Phase Decompositions In Iron-nickel Systems At Low Temperatures.

Order Number 9519848

Phase decompositions in Fe-Ni systems at low temperatures

Yang, Cheol-Woong, Ph.D.

Lehigh University, 1995

U·M·I

300 N. Zeeb Rd.
Ann Arbor, MI 48106

Phase Decompositions in Fe-Ni Systems at Low Temperatures

by

Cheol-Woong Yang

Presented to the Graduate and Research Committee

of Lehigh University

in Candidacy for the Degree of

Doctor of Philosophy

in

Materials Science & Engineering

Lehigh University

December, 1994

CERTIFICATE OF APPROVAL

Approved and recommended for acceptance as a dissertation in partial fulfillment of the requirements for the degree of Doctor of Philosophy.

12/8/94
Date

Joseph I. Goldstein
Dissertation Director
Dr. Joseph I. Goldstein

12/8/94
Accepted Date

Special committee directing the doctoral work of Mr. Cheol-Woong Yang:

Joseph I. Goldstein
Dr. Joseph I. Goldstein

Dr. David B. Williams

Dr. Arnold R. Marder

Edward RD Scott
Dr. Edward R. D. Scott

ACKNOWLEDGEMENTS

I would like to express my sincere appreciation to my advisors, Dr. J. I. Goldstein and Dr. D. B. Williams for their continuous guidance and support throughout the course of my Ph. D. study. I also appreciate the interest and suggestions of the other members of my committee: Dr. A. R. Marder and Dr. E. R. D. Scott. Appreciation is extended to Dr. R. B. Scorzelli, Dr. R. S. Clarke, Jr. and the Smithsonian Institution for providing meteorite samples.

Special thanks are due to Dave Ackland, Jim Kerner and Kathy Repa for technical assistance and for their efforts to keep the electron microscopes running smoothly, especially for accepting late night and weekend panic calls, to Arlan Benscoter for helpful discussion about etching techniques and to Andrea Pressler for her help in making slides and prints. I am also grateful to the staff of Department of Materials Science and Engineering, especially Pat Newhart, Maxine Mattie for their help in those all-confusing paper works.

My sincere thanks go to Dr. Jondo Yun, Dr. Minseok Oh and Dr. Changmo Sung for valuable discussions and for their support and encouragement. I would like to acknowledge my fellow graduate students in the department, especially, Jihwan Kim, Junghyun Cho, Young Jin Choi, Ming-wei Tseng, Lina Ma, Sambit Saha, Michael Huang, Michael Zemyan, Saikumar Vivekanand, and Jicheng Zhao for their time and efforts for valuable discussions and technical assistance. I would also like to say "Thanks" to all the members of the Korean community at Lehigh, especially, Dr. Sungul Hong, Gyutae Baek, Bemmjae Choi, Sang Koo Lee, Dong Ho Lee, Soongwon Yoo, Soojun Park,.....

I would like to thank my family at home, who has been a continuous source of support: Grandmother, father, mother, Sunyoung and Kyoungmo. I would like to especially thank my parents, Seong-Pil Yang and Hee-Bok Ryu, for their support,

understanding and encouragement throughout the course of my education. I would also like to thank my parents in law for their support and encouragement.

Finally, I would like thank my wife, Eunha Kim, for her enthusiasm, limitless paitence and constant encouragement, and my little daughter, Haeyeon, for having been an easygoing, happy baby.

TABLE OF CONTENTS

LIST OF TABLES

LIST OF FIGURES

rim are observed. The arrows give the general boundaries of zone 1/zone 2 and zone 2/zone 3. The arrow on the right shows the position of the taenite/silicate (S) boundary.

Fig. 4.3 a) a light optical micrograph of retained taenite surrounded by silicate matrix in Patwar mesosiderite. b) a SEM image of the outer taenite rim which shows three sub-zones (1, 2, 3). T: retained taenite, TR: tetrataenite, CZ: cloudy zone, S: silicate matrix.

Fig. 4.4 The SEM images of the outer taenite rim of the RKPA79015 mesosiderite. a) an image of the cloudy zone (CZ), the outer taenite rim (TR) containing three sub-zones(1, 2, and 3), and kamacite (K). b), c) and d) are high magnification images of three sub-zones; zone 1, zone 2 and zone 3, respectively.

Fig. 4.5 Ni concentration profile obtained with EPMA traversing kamacite, TR and CZ in the RKPA 79015 mesosiderite showing well known "M" shaped profile. Note the discontinuity in the Ni content at the TR/CZ boundary.

Fig. 4.6 A SEM image of the tetrataenite rim in the Imilac pallasite.

Fig. 4.7 A SEM image of the tetrataenite rim in the Carbo (IID) iron meteorite.

Fig. 4.8 A series of TEM images of the tetrataenite rim of taenite in the RKPA 79015 mesosiderite. a) BF image, b) CDF image using the (010) superlattice reflection, c) SADP showing a $[100]_{fcc}$ zone axis pattern with three variants of the $L1_0$ ordered superlattice reflections, and d) indexing of the SADP.

Fig. 4.9 A set of images from the tetrataenite rim and the cloudy zone of the RKPA 79015 mesosiderite at the boundary between the two structures. a) SEM image showing the etch pits b) TEM bright field image showing precipitates which correspond to the etch pits in a).

Fig. 4.10 A set of TEM bright field images of the RKPA79015 mesosiderite. a) BF image of the tetrataenite rim and the cloudy zone at the boundary between the two structures. b) BF image showing the precipitate loop and some scattered precipitates at the center of the tetrataenite rim (zone 2). c) CBED pattern from a precipitate in the TR containing a fcc $[100]_\gamma$ matrix pattern with a bcc $[011]_\alpha$ precipitate pattern. d) indexing of the CBED pattern.

Fig. 4.11 A series of TEM images taken at the border between the TR and the CZ. a) BF image, b) CDF image using a $(200)_\alpha$ reflection of bcc $[011]_\alpha$ zone axis pattern, c) CDF image using a (100) superlattice reflection, d) SADP, e) schematic diagram of the SADP, f) indexing of the $[100]_\gamma$ fcc matrix pattern and superlattice reflections, and the $[100]_\alpha$ bcc zone axis pattern, and g) indexing of the $[011]_\alpha$ bcc zone axis pattern.

Fig. 4.12 a) Convergent beam micro-diffraction pattern of the tetrataenite matrix in the outer taenite rim, b) Indexing of the diffraction pattern containing $[100]_\gamma$ fcc matrix spots with superlattice reflections and $[\bar{1}\,11]$ oxide spots.

Fig. 4.13 A set of TEM images of the tetrataenite rim and the cloudy zone of the Saint Séverin ordinary chondrite.

Fig. 4.14 a) a TEM BF image of the RKPA79015 mesosiderite at the boundary between the cloudy zone (CZ) and the tetrataenite rim (TR), b) Ni composition profile across kamacite and taenite.

Fig. 4.15 A Ni composition profile across the kamacite/tetrataenite rim interface in the RKPA 79015 mesosiderite obtained with VG HB501 STEM.

Fig. 4.16 TEM bright field images of the precipitates in the tetrataenite rim region of the mesosiderites: a) Estherville and b) RKPA 79015.

Fig. 4.17 A Ni composition profile across a precipitate in the RKPA 79015 mesosiderite obtained with VG HB501 STEM.

Fig. 4.18 SEM images of the cloudy zone of the RKPA79015 mesosiderite. a) substructure is marked with a arrow, b) high magnification image showing details of the substructure. H: honeycomb phase, I: island phase

Fig. 4.19 A series of SEM images of a taenite particle in Saint Séverin (LL6) chondrite showing the size variation of the island phase in the cloudy zone. b), c) and d) are high magnification images of regions A, B, and C labeled in a), respectively.

Fig. 4.20 a) a SEM image of the Estherville mesosiderite showing the microstructure of a retained taenite. b) a Ni concentration profile obtained by EPMA traversing kamacite and retained taenite.

Fig. 4.21 A set of images of the cloudy zone in the RKPA 79015 mesosiderite. a) SEM image showing the etch pits (marked with arrows) as well as honeycomb phase (H) and island phase (I), b) TEM bright field image showing precipitates which correspond to the etch pits in a).

Fig. 4.22 A set of TEM bright field and dark field images of the cloudy zone of the Estherville mesosiderite. a) BF image containing the island phase (I) which is bright, the honeycomb phase (H) which is dark, and the precipitates (P) within the island phase, b) CDF image from a (011) bcc reflection, c) SADP, and d) indexing of the SADP.

Fig. 4.23 a) TEM bright field image of the CZ region of Saint Séverin chondrite, b) centered dark field image from a (011) bcc spot, c) SAD pattern, d) indexing of the SAD pattern; ●hkl: bcc[111] zone axis pattern; * hkl: another bcc [111] zone axis pattern; ○ hkl: fcc[110] zone axis pattern; ⋆ superlattice diffraction spots (observed on the negative).

Fig. 4.24 a) a TEM BF image of the cloudy zone in the Saint Séverin chondrite. The island phase is labeled I, b) CBED pattern from the island phase showing a fcc [110] zone

ABSTRACT

In order to understand the low temperature phase transformation mechanismes in the Fe-Ni system, the microstructure and microchemistry of meteorites were investigated using various AEM techniques. The sub-zone structure within the tetrataenite rim was observed in iron, stony-iron and stony meteorites. This sub-zone structure is due to the fact that the tetrataenite rim is composed of low Ni bcc precipitates (14.2 ± 1.0 wt.% Ni) in a high Ni $L1_0$ ordered FeNi matrix (51.8 ± 1.7 wt.% Ni). The density of the precipitates changes with the position. The outermost layer of the TR is likely to be the $L1_2$ (Ni_3Fe) ordered structure (65.5 ± 3.3 wt.% Ni). The Ni content of kamacite at the TR interface was 3.6 ± 0.2 wt.% Ni. The cloudy zone is composed of low Ni bcc honeycomb phases (9.0 ± 1.0 wt.% Ni) and high Ni island phases (51.8 ± 1.7 wt.% Ni) with low Ni precipitates inside. The matrix of the island phases is ordered FeNi with the $L1_0$ superstructure.

The low temperature Fe-Ni phase diagram was modified using the AEM data obtained from meteorites in this study. A monotectoid reaction ($\gamma_1 \rightarrow \alpha + \gamma_2$) at about 400°C and a eutectoid reaction ($\gamma_2 \rightarrow \alpha + \gamma'$) at 345°C were incorporated in the new phase diagram. At low temperatures, α and γ' (Ni_3Fe) phases are in equilibrium , while γ'' (FeNi) phase is present as a metastable phase.

A new method to determine the low temperature cooling rate of the meteorite has been established. The size of the biggest island phase decreases with increasing cooling rate without regard to whether the host is an iron, stony-iron or stony meteorite. The size of the biggest island phase of the meteorites that were investigated in this study varies approximately from 470 nm to 17 nm, while the cooling rate varies from 0.5 K/Myr to 325 K/Myr. The cooling rates vary in the IIIAB-Pallasite group meteorites. The cooling rates vary randomly with Ni concentration for the IVA group iron meteorites.

1. INTRODUCTION

The Fe-Ni alloy system has been an attractive research topic for several decades. Not only is the Fe-Ni alloy system a class of important structural materials, but more importantly, it has some unique characteristics. Especially, a very unique and complicated microstructure of Fe-Ni alloy has developed in meteorites during the extremely slow cooling process that these meteorites experienced. The microstructure of meteorites that formed at a slow cooling rate cannot be completely duplicated in the laboratory due to the sluggish diffusion of Ni at low temperatures. For example, at 300°C, it takes more than 10^4 years for one atomic jump to occur. Therefore, little experimental data exist for the Fe-Ni system at lower temperatures. To overcome this problem, the microstructure and chemistry of the metallic phases in meteorites were investigated. Because meteorites have cooled slowly, low temperature phase transformations can occur. Therefore, the microstructure and microchemistry of the metallic phases in meteorites can be used to determine the phase boundaries in the low temperature Fe-Ni phase diagram, and to understand the phase transformations occurring at low temperatures.

Because the phases that form in meteorites at low temperatures are on a submicron scale, analytical electron microscopy (AEM) techniques were employed in this study. High spatial resolution X-ray microanalysis using energy dispersive spectrometry (EDS) was used to determine the chemistry, and electron diffraction was used to identify the crystal structures of the various phases in the meteorites. With the results from the AEM analysis in this study, the low temperature Fe-Ni phase diagram was modified.

In order to understand the phase transformation processes correctly, the thermal history (cooling rate) of the system should be considered. In this study a new method to determine the cooling rate of meteorites was proposed.

From the metallurgical point of view, a study of the microstructure of meteorites will give a better understanding of the phase transformation processes that occur in

transition metal systems at low temperatures. Furthermore, an understanding of the meteorite microstructure will provide valuable information on the thermal history of our solar system in which the meteorites evolved.

The main objective of this study is to gain an understanding of the phase transformation processes that occur in the Fe-Ni systems at low temperatures. The Fe-Ni phase diagram below 400°C was determined, and a new method for determination of cooling rate of meteorites was developed.

2. BACKGROUND

2.1 Diffusional Decompositions in Solid Solutions

Solid state transformations occur either heterogeneously, whereby fluctuations in composition are large in degree but small in extent, or homogeneously, where compositional fluctuations are small in degree but large in extent [Soffa and Laughlin, 1982]. Heterogeneous transformations including both the classical homogeneous and heterogeneous nucleation processes generally involve the spatial partitioning of the system into transformed and untransformed regions, separated by interphase interfaces [Christian, 1975]. On the other hand, homogeneous, or continuous transformations occur uniformly throughout the entire system via the continuous amplification of initially small fluctuations in composition within the supersaturated or undercooled solid solution resulting in a more stable state [Christian, 1975; Laughlin *et al.*, 1984]. Thus, the alloy cannot be separated into transformed regions and untransformed regions. Continuous transformations include spinodal decomposition and spinodal ordering. It is worth emphasizing that phase separation and ordering are not mutually exclusive phenomena but can occur together in the same system often in a cooperative or interdependent manner [Laughlin *et al.*, 1984; Soffa and Laughlin, 1982, 1989; Kubo and Wayman, 1980; Allen and Cahn, 1976]. It has been shown, for example, that in both Cu-Ti and Fe-Be alloys, a supersaturated alloy first lowers its free energy by a homogeneous ordering process followed by concomitant spinodal decomposition and long range atomic ordering within the solute enriched phase [Laughlin *et al.*, 1984]. Since one objective of this study is to gain a better understanding of the decomposition which has occurred in the Fe-Ni system at low temperatures, the possible phase transformation mechanisms are reviewed herein.

2.1.1 Nucleation and Growth

When a single phase (α) solid solution becomes supersaturated (α') and falls into two phase ($\alpha+\beta$) field as temperature changes, the most common mechanism through which the metastable α' phase is transformed into a stable $\alpha+\beta$ two phase mixture is nucleation and growth. In the nucleation stage, nuclei of the precipitating phase are formed. These result from spatially localized composition fluctuations which occur statistically within the supersaturated matrix. In the latter stage, the so-called growth regime, diffusional growth of a precipitate occurs by solute depletion of the surrounding matrix without competing with the growth of any other particles. Finally, in the coarsening regime, the particle dispersion established during the nucleation and growth period coarsens by the growth of larger particles at the expense of the smaller ones.

The free energy change associated with the nucleation process will have the following contributions. The volume free energy (ΔG_v) will decrease by the formation of a volume V of the precipitate phase β. However, the strain energy (ΔG_s) and interfacial energy (γ) introduced by forming the β phase of which an interfacial area is A will increase the free energy of the system. Nucleation in solids is almost always heterogeneous [Porter and Easterling, 1981]. Suitable nucleation sites are non-equilibrium defects such as excess vacancies, dislocations, grain boundaries, stacking faults, inclusions, and free surfaces, all of which increase the free energy of the material. If the creation of a nucleus results in the destruction of a defect, some free energy (ΔG_d) will be released thereby reducing (or even removing) the activation energy barrier. The total free energy change can be written as:

$$\Delta G = -V(\Delta G_v - \Delta G_s) + A\gamma - \Delta G_d \qquad (2\text{-}1)$$

The equation shows that, thermodynamically, the optimum shape of the new phase generally will represent a compromise between the surface and strain energies. There is a critical size (r^*) of the precipitate at which the free energy reaches a maximum

as shown in Fig. 2.1. Any embryo which is larger than the critical size ($r>r^*$) is able to grow larger lowering the free energy of the system. The maximum increase of the free energy due to the initial formation of the embryo (ΔG^*) is the energy barrier for nucleation. The driving force for nucleation is provided by supersaturation or undercooling as shown in Fig. 2.2. The driving force increases with increasing undercooling (ΔT) below the equilibrium solvus temperature, T_e. The nucleation does not occur until a critical undercooling (ΔT_c) is reached because the driving force (ΔG_n) is too small, whereas at very high undercooling, nucleation rate is negligible because diffusion is too slow. A maximum nucleation rate is obtained at intermediate undercoolings.

2.1.2 Spinodal Decomposition

In a continuous or spinodal transformation, the phase separation occurs spontaneously with continuous decrease in free energy and there is no energy barrier for decomposition. Free energy (G) vs. composition (X) curves can be used, in conjunction with the phase diagram, to illustrate the phenomenon of spinodal decomposition. When a single phase solid solution (α) of composition X_0 is cooled into a miscibility gap at T_2, as shown in Fig. 2.3, its initial free energy will be represented as G_0 and the free energy curve of the α phase has a negative curvature:

$$\frac{d^2G}{dX^2} = G'' < 0$$

The α phase will immediately become unstable because any small fluctuation in composition will reduce the free energy of the system, and therefore, α will decompose into two stable phases ($\alpha_1+\alpha_2$) which contain equilibrium compositions, X_1 and X_2. The spinodal line in Fig. 2.3 indicates an instability with respect to the response of the system to compositional fluctuations. The locus, called the "chemical spinodal", is defined by the inflection points of the isothermal free energy vs. composition curves ($G''= 0$). Spinodal

decomposition essentially involves the amplification of long wavelength concentration waves within the supersaturated state resulting from "up-hill" diffusion as a consequence of the inherent thermodynamic instability of the system. The transformation occurs homogeneously throughout the alloy via the gradual buildup of regions alternately enriched or depleted in solute. Fig. 2.4 a) and 2.4 b) are schematic composition profiles of the two phase structure in various stages of the transformation showing the difference between a) the spinodal mechanism and b) the nucleation and growth mechanism. If the alloy lies outside the spinodal, X_0' in Fig. 2.3, small variations in composition lead to an increase in free energy and the alloy is therefore metastable. The free energy of the system can only be decreased through nucleation and growth by overcoming the energy barrier.

Spinodal decomposition was discussed in detail by Cahn [1961, 1962, 1968]. The factors controlling the spinodal reaction and resultant structures are clarified by examining the energetics of small-amplitude composition fluctuations in solid solutions. After considering the strain energy and the interfacial energy introduced by the decomposition, Cahn has shown that the free energy change due to the formation of a composition fluctuation is:

$$\Delta G = \left[\frac{d^2 G}{dX^2} + \frac{2K}{\lambda^2} + 2\eta^2 E' V_m \right] \cdot \frac{(\Delta X)^2}{2} \qquad (2\text{-}2)$$

where ΔX and λ is the amplitude and the wave-length of the composition fluctuation. The second term of Equation (2-2) represents the contribution of the interfacial energy and K is a proportionality constant.

$$\eta = \frac{1}{a}\left(\frac{da}{dX}\right); \qquad E' = \frac{E}{1-\nu}$$

where a is the lattice parameter, E is the Young's modulus and v is the Poisson's ratio. The third term of Equation (2-2) represents the coherency strain energy effects. The coherency strain energy term is independent of wavelength, but can vary markedly with crystallographic direction in elastically anisotropic crystals. Therefore, the dominant concentration waves will develop along elastically soft directions in anisotropic systems.

The significance of Equation (2-2) is that it gives the criterion for spinodal decomposition to occur in a solid solution, i.e.

$$\left|-\frac{d^2G}{dX^2}\right| > \frac{2K}{\lambda^2} + 2\eta^2 E' V_m \qquad (2\text{-}3)$$

Thus the limits of temperature and composition within which spinodal decomposition is possible are given by the conditions $\lambda = \infty$ and

$$\frac{d^2G}{dX^2} = G'' = -2\eta^2 E' V_m \qquad (2\text{-}4)$$

This condition defines the coherent spinodal in the phase diagram. Two different spinodal transformation lines can be drawn on the phase diagram: the chemical spinodal (G''=0) and the coherent spinodal. Fig. 2.5 schematically illustrates the position of typical chemical and coherent spinodal boundaries with respect to the incoherent and coherent miscibility gaps. The incoherent miscibility gap corresponds to the equilibrium composition of the phases in the absence of strain fields. The chemical spinodal is associated with this incoherent miscibility gap as it also ignores any strain energy effects and only considers the change in free energy due to the change in composition between the enriched and depleted regions. The coherent miscibility gap, on the other hand, takes into account the coherency strain effects. As shown in Fig. 2.5, the coherent spinodal lies entirely within the chemical spinodal. Since the strain energy term is strongly dependent

on lattice parameter change, the chemical and coherent spinodal will be very close if there is a small change of the lattice parameter with composition [Chamberod *et al.*, 1979].

The minimum possible wavelength that can be formed by spinodal decomposition may be calculated from Equation (2-3), i.e.

$$\lambda_{min}^2 > \frac{2K}{-\left(\frac{d^2G}{dX^2} + 2\eta^2 E' V_m\right)} \qquad (2\text{-}5)$$

If the term in the parentheses is greater than zero, Equation (2-4) is not valid. This means that the strain energy is too large for spinodal decomposition to occur. The wavelength of the compositional fluctuation, λ, depends on the amount of undercooling below the coherent spinodal. Cahn [1968] showed that λ is proportional to $(T_s - T)^{-1/2}$ in which T_s is the coherent spinodal temperature and T is the reaction temperature. Thus, the larger the undercooling, the smaller the wavelength. Long wavelength fluctuations grow sluggishly because of the large diffusion distance; short wavelength fluctuations are suppressed by the interfacial energy effects. The microstructure that develops during spinodal decomposition in metallic systems has a characteristic periodicity that is typically 2.5 to 10 nm [Laughlin and Soffa, 1988].

The rate of the spinodal transformation is controlled by λ and the interdiffusion coefficient, $\tilde{D}$, which is negative within the spinodal. The compositional fluctuations will increase exponentially with time with the relaxation time $\tau \approx -\lambda^2/\tilde{D}$. Thus, with a large $\tilde{D}$ and a small λ, the decomposition rate can be high.

2.1.3 Order/Disorder Transformation

Solid solutions which have a negative enthalpy of mixing ($\Delta H_{mix}<0$) prefer unlike nearest neighbors and therefore show a tendency to form ordered phases at low temperatures.

"Long-range order" describes the macroscopic state of order of the system. In a binary system consisting of A and B atoms, the ordered structure is composed of two distinct sublattices commonly denoted as α and β sublattices. In case of perfect order, all the α sites are occupied by A atoms and all the β sites are occupied by B atoms. When the system becomes completely disordered, the occupation of sub lattice sites becomes random. A critical transformation temperature (the Kurnakov point), T_k, is associated with this transformation, below which the system is ordered to some degree, and above which the system is disordered [Reynaud, 1982].

Another phenomenon of the order-disorder transformation is "short-range order". Contrary to long-range order, short-range order describes the local state of order in the system. Short-range order can exist above the critical temperature when long-range order vanishes.

A long-range order parameter, L, is defined as:

$$L = \frac{r_A - X_A}{1 - X_A} \qquad (2\text{-}6)$$

where X_A is the mole fraction of A atoms in the alloy and r_A is the probability of finding an A atom on an α lattice site. L equals 0 for a completely disordered arrangement and L equals 1 for a fully ordered alloy. The degree of order in an alloy depends strongly on temperature. At absolute zero the crystal will minimize its free energy by choosing the most highly ordered arrangement (L=1) which corresponds to the lowest internal energy. As the temperature increases, L will decrease and some disorder will exist. Above some critical temperature (T_k), the alloy will be completely disordered (L=0). The way in

which L decreases to zero is different for the different superlattices. By choosing a suitable model, it is possible to predict how L varies with temperature.

There are two possible mechanisms for creating an ordered structure from a disordered system. First, there may be a continuous increase in short-range order by local rearrangements occurring throughout the sample resulting in long-range order. This mechanism is called continuous ordering. Second, there may be an energy barrier to overcome in order to form ordered domains. This mechanism is termed heterogeneous ordering. Although both types of mechanisms have been observed experimentally, heterogeneous ordering is more common. According to the Ehrenfest classification, a heterogeneous process is associated with a first order transformation while a continuous process is associated with a second order transformation. The Ehrenfest classification of phase transformations is based on the successive differentiation of a thermodynamic potential (e.g. Gibbs free energy) with respect to an external variable such as temperature or pressure. The order of the transformation is given by the lowest derivative to exhibit a discontinuity. In a first order transformation, the partial derivative of the Gibbs free energy with respect to temperature is discontinuous at the transition temperature. There is thus a latent heat of transformation evolved at a sharp transformation interface which separates the co-existing parent and product phases. A two phase region exists on the phase diagram. In a first order transformation, L changes substantially at the critical temperature and the phase change occurs at a well defined interface separating the parent and product phases. In these circumstances, interface structure must dominate the mechanism of the transformation and the formation of a new phase involves a nucleation and growth process. On the other hand, in a second order transformation, L changes continuously from disorder to order. Thus, disorder and order do not co-exist at any temperature, even for alloys off the stoichiometric composition; when such a transformation involves a lattice change, the change occurs continuously throughout the

parent phase until its lattice is gradually changed into that of the product. There is no identifiable interface.

The systematics of possible reaction paths involving clustering and ordering in the alloy system can be elucidated using a simple approach based on graphical thermodynamics or free energy-composition (G-C) curves. A series of hypothetical free energy-composition diagrams are shown in Fig. 2.6. The free energy curve associated with the disordered solid solution is considered concave upwards at all compositions in Fig. 2.6 a). The ordered free energy curve represents the free energy of a homogeneous ordered phase of optimum order parameter. Clearly, the free energy curve for the ordered solution is a projection of a locus along the G-C-η surface, η being the order parameter [Laughlin *et al.*, 1984]. For this free energy-composition scheme, spinodal decomposition can only occur if the supersaturated solid solution orders first. A disordered solid solution of composition C_0 is metastable with respect to precipitation of the A_xB_y phase; however, the solid solution can lower its free energy from P to Q by ordering. This partially ordered state is unstable with respect to phase separation and the system can undergo a spinodal reaction involving continuous clustering and ordering leading to a metastable two-phase mixture. Here the spinodal reaction is entirely contingent on prior ordering and is termed a 'conditional spinodal' [Allen and Cahn, 1976]. On the other hand, the composition C_0' which is also metastable with respect to precipitation of the ordered phase, can lower its free energy from P' to Q' by ordering. This ordered state is still metastable with respect to the formation of the A_xB_y phase.

The clustering and ordering process may also be interpreted in terms of the slightly modified schemes shown in Fig. 2.6 b). Here the disordered free energy curve also shows inflections and phase separation. In Fig. 2.6 b) the disordered solid solution of composition γ_0 is unstable with respect to phase separation and spontaneous unmixing will occur leading to solute-enriched and solute-depleted regions. When the composition

in the solute-enriched region exceeds the composition o, this region will order. A continuous phase separation involving clustering and ordering can then proceed, eventually generating the two-phase mixture denoted by the common tangent construction. In this case, clustering precedes the ordering reaction and then the system progresses toward equilibrium via cooperative clustering and ordering. The composition γ_0' is unstable with respect to clustering and ordering. it is likely that short range atomic exchanges occur rapidly to produce ordering, relaxing the free energy along the G-C-η surface toward the ordered curve. Simultaneously a spinodal reaction leading to continuous unmixing or phase separation can occur. This is in contrast to previous case (γ_0) in which the supersaturated state is unstable initially only with respect to long wavelength compositional fluctuation.

Importantly, in the case of the thermodynamically first-order order/disorder transformation, a spinodal decomposition process resulting in a two-phase mixture of ordered and disordered phases at equilibrium always involves prior ordering of the solution, either by congruent (heterogeneous) or continuous (homogeneous) ordering [Soffa and Laughlin, 1989].

2.2 Fe-Ni Phase Diagram

There have been many versions of the low temperature Fe-Ni phase diagram proposed by different research groups based on their experimental or theoretical work, although it cannot yet be considered as complete. At the Fe-rich side of the phase diagram the $\alpha/\alpha+\gamma$ and the $\alpha+\gamma/\gamma$ phase boundaries were established experimentally by Romig and Goldstein [1980] down to 300°C. On the Ni-rich side of the phase diagram, the Ni_3Fe ordered fcc phase which has $L1_2$ superstructure was first detected by Leech and Sykes [1939] using X-ray diffraction. Van Deen and Van der Woude [1980, 1981] determined the phase diagram around the critical ordering temperature of Ni_3Fe using Mössbauer

spectroscopy. They found a first order transformation with a maximum critical ordering temperature of 516°C at 73 at.% Ni.

A eutectoid reaction was incorporated by Heumann and Karsten [1963] suggesting that the α and Ni_3Fe were in equilibrium at low temperatures. They determined the $\alpha+Ni_3Fe/Ni_3Fe$ boundary and the eutectoid point which was at 345°C and 52 at.% Ni. It is worth noting that they used a chemical metallurgy method to prepare the sample and the final samples contained up to 0.2 wt.% C. Combining the above data, Kubaschewski [1982] constructed a complete Fe-Ni phase diagram shown in Fig. 2.7. The FeNi and Fe_3Ni phases were also incorporated in this phase diagram under the eutectoid temperature in the two phase field. These two phases were drawn in dashed lines and accompanied by a question mark indicating that no solid experimental evidence was available.

The existence of the ordered FeNi phase has been established in meteorites and the critical ordering temperature was determined by high energy particle irradiation experiments. Rossiter and Jago [1984] proposed a phase diagram including the ordered FeNi phase as shown in Fig. 2.8. The critical ordering temperatures that they accepted were 320 °C at 50 at.% Ni and 350 °C at 52 at.% Ni [Sadchikov and Puzey, 1983]. Therefore two eutectoid points were introduced with α+FeNi and FeNi+Ni_3Fe in equilibrium respectively.

There were attempts to calculate the Fe-Ni phase diagram thermodynamically. The thermodynamic calculations are very useful but they usually need something to start with such as the existing phases and their structures. Recently major progress has been made by Chuang *et al.* [1986a, 1986b] in showing the interplay of the chemical and magnetic contributions to the stability of phase equilibria of Fe-Ni alloys. They calculated the Fe-Ni phase diagram by taking into account the magnetic effect in the Gibbs free energy. The magnetic contribution is large enough to change the free energy curve in a

system which shows rapidly changing Curie temperature vs. composition. Based on thermodynamic calculation, Chuang *et al.* introduced a tricritical point at 462°C and 48.8 wt.% Ni. In addition, a miscibility gap of the fcc phase, as well as the associated spinodal, at low temperatures was predicted for Fe-Ni alloy system resulting in the formation of a monotectoid equilibrium at 389°C as given below:

$$\gamma_1 \text{ (41.2 wt.\% Ni)} \Leftrightarrow \alpha \text{ (6.6 wt.\%Ni)} + \gamma_2\text{(47.5wt.\%Ni)}$$

Their calculated phase diagram is shown in Fig. 2.9. Since they used Kubaschewski's phase diagram to establish the thermodynamic functions which they need for the calculation, this diagram is basically the same as that of Kubaschewski except for the miscibility gap and the resulting $\alpha+\gamma_2$ two phase field, the monotectoid reaction, and the tricritical point.

Since the experimental evidence from both iron meteorites and Invar alloys indicated some kind of phase decomposition, the magnetically induced miscibility gap has been accepted by Reuter *et al.* [1988] in constructing a new phase diagram. As shown in Fig. 2.10, the FeNi phase joins the γ phase congruently at 462°C and 47 at.% Ni, and the critical ordering temperature of the FeNi ordered phase is 320°C. The boundaries of the miscibility gap and the spinodal decomposition area are determined from the analytical data of the iron meteorites and HVEM in-situ irradiation experiments. The authors extended the FeNi phase to the disordered γ phase field because no α/Ni_3Fe equilibrium has been observed in iron meteorites. The Fe_3Ni phase is left out since experimental evidence, especially the atom probe work by Miller and Russell, shows that the Fe_3Ni phase does not exist in the iron meteorites. The diagram of Reuter *et al.* [1988] actually combines the features of the Rossiter's diagram (Fig. 2.8) and Chuang's diagram (Fig. 2.9).

Another miscibility gap has been proposed by Rusell and Garner [1992] to account for the experimental evidence for a high temperature phase decomposition. A high temperature miscibility gap and spinodal were proposed as shown in Fig. 2.11. They argued that the large scale composition fluctuation which occurred in the neutron irradiated alloys could not be formed by the low temperature decomposition. Their high temperature miscibility gap suggests that the 35 wt.% Ni alloy decomposes into 25 wt.% and 50 wt.% Ni phases at 550°C. They did not exclude the low temperature miscibility gap in order to explain the other experimental evidence which showed much finer scale decomposition products.

2.3 Meteorites

2.3.1 Classification of Meteorites

Meteorites can be classified into three major groups based on their metallic iron and nickel, and silicate content: iron, stony and stony-iron meteorites. Iron meteorites consist almost entirely of Fe-Ni alloys, whereas stony meteorites are composed mostly of silicate minerals although many also contain small metal grains. In a third category are stony-iron meteorites, which have nearly equal proportions of metals and silicates [Dodd, 1981; Wasson, 1985; McSween, 1987].

2.3.1.1 Iron Meteorites

There are two entirely different classification schemes for iron meteorites now in use. One of these is the structural classification based on the structures present in irons. The other scheme requires accurate chemical analysis. By the structural classification scheme, iron meteorites can be classified into three major classes, hexahedrites (H), octahedrites (O) and ataxites (D) as shown in Table 2.1. Most iron meteorites have a characteristic texture, the Widmanstätten pattern, which consists of α-ferrite (bcc)

precipitates that have nucleated and grown preferentially on the octahedral planes of the parent γ-austenite (fcc) phase (See section 2.3.2.1). In the meteoritic terminology, the bcc α-ferrite is called kamacite and the fcc γ-austenite is called taenite. However, iron meteorites with less than about 6 wt.% Ni contain only kamacite but no taenite. Because kamacite is cubic, such meteorites are called hexahedrites, from the Greek word for "cube". The hexahedrites have a microstructure containing large equiaxed single crystals of kamacite. The octahedrites of which Ni content vary from ~6 wt.% to ~18 wt.% have well developed Widmanstätten structure. The octahedrites constitute by far the largest and most diverse group of iron meteorites, so they are subdivided by use of the width of the kamacite bands that form the Widmanstätten pattern into five groups: coarsest (Ogg), coarse (Og), medium (Om), fine (Of), and finest (Off). Generally, the higher the Ni content, the finer is the kamacite band width. The ataxites have a microscopic Widmanstätten structure which is not visible with the unaided eyes. Such meteorites consist almost entirely of taenite, with only a few microscopic plates of kamacite. The Ni content of the ataxites is usually higher than 15 wt.%.

The chemical group classification scheme utilizes trace elements to diagnose the different groups. An initially proposed subdivision into four groups, named I through IV, was based on varying contents of Ga, Ge and Ir as well as the abundance of Ni. When enough high quality chemical data became available, some of these groups were subdivided further like IVA and IVB. Comparison of chemical and structural classifications for iron meteorites is shown in Table 2.1.

2.3.1.2 Stony Meteorites

Stony meteorites can be divided into two broad categories: chondrites and achondrites. The chondrites are a kind of cosmic sediment which has suffered little chemical change since formation. In contrast, the achondrites are an igneous rock, that is, a

product of partial melting. The chondrites can be further divided into three major classes (enstatite, ordinary and carbonaceous) with eight subgroups and six petrologic types according to their chemistry and metamorphic grade, respectively [Dodd, 1981; Wasson, 1985]. Table 2.2 shows the classification of chondrites. The enstatite chondrites (named for their high abundance of the mineral enstatite, $MgSiO_3$) are all strongly reduced and their silicates generally contain very little Fe. The carbonaceous chondrites, however, are all strongly oxidized and therefore contain very little metal. The ordinary chondrites (so named because they are the most abundant type), are neither strongly oxidized nor strongly reduced and thus contain significant amounts of both metallic and oxidized Fe. The category of principal interest in this study is the ordinary chondrites. The ordinary chondrites are subdivided on the basis of distinctive iron contents into high-iron (H), low-iron (L), and lower-iron (LL) groups. Six grades of metamorphism in chondrites based on observable textural and mineralogical changes have been recognized. These metamorphic grades (called petrologic types) are combined with the chemical classes already discussed to formulate the currently used classification for chondrites.

2.3.1.3 Stony-Iron Meteorites

The stony-iron meteorites include two chemically, texturally distinct kinds of materials (pallasites and mesosiderites). They consist of roughly equal proportions of metal and silicates. Pallasites consist of crystals or crystal fragments of magnesian olivine [$(Fe,Mg)_2SiO_4$] in continuous matrix of metallic Fe-Ni alloy. The metallic phases in pallasites have Ni, Ge, and Ga contents that are rather similar to those in group IIIAB iron meteorites [Dodd, 1981; McSween, 1987]. Mesosiderites appear to be more or less recrystallized mechanical mixtures of silicates and metal, are related to several groups of a achondritic stony meteorites [Dodd, 1981]. The metallic phases in mesosiderites usually

occur as discrete blebs and grains that may reach centimeter-size and display Widmanstätten structure [Buchwald, 1975].

2.3.2 Microstructure of Meteorites

2.3.2.1 Widmanstätten Structure

Grains of kamacite nucleate and grow in certain preferred orientations within the fcc taenite lattice. Kamacite forms four sets of plates that cut the corners of the original cubic crystals, forming eight-sided octahedra. The intergrown plates of kamacite within taenite can be readily seen in iron meteorites. In 1808, Count Alois de Widmanstätten first observed this structure, now called the Widmanstätten pattern. The degree of development and coarseness of this pattern depends on bulk Ni content and thermal history, and have been used, with trace element data, to place the iron meteorites in three major classes and many smaller groups. Fig. 2.12 a) is a typical Widmanstätten structure as seen in the Dayton iron meteorite and shows the regular arrangement of ferrite plates.

The formation of the Widmanstätten pattern can be understood based on the established high temperature portion of the Fe-Ni phase diagram. In the composition range of the octahedrites, the meteorites were single phase taenite above a temperature of ~750°C. As they cooled down through the two phase region, kamacite precipitated and grew simultaneously on the crystallographically equivalent planes of the taenite ({111} planes of the fcc). The extent of kamacite growth depends on the bulk Ni composition along with the cooling rate of the parent body.

The Widmanstätten structure can also be observed in mesosiderites. In chondrites, however, no Widmanstätten structure has been observed. Metallic particles in chondrites are basically composed of kamacite and taenite [Urey and Mayeda, 1959], and are commonly in contact with troilite (FeS) and silicates[Willis and Goldstein, 1983]. Fig. 2.13a is a low magnification light optical photograph of the St. Séverin ordinary chondrite.

As shown in Fig. 2.13a, kamacite and taenite grains, which often appear to be isolated particles, are connected directly or by intervening troilite(FeS) in three dimension [Willis and Goldstein, 1983]. Ni is entering the taenite grain from the taenite/silicate interface so that zoning (See next section) can occur around each metal particle. It is likely that surface diffusion or grain boundary diffusion is sufficiently fast to transport Ni around the perimeter of the taenite grain [Willis and Goldstein, 1983].

2.3.2.2 Zoned Taenite

As the kamacite grows, the Ni content of taenite increases along the equilibrium $\alpha+\gamma/\gamma$ phase boundary. The taenite between the kamacite plates is called retained taenite. As temperature decreases, the Ni diffusion rate in the retained taenite is no longer able to keep up, and equilibrium is no longer maintained in the meteorite. As cooling continues to below 400°C, Ni piles up in the retained taenite region close to the kamacite/retained taenite interface due to the slower diffusion rate of Ni in the taenite and thus the so-called "M" shaped Ni concentration profile develops in the retained taenite. The highest Ni concentration in the "M" profile is about 50 wt.% Ni according to the AEM study of Reuter *et al.*[1988]. The lowest Ni concentration in the "M" profile varies with the width of the retained taenite region and has a minimum Ni which is the original Ni concentration of the meteorite.

The retained taenite does not remain in solid solution as cooling continues, instead, it is structurally zoned. The microstructure of the retained taenite varies with its local average Ni composition indicating that different phase transformations have occurred along the Ni concentration gradient. Each distinct structural region is named according to its appearance under the light optical microscope. An optical micrograph of typical retained taenite is shown in Fig. 2.12 b). From the high Ni border moving into the center of the retained taenite, the microstructure includes clear taenite I (CT-I), cloudy zone

(CZ), clear taenite II (CT-II), and martensitic region (M) along the Ni concentration gradient. The CT-I and CT-II have been named because of its clear and bright appearance. The CZ shows dark brown color. A review of previous research on each structural region of the zoned taenite is given below. In this study the structure and composition of CT-I and CZ were investigated to gain a better understanding of their formation, thereby phase transformations at low temperatures.

Clear Taenite - I (CT-I)

Peterson *et al.* [1977] and Albertsen *et al.* [1978] first found that an ordered FeNi (γ') phase existed in the CT-I region of Cape York iron meteorite (IIIA) using Mössbauer spectroscopy and X-ray diffraction. They later found the same ordered phase in a number of meteorites using the same techniques. Their evidence indicated that the superstructure was $L1_0$ with three possible variants as shown in Fig. 2.14. Clarke and Scott [1980] examined optically over 40 meteorites in which this $L1_0$ ordered FeNi phase was present. Their method was to look at the optical anisotropy of this phase resulting from the tetragonal ordering. The Ni composition was also measured using the EPMA. They named the phase tetrataenite because the Bravais lattice of the $L1_0$ ordered phase was tetragonal. By overlapping the centered dark field (CDF) images from each variant of the tetrataenite, it was shown that the entire CT-I region was the tetrataenite phase [Mehta *et al.*, 1980; Reuter *et al.*, 1984]. Using EDS X-ray analysis, the Ni composition across the CT-I region was measured as 52 wt.% at the kamacite/retained taenite interface, decreasing to 45 wt.% near the CZ with an increasing number of antiphase domain boundaries. The ordered domains ranged in size from about 650 nm to 15 nm [Reuter *et al.*, 1988].

The zoned taenite in chondrites is apparently similar to that in iron and stony-iron meteorites. Holland-Duffield *et al.* [1991] have first observed that, however, in the St.

Séverin (LL6) and the Kernouve (H6) ordinary chondrites, the tetrataenite rim (TR) of the zoned taenite, which corresponds to CT-I region in iron meteorites, contains three structural sub-zones (See Fig. 2.13 b) and Fig. 4.1) rather than one seen in the iron meteorites. It was originally argued that this structure was unique to the non-phosphorus containing metal particles found in the chondrites. Two possibilities for forming these zones were suggested. One is the high Ni taenite cooling into the two phase (FeNi + $FeNi_3$) region of the low temperature Fe-Ni phase diagram. The other is the presence of uniform size antiphase boundaries within the high Ni taenite. Also, abnormally wide high Ni taenite rims bordering troilite were observed. It was suggested that it was caused by the diffusion of Ni from troilite into the high Ni taenite borders at low temperatures [Afiattalab and Wasson, 1980; Duffield, 1989]. However, there is no detailed AEM study on the taenite particles in stony meteorites. One of the objectives of this study is to understand the mechanism of formation of the three subzones in the tetrataenite rim.

Cloudy Zone (CZ)

The two phase structure of the CZ, with the globular island phase in the honeycomb phase, was first revealed by Scott [1973]. However, there are contradictory experimental results about the identities of the two phases. The early studies by Scott [1973] and Lin *et al.* [1977] using conventional TEM showed that the two phases in the CZ were interpenetrating α-bcc and γ-fcc single crystals. The more recent studies using various techniques showed that the island phase was ordered tetrataenite containing about 51 ± 2.8 wt.% Ni. The discrepancy concerned the identity of the honeycomb phase. Albertsen *et al.* [1983] found a low Ni fcc phase in the CZ region of a number of meteorites belonging to various groups using Mössbauer spectroscopy. Novotny *et al.* [1982] and Reuter *et al.* [1984] showed that the honeycomb phase of the CZ had a bcc structure using electron diffraction. Reuter *et al.* [1984] measured the Ni composition of

the honeycomb phase of the Estherville stony-iron meteorite as 11.7±0.5 wt.% Ni. Based on the Ni composition and the crystal structure (bcc), they concluded that the honeycomb phase was martensite. They also concluded that the CZ was formed through spinodal decomposition of the fcc taenite phase and that the martensite transformation occurred in the low Ni honeycomb phase.

Clear Taenite - II (CT-II)

The CT-II region was originally thought to be a single crystal fcc phase containing 25 to 30 wt.% Ni. Recently, Reuter et al. [1988] observed possible ordering diffraction spots of fcc phase from the CT-II region of the Dayton iron meteorite. The CDF imaging showed <10 nm sized ordered domains. Electron diffraction could not identify whether the ordering was of the $L1_0$ or $L1_2$ type. The very small size of the ordered domains prevented detailed AEM analysis. Therefore, whether the ordering was due to the nucleation of FeNi ($L1_0$) or the nucleation of Fe_3Ni ($L1_2$) was not confirmed.

Martensitic Zone (M, α_2) / Plessite (P)

The martensitic zone contains between 25 wt.% and 15 wt.% Ni. Both lath and lenticular martensite can be present at the same time. However, lenticular martensite is generally found at the slightly higher Ni contents close to the CT-II boundary.

Massalski *et al.* [1966] first systematically discussed the possible mechanisms of plessite formation. They assumed that the two phase structure of the duplex plessite was equilibrium $\alpha+\gamma$ and the structure of the black plessite was martensite. The $\alpha+\gamma$ two phase structure could be formed through different phase transformations, either $\gamma \rightarrow \alpha+\gamma$ or $\gamma \rightarrow \alpha_2 \rightarrow \alpha+\gamma$. Lin *et al.* [1977, 1979] observed the black plessite composed of martensite and decomposed martensite, and duplex plessite consisted of two phases, γ phase nucleated in α matrix, in IIICD iron meteorites.

2.4 Determination of Cooling Rate of Meteorites

In order to understand the phase transformation processes correctly, the thermal history (cooling rate) of the system should be considered. Over the years, several investigators have proposed various methods to determine the cooling rates of meteorites using the kamacite bandwidth, the Ni concentration gradient in taenite, a combination of the central taenite Ni content and the taenite half-width, and by measuring the Pu fission track densities in certain minerals associated with the meteorites.

The kamacite bandwidth method was developed by Goldstein and Short [1967] and directly relates the kamacite bandwidth with the cooling rate. It assumes infinite diffusion distance between adjacent kamacite plates, which means there is no impingement of neighboring diffusion fields. The growth of kamacite is estimated for a series of cooling rates by solving the second order diffusion equation till the exact bandwidth is obtained. The cooling rate which gives exact bandwidth, without any impingement at the center of the taenite is established as the cooling rate of the meteorite. This method totally neglects any impingement effects and usually overestimates the cooling rate. However, this approach should be directly applicable to determine the cooling rate of very fine octahedrites and ataxites which exhibit negligible or no impingement.

Goldstein and Ogilivie [1965] estimated the cooling rates of meteorites by matching calculated Ni composition profiles in taenite with experimentally measured profiles. The Ni composition profiles in meteorites can be measured experimentally using an electron microprobe or an analytical electron microscope. Again, using numerical methods the Ni composition profiles in taenite for various cooling rates can be computed. By matching the computed profile with the measured profile, one can arrive at a cooling rate for given meteorite. This is a fairly accurate method to determine cooling

rates, since it would include the effects of impingement. However, there is an uncertainty in the width of the taenite fields. Taenite fields can be large or small depending on the spacing of kamacite nucleation sites. This method will be particularly effective for coarse octahedrites, where taenite fields are very small and the profile does not differ very from one field to another. The disadvantage of this method is that it can be rather tedious to match the profiles.

There is a so-called Wood method [Wood, 1964] which is also referred to as the taenite half width-central Ni content method. In this procedure the half width of taenite is plotted against the Ni content at the center of the taenite. The basis for this method is the close relationship that exists between the half width-central Ni content and the shape of the M-profiles. Half width-central Ni content values for different cooling rates are computed numerically and plotted, resulting in straight lines. Experimental values of half width and measured central Ni content can be determined for a particular meteorite. If these experimentally determined values are plotted on the same graph as the computed values, they will fall along one of the computed lines. The cooling rate of the meteorite can now be estimated. There are two chief advantages in using this method. First, it uses data from a number of structures thereby lessening the chance of being misled by geometric oddities. Second, the consideration of effective initial dimension of the impingement distance is eliminated.

It was demonstrated in the early 1960s that fission fragments leave behind narrow, continuous trails of damage when they travel through micaceous minerals [Fleischer and Price, 1964]. These trails or fission tracks can be easily revealed by selective chemical etching. The primary interest of fission tracks is in mineral dating. Recently this approach was adopted by Pellas and Storzer [1981] for determination of cooling rates of meteorites. The basic principle of the method is as follows: ^{244}Pu, with a half life of approximately 82 Myr leaves fission tracks records in uranium rich and plutonium rich phosphates

(whitlockite and apatite) and adjacent mineral track detectors (olivines, pyroxenes and feldspar). In a cooling environment the ^{244}Pu fission track density in the detectors is a function of the ^{244}Pu decay and precisely defines the time lags between the onset of track retention in the respective minerals. Since the fission track retention temperatures for the minerals are known, the time elapsed in the temperature range of interest can be determined by measuring the fission track densities. Thus one is able to estimate the cooling rate of a meteorite. There are however experimental difficulties in using this method. Dislocation etch pits can often be confused with the track densities thereby leading to erroneous results. Also the exact track retention temperatures for the minerals used in this process are not easily determined. Furthermore, large phosphates and other minerals which retain the tracks are needed. Hence this approach may not be very accurate for the meteorites which do not contain abundant phosphates. However, this technique has been applied to ordinary chondrites.

2.5 Analytical Electron Microscopy

2.5.1 Quantitative X-Ray Microanalysis

The ratio technique for quantitative X-ray microanalysis in AEM was first proposed by Cliff and Lorimer [1975]. This technique relates the ratio of the concentration of the element present in the specimen to the ratio of the intensity of the characteristic X-ray count collected:

$$\frac{C_A}{C_B} = k_{AB}\frac{I_A}{I_B} \qquad (2\text{-}7)$$

where C is the concentration of the element in wt.%, I is the characteristic peak intensity, A and B are the elements present in the specimen. k_{AB} is a proportionality factor termed the Cliff-Lorimer k-factor which accounts for the difference in generation and collection of

the characteristic X-rays between element *A* and *B*. The k-factor depends on the operating voltage but is independent of the thickness or chemical composition of the specimen. The k-factors are usually determined experimentally using standards of known composition. They can also be evaluated theoretically [Goldstein *et al.*, 1977]. For a specific characteristic X-ray line *i* being analyzed (i.e. $i = K_\alpha, L_\alpha$ etc.):

$$(k_{AB})_i = \frac{(Q_i \omega_i a_i \varepsilon_i)_B / A_B}{(Q_i \omega_i a_i \varepsilon_i)_A / A_A} \qquad (2\text{-}8)$$

where A is atomic weight, Q_i is the ionization cross section, ω_i is the fluorescence yield, a_i is the ratio of intensities of *i* line and its line family, e.g. $K_\alpha/(K_\alpha+K_\beta)$, and ε_i is the EDS detector efficiency for the element. Of these terms the EDS detector efficiency and the ionization cross section are the most difficult to calculate. The most accurate method for determining the k-factor is through experimental measurements.

In order to use the Cliff-Lorimer equation, an assumption must be made that the specimen is 'infinitely thin' so that absorption and fluorescence effects are negligible. Because no specimen is infinitely thin, criteria have been developed whereby the analyst can judge if the thin film criterion still holds even for some finite specimen thickness [Goldstein, 1979]. Practically, a thin-film criterion is established which states that the specimen is considered to be "infinitely thin" if the calculated absorption and fluorescence corrections on X-ray intensity ratio are less than the statistical error of the peak X-ray counts. Romig [1979] calculated that the maximum allowable thickness which satisfied the thin film criterion was 200 nm in the Fe-Ni system, even at Ni contents as low as 2 wt.%. Since the allowable foil thickness increases with increasing Ni content, no absorption or fluorescence corrections are required by examining only areas thinner than 200 nm.

2.5.2 Spatial Resolution

When a beam of high energy electron strikes the surface of a sample, the resulting X-rays come from the volume of the sample that interacts with the incident electron beam [Goldstein *et al.*, 1977]. This "interaction volume" defines the region from which chemical information is acquired and is larger than the incoming beam diameter. The spatial resolution of X-ray microanalysis is determined by the size of the beam-specimen interaction volume. This volume is a combination of the incident electron beam diameter, d, and the beam broadening, b, due to elastic scatter within the specimen [Goldstein, 1979; Goldstein *et al.*, 1984]. Both the X-ray spatial resolution could be improved and the analysis procedure for chemical analysis simplified by use of thin samples as specimens for X-ray microanalysis [Duncumb, 1966]. Definitions of spatial resolution have been proposed by several authors [Goldstein *et al.*, 1977; Reed, 1982; Michael *et al.*, 1990; Williams *et al.*, 1991]. The average size of the interaction volume R, midway through the thin foil as shown in Fig. 2.15, can be given by

$$R = \frac{[d + (d^2 + b^2)^{1/2}]}{2} \qquad (2\text{-}9)$$

This definition of R ignores the effects of diffraction and fast secondary (FS) electrons [Joy *et al.*, 1982]. Recent Monte Carlo calculations show that FS are only significant for elements below atomic number 13 (Al) [Williams *et al.*, 1991]. There have been many definitions and theoretical calculations of b. Some definitions of b include a diameter which contains only 75-80% of the emerging electrons [Faulkner *et al.*, 1977; Hutchings *et al.*, 1979], while other definitions include 90% [Newbury and Myklebust, 1980; Reed, 1982]. However, the most widely used definition of b is that derived from the single-scattering model developed by Reed [1982] from the original paper by Goldstein *et al.* [1977]. Using Reed's single-scattering model, the beam broadening b in cms is given by

$$b = 7.21 \times 10^2 \frac{Z}{E_o} \cdot \left(\frac{\rho}{A}\right)^{1/2} \cdot t^{3/2} \qquad (2\text{-}10)$$

where ρ, A and Z are the average density (gm/cm^3), atomic weight (gm) and atomic number of the specimen, E_o is the accelerating voltage in keV and t is the thickness of the specimen in cms. In order to minimize R according to Equations (2-9) and (2-10), one should use as thin a specimen as possible, as high an electron beam energy as possible, and as small a beam diameter as possible. High brightness sources of electrons, such as a field emission gun (FEG), produce the smallest probe diameters for the same beam current and clearly provide for the highest spatial resolution as long as beam broadening is not a dominant factor. X-ray spatial resolution in the 2 to 3 nm range can be obtained with current instrumentation using a FEG. For example, a spatial resolution of 2.5 nm was obtained from a 20 nm thick sample analyzed in a VG HB501 FEG AEM at 100 keV using probe diameter of 1.8 nm full width half maximum (FWHM) [Zhang *et al.*, 1988].

2.5.3 Counting Statistics

The accuracy of the quantitative data obtained is ultimately limited by the counting statistics of the X-ray collection process, both in terms of experimental determination of the k-factor, and the acquisition of the raw intensity data for each element. Assuming Gaussian statistics, one can follow the treatment of Romig and Goldstein [1980] which is a classical treatment of the errors involved in EDS spectral processing. If the peak for element A is Gaussian, the standard deviation σ is given by

$$\sigma_A = \sqrt{I_A} \qquad (2\text{-}11)$$

where I_A is the total number of counts for element A either in the manually selected window or the full peak after background subtraction. At the 3σ confidence level, usually

taken to be about the 99% confidence level, the error in the number of accumulated counts for element A would be $3\sqrt{I_A}$. The relative error in I_A is given by

$$\text{Relative Error } (\%) = \pm\frac{3\sigma_A}{I_A}\times 100 = \pm\frac{3\sqrt{I_A}}{I_A}\times 100 \qquad (2\text{-}12)$$

Therefore the greater I_A the lower the relative error. According to the law of propagation of errors [Mandel, 1984], the total error in the ratio of compositions defined by Cliff-Lorimer relation (Equation (2-7)), C_A/C_B, for a single measurement is given by

$$\sigma_C = \frac{C_A}{C_B}\left[\left(\frac{\sigma_k}{k_{AB}}\right)^2 + \left(\frac{\sigma_A}{I_A}\right)^2 + \left(\frac{\sigma_B}{I_B}\right)^2\right]^{1/2} \qquad (2\text{-}13)$$

Therefore, the total relative error is the sum of the errors in I_A, I_B, and k_{AB}. The error in k_{AB} is again the sum of the errors in I_A and I_B used when acquiring the X-rays from the standard of known composition. This assumes negligible errors in the standard which is obviously not always the case [Williams, 1984]. Unless otherwise noted, in this study, all of the errors in the AEM data were determined in this way.

2.5.4 Artifacts due to Thin Foil Preparation

It has long been a question in AEM whether the thin foil specimens represent the characteristic structural and chemical features of the bulk materials after thinning processes involving severe chemical or physical reactions. Although a positive answer is now widely accepted due to the great success of AEM in solving real problems, several effects need to be carefully considered before the interpretation of the results obtained by AEM, such as microstructure and chemical composition, is attempted.

Ion beam milling has come into widespread use for preparation of electron transparent foils of specimen materials that are not amenable to electropolishing methods. It has been applied to integrated circuit devices composed of several different semiconductors and metals and for preparation of cross section specimens of various materials. However, there are several artifacts which may occur. Briefly these are the rise in specimen temperature during thinning, ion implantation and the development of a surface structure. Barber [1970] has measured temperature rises at the specimen position of more than 100°C. More recently, It has been reported that a standard ion beam thinning technique using room temperature stage could increase the temperature of Au/Si interface specimens to at least 370 °C by observations of eutectic melting at the interface and that interface instability could be completely suppressed by use of a low temperature thinning stage [Kim and Carpenter, 1987].

In practice some ion implantation will usually occur, although the disturbed layers should only be a small proportion of the volume. Argon in the form of bubbles is often detected after conventional ion milling [Goodhew, 1985]. The implantation of ions may lead to misleading peaks in X-ray analysis.

Ion beam damage called "black dot" defects, attributed to the clustering of point defects introduced by irradiation, have also been observed after ion milling [Cullis *et al.*, 1985; Chew and Cullis, 1987; Cullis and Chew, 1988]. They are usually ~10 nm across and are only visible in crystalline materials which give rise to diffraction contrast. The foils may also contain a high density of dislocations which are near to the foil surface [Baxter and Stobbs, 1985]. Ion beam damage resulting in development of non-flat surface which appeared to be ripples or an array of cones has been observed [Kelly and Auciello, 1980]. The damage depth can be reduced by tuning the thinning conditions during the final stages of foil preparation. The image artifacts may also arise from the formation of a thin amorphous layer or surface contamination (redeposition) during ion beam milling.

The surface layer can be formed by various mechanisms in different specimen preparation techniques. The redeposition problem has been reported in the Al-Cu system where a surface layer of Cu was formed during electropolishing [Thompson *et al.*, 1977]. A similar problem has been found in the Al-Zn and the Al-Ag systems with both electropolishing and ion beam milling [Morris *et al.*, 1977]. Since it is desirable to perform EDS X-ray analysis in very thin specimens to achieve high spatial resolution, any surface layer introduced by sample preparation process will affect the chemical composition. The thinner the specimen is, the larger the effect.

3. EXPERIMENTAL PROCEDURES

3.1 Selection of Meteorites

The phase transformation processes and phase equilibria of the Fe-Ni system at low temperatures can be better understood by characterizing the microstructure and chemistry of metallic phases in meteorites using AEM and other techniques, and evaluating the cooling rate of meteorites. In this study, various types of meteorites were selected for microstructural and microchemical analysis to reveal the low temperature transformations in the Fe-Ni system, by considering the cooling rates, the Ni content and the degree of metamorphism.

3.1.1 Iron Meteorites

Metallic phases in iron meteorites have been investigated by many research groups using the transmission electron microscopy [Jago, 1974; Albertsen *et al.*, 1983; Goldstein *et al.*, 1985; Reuter *et al.*, 1988; Zhang *et al.*, 1988, 1990]. Therefore there are significant data available on the fine-scale structures that formed in the retained taenite region. In this study, iron meteorites selected were examined by high resolution scanning electron microscope (HRSEM) in order to measure the size variation of the island phase in the cloudy zone (See section 3.4). 14 iron meteorites including Toluca (I), Carbo (IID), Cape York (IIIAB), Cumpas (IIIAB), Spearman (IIIAB), Grant (IIIAB), Tazewell (IIICD), Dayton (IIICD), Duchesne (IVA), New Westville (IVA), Chinaulta (IVA), Bishop Caynon (IVA), Gibeon (IVA), and Bristol (IVA) were chosen for this study as shown in Table 3.1 by considering the cooling rates and the Ni content. The IVAs were selected because they are known to be fast cooled.

3.1.2 Stony Meteorites

Each chondrite contains metal grains that formed in a wide variety of environments and experienced a wide range of thermal events prior to accretion in the asteroid [Wood, 1967]. Fig. 3.1 shows a schematic thermal history of chondrites. After primary heating, Chondrules cooled at rates of 100~1000°C/hour and were then accreted to form chondrite parent bodies. [Radomsky and Hewins, 1990]. The parent bodies were initially cold [Haack *et al.*, 1992] and were reheated to approximately 400°C to 900°C and then cooled slowly [McSween, 1987]. The composition and structure of metallic particles in chondrites record shock and thermal events in the parent body at relatively low temperatures. The reheating temperature range is different from one chondrite to another and the cooling rate is determined by its depth of burial, the total size of the parent planet and its content of radio nuclides (heat sources), the thermal diffusivity of its substance, and the initial temperature of the system. The final structure of metal particles is mainly determined by the processes in the regions D and E in Fig. 3.1.

The difficulty in understanding the structure and the thermal history of the metal particles in chondrites depends on the degree of reheating or metamorphism. Since the high metamorphic grade chondrites, types 5 and 6, underwent reheating into the single phase taenite region [McSween, 1987], all traces of the microstructure produced within the metal particles during the initial cooling have been completely erased, and the microstructure is relatively easy to understand. In contrast, the metal particles in the low metamorphic grade chondrites, type 3 and 4, are reheated to temperatures below 700°C where they are in the two-phase ($\alpha+\gamma$) region of the Fe-Ni phase diagram. Thus, the metal particles of type 3 and 4 chondrites are very complex structurally and chemically. Consequently, the higher metamorphic grade chondrites were investigated.

In this study, 3 type 6 chondrites (Saint-Séverin, Guareña, and Kernouve) were selected for microstructural and microchemical analysis as listed in Table 3.2. All three chondrites are well known and have been studied by other investigators [Duffield, 1989;

Holland-Duffield *et al.*, 1991] using LOM, SEM and EPMA, but no AEM. The Saint-Séverin chondrite was selected for AEM study because it is in LL group which contains relatively large amount of metallic particles. The other chondrites were investigated using HRSEM recognizing the inherent differences and the similarities with other meteorites.

3.1.2 Stony-Iron Meteorites

Stony-iron meteorites have nearly equal proportions of metals and silicates. There are two types of the stony-iron meteorite: pallasites and mesosiderites. In this study, 9 stony-iron meteorites including 6 mesosiderites (Patwar, Barea, Chinguetti, Pinnaroo, Estherville, RKPA79015) and 3 pallasites (Imilac, Newport, Glorieta Mountain) were selected for HRSEM and AEM investigations. All these meteorites are listed in Table 3.3. Thin foils for AEM study were made out of the Estherville and the RKPA79015 mesosiderites. There are relatively more and larger metallic phases in mesosiderites than in chondrites. The metallic grains in mesosiderites usually reach centimeter-size. Therefore it is relatively easy to make the thin foils of the metallic phases in mesosiderites (See section 3.2). In addition, since the cooling rate of mesosiderites is extremely slow, they have much coarser and well developed microstructure than any other meteorites, which could help in investigating the fine metallic phases produced at low temperatures and understanding the phase transformations.

3.2 Bulk Sample Preparation for SEM/EPMA

The meteorite samples were epoxy-mounted, ground with SiC paper, and polished with 6 μm diamond paste, 1 μm alumina powder and finally 0.05 μm silica. The sample was then etched with 2% Nital for various times, usually less than ten seconds for the optical microscope observation and a little longer for scanning electron microscopy (SEM) observation. The samples for compositional analysis using an electron probe

microanalyzer (EPMA) or an energy dispersive spectrometer (EDS) on a SEM were not etched. Most of the SEM and EPMA samples were coated with carbon after polishing using a vacuum evaporator (Denton Vacuum DV-502). However, the iron meteorite samples for low keV SEM were not coated.

3.3 Thin Foil Preparation for AEM

Since the microstructures of the metallic phases which were formed by low temperature phase transformations are sub-micron in size due to the very low diffusivity of the system, the application of various AEM techniques for structural and chemical characterization is critical to this experimental work. Numerous AEM studies of iron meteorites can be seen in the literature [Lin *et al.*, 1977, 1979; Romig and Goldstein, 1980; Novotny *et al.*, 1982; Albertsen *et al.*, 1983; Goldstein *et al.*, 1985; Reuter *et al.*, 1988; Kowalik *et al.*, 1988; Zhang *et al.*, 1988, 1990]. However, only a few TEM/AEM studies of stony-iron and stony meteorites has been reported [Mehta *et al.*, 1980; Duffield, 1989]. Thin specimen preparation is a very important step and not just a minor part of the TEM/AEM work, because specimens produced improperly may lead to a misunderstanding of microstructure and microchemistry. In the following sections, the procedure of thin foil preparation for successful AEM study is described.

3.3.1 Thin Foils with Metallic Phases in Mesosiderites

The metallic phases in the selected mesosiderites, Estherville and RKPA 79015, were large enough to make 3 mm discs containing the area of interest inside. After optical examination to determine if taenite areas existed in the sections, the appropriate sections were sliced to about 200 μm with a slow speed diamond saw. These wafers were polished, briefly etched, and then examined optically and areas of interest were marked with a permanent felt-tip marker. The 3 mm discs were cut from the wafers using an

electro-discharge machine (EDM) with the marked area being carefully aligned in the middle of the disc. The discs were ground down to 50 - 100 μm and photographed after brief etching. Since the meteorites do not have a uniform microstructure throughout the disc, it is worth to compare the discs before and after perforation to confirm that the perforation is in exactly right place.

Thin foils were prepared in two different ways: one is electro-chemical thinning and the other is ion beam thinning. In the case of electro-chemical thinning, a Fischione twin jet electropolishing unit was used. The electrolyte was 2% perchloric acid ($HClO_4$) in ethanol. The polishing condition was 100V and -20°C for which a current of about 50mA was obtained. Only two specimens were successful, which means the initial perforation was at a desired area. The other specimens of which the initial perforation was not at the right place were further thinned by ion beam milling until an area of interest was thin enough. In the case of ion beam thinning, the disc was first dimpled down to ~10 μm using either a Gatan model 656 dimple grinder or a VCR Group DIMPLER® model D500i. The latter provided more accurate control of the final thickness. Dimpling was performed on only single side of the specimen. After dimpling, the disc was ion beam thinned using a Gatan model 600 DuoMill™. Ion beam thinning was always performed on the liquid nitrogen (LN_2) cooled stage to suppress any possible phase transformation due to the local heating by Ar^+ ion beam bombardment. It has been reported that a standard ion beam thinning technique using a room temperature stage can increase the temperature of Au/Si interface specimens to at least 370 °C by observations of eutectic melting at the interface, and that interface instability can be completely suppressed by use of a low temperature thinning stage [Kim and Carpenter, 1987]. In order to minimize the redeposition problem, the cold trap was filled with LN_2 to collect sputtered particles coming out of the specimen and holder throughout the ion beam thinning. The thinning was performed using two guns at 5 kV gun voltage, 15° incident angle, and 0.5 mA gun

current for each gun until initial perforation occurred. The initial perforation was detected by Laser autoterminator which automatically terminates milling when it senses the perforation. Once perforation occurred, the gun voltage was dropped to 4 kV, and the incident angle was changed to 11° to reduce possible damage from ion beam thinning.

3.3.2 Thin Foils with Metal Particles in Chondrites

Chondrites are composite materials consisting of metal particles which are sub-millimeter size, in a silicate matrix. The area of interest in this study is not the silicate matrix but the metal particles. Materials of this type present particular difficulties in the preparation of thin foil specimens because the area of interest is limited to the specific regions within the metal particles. The metal particles are usually less than 500 μm and the silicate matrix is inherently brittle. Moreover, the interfaces between metal particles and silicates are weak. Thus, a supporting medium which is able to hold the metal particles throughout the thinning process is necessary to make a 3 mm disc which fits in most TEM/AEM. There has been one attempt at making thin foils for investigation of the metal particles [Holland-Duffield *et al.*, 1991], but no success has been reported.

There are important factors to be considered when preparing thin foils with such materials. First, the sample must be strong enough to withstand the necessary mechanical handling and thinning. Secondly, the differential thinning rate problem caused by the composite nature of the sample must be overcome. In other words, both the metal particles and the matrix must be thinned at a similar rate so that the matrix may have enough thickness to support the metal particles. Thirdly, it is better to achieve as large an electron transparent region in the metal particle as possible. Finally, artifacts caused by thinning processes must be minimized.

Due to the difficulty in the preparation of thin foils of the metal particles and the limited amount of material available from the Saint. Séverin chondrite, every stage of the

preparation technique was practiced thoroughly using some thin sections of the Farmington chondrite and Fe-Ni alloys before any attempt was made to produce thin foils from Saint. Séverin.

Stage 1: Extracting Metal Particles

The metallic particles of the St. Séverin ordinary chondrite were provided by R. B. Scorzelli, CBPF in Brazil. After breaking the meteorite sample, a first magnetic separation was performed to collect the metallic fraction. And then the metallic fraction was boiled in concentrated HF solution for a few minutes to dissolve the residual silicate around the metal particles. Finally, the residue was submitted to another magnetic separation. After the chemical and magnetic treatment, the metallic particles were examined under a light optical microscope (LOM) to evaluate the separation. The LOM examination showed that the proportion of free surface of the metal particles is above 80%. It is important for the metal particles to be free from silicate to secure a strong bonding between metal particles and supporting materials. The next step is preparing 3 mm discs with the small metal particles.

Stage 2: Producing 3 mm Discs

A variety of methods have been developed for the preparation of thin foil specimens from complicated materials, such as multilayered materials [Baxter and Stobbs, 1985; Chang *et al.*, 1988; Ostreicher and Sung, 1993; Yu *et al.*, 1991; Hefter *et al.*, 1992], semiconductors [Ivey and Piercy, 1988; Barna and Pécz, 1991], small oxide crystals [Krumeich and Mertin, 1991], and fine particles [Kelly *et al.*, 1988; Kamenetzky *et al.*, 1988; Alani, 1990a; Shield *et al.*, 1993]. Most of them used various embedding materials to hold the samples together during the subsequent thinning process. In order to make the 3 mm disc with the extracted metal particles, in this study, several embedding materials,

such as G-1 epoxy (Gatan), 2 ton clear epoxy (Devcon), Torr Seal (Varian) and Epo-Tek H20E silver glue (Epoxy Tech.) were tested. The different embedding materials have different properties. The G-1 epoxy and Epo-Tek H20E silver glue showed a strong bonding and was easy to use (short curing time and low viscosity). However Epo-Tek H20E silver glue was preferred for its good electro-conductivity which allowed the specimen to be thinned by electro-chemical polishing technique (See next section). Meanwhile, it was very difficult to grind dimples into Torr Seal samples because it tended to clog the grinding/polishing wheel. The 2 ton clear epoxy samples were easily broken apart during dimpling. Both the Torr Seal and the 2 ton clear epoxy has proved unacceptable to this study.

The extracted metal particles were placed in the center of a shallow brass mold (made of brass tube; 3 mm outer diameter, 1 ~ 2 mm height) which was stuck on the glass plate as shown in Fig. 3.2. The mold was then filled with embedding materials and cured. After curing, these discs were fixed to a specimen mount (a thick glass plate) using mounting wax called Crystal-Bond (Gatan; melting point ≈ 130°C). Both sides of the specimen were ground down to a residual thickness of 100 ~ 150 μm. Fig. 3.4 a) is a light optical micrograph of polished TEM sample which shows the metal particles surrounded by the Epo-Tek H20E silver glue. The bright contrast in embedding material is from Ag particles in the Epo-Tek H20E silver glue. With the dimple grinder (either a Gatan model 656 dimple grinder or a VCR Group DIMPLER® model D500i.) the discs were further thinned to a residual thickness of about 30 ~ 50 μm. It is practical to grind a hemispherical depression into the specimen disc to produce a minimum thickness in the center while a thicker border for good mechanical strength and specimen handling is retained [Goodhew, 1985].

In addition to the simple epoxy mounting technique, there were attempts at preparing 3 mm discs in different ways, such as cold compaction and sandwich-type

reinforcement. However, the technique of cold compection of the metal particles mixed with high-purity ductile Ag metal powder, which is similar to that proposed by Kamenetzky *et al.* [1988] and Shield *et al.* [1993], has proved unacceptable for this study. The sandwich-type samples were prepared by conventional cross-sectioning techniques [Bravman and Sinclair, 1984; Alani, 1990a; Alani *et al.*, 1990b]with only a few modifications. Fig. 3.3 is a schematic illustration of the sandwich-type sample preparation technique. A thin slab containing extracted metal particles in the center was prepared as shown in Fig. 3.3 a). The inner part was then assembled by gluing the slab and the half-cut brass rods that fitted originally in the brass tube(See Fig. 3.3 b)) together and inserted into the brass tube (outer diameter: 3 mm). Based upon tube geometry, the ideal thickness of the slab is the width of the portion which has been removed by the diamond saw. This means that the final sample to be inserted into the tubing should have the size of the inner diameter of tube so that a full, tight fit of the sample is obtained. Finally, after curing, the assembly was sliced into a series of 200 μm to 300 μm thick discs using a thin blade diamond saw. The sliced discs were then ground to about 100 μm from both sides. The 100 μm thick discs were dimpled and ion beam thinned to perforation. More details about dimpling and ion beam thinning are given below.

Stage 3: Thinning Processes

The technique of mechanical dimpling prior to conventional ion beam thinning described by Bravman and Sinclair [1984] was selected for thinning the metal particles in the embedding materials but proved unsuccessful because of preferential thinning of the embedding material portion. In conventional ion beam thinning, Ar ions with energies of 3 ~ 6 keV only penetrate a few nanometers into most materials and, by collision, one or more atoms in the target may be ejected from the surface by each incident Ar ion. The sputtering yield (atoms ejected per incident ion) depends on the relative masses of the ion

and target atom, on the ion beam energy, on the atomic density and crystalline structure of the specimen and on the angle of incidence of the beam on the specimen surface [Goodhew, 1985]. The maximum sputtering yield for bombardment with Ar ions with respect to the atomic number shows a periodicity related to the filling of the d electron shells [Kanaya *et al.*, 1974]. Therefore, it is obvious that the preferential thinning occurs during the thinning process, since the atomic density and crystalline structure of the metal particles and the embedding material are so different.

In order to prepare the thin foil specimens which have such problems, various ion beam thinning techniques which have been used to the specimens having similar problems were applied, which included non-rotational ion beam thinning [Yao and Dunlop, 1991], shielded ion beam thinning [Chang *et al.*, 1988],and low angle ion beam thinning [Alani, 1990a].

The specimen stage in ion beam milling machine is rotated because the development of distinctly non-flat surface topographies during ion bombardment, e.g., arrays of cones or spikes, originating from surface asperity[Kelly and Auciello, 1980], can be suppressed by rotation. A drawback of rotation is that if the specimen consists of materials having large differences in thinning rates it may amplify the problem. This is because rotation, of a layered specimen, allows the specimen to be sputtered with the beam parallel to layer with a higher thinning rate and removes this layer faster than the layer with a low thinning rate. In the technique of non-rotational ion beam thinning, the specimen stage is not rotated and a single ion gun is used to sputter the specimen from the direction perpendicular to the epoxy layer. However, the result was not successful. Although this technique somewhat alleviated the differential thinning rate problem, non-flat surface topographies developed and made a TEM examination difficult.

In the shielded ion beam thinning technique, the basic idea is the same as the non-rotational ion beam thinning technique but the specimen stage is rotating. The preferential

thinning can be suppressed by shielding the epoxy layer from the ion beam coming in the direction parallel to that layer. The platform of the specimen holder was modified such that two pieces of beam shield which were made of Mo plate were glued on its surface as shown in Fig. 3.5. Since the specimen stage was rotating, the surface of the specimen appeared to be better than that obtained by non-rotational ion beam thinning technique but was still too harsh to use as a TEM specimen.

It has been suggested that the differential thinning problem could be overcome by low angle ion beam thinning technique [Alani *et al.*, 1990b]. The low angle specimen holder (Gatan, see Fig. 3.6) was tested. However, in practice, it was very difficult to lower the incident angle of ion beam down to 5° or less with the specimen being focused. Moreover, with such low incident angles milling time was too long (more than 40 hours). Therefore, this technique was only used as a final thinning step to smooth out the damaged surface resulting from high angle ion beam thinning.

For all three techniques above, dimple grinding was carried out prior to ion beam thinning. The dimple grinding was necessary because the specimen must be as thin as possible to reduce the milling time. An alternative technique which could reduce the thinning time and thus minimize the differential thinning rate problem was dimpling the specimen to perforation prior to ion beam thinning, which was similar to that described by Ivey and Piercy [1988]. In practice, however, it was very difficult to control the final thickness of the specimen down to 10 μm with dimplers available. The specimen became very fragile as thickness decreased. Almost all specimens prepared by this technique were broken during or after dimpling.

In another approach, if the specimen is electrically conducting, the metal particles can be thinned down preferentially by use of electro-chemical polishing prior to ion beam thinning. This technique offered the possibility of overcoming the differential thinning rate problem. Although the ion beam thinning sputtered embedding materials faster, the

metal particles were preferentially attacked and became so thin during electro-chemical polishing that it was possible to preserve the embedding material which held the metal particles during ion beam thinning. Taking advantage of the characteristics of the Epo-Tek H20E silver glue, e.g., a high bonding strength and a electro-conductivity, successful thin foil specimens could be obtained by only electro-chemical polishing itself or a combination of electro-chemical polishing and ion beam thinning. The electro-chemical polishing was carried out using a Fischione twin jet electropolishing unit with 2% perchloric acid ($HClO_4$) in ethanol at 100V and -20°C. After jet polishing, the specimen was examined under a light optical microscope comparing to the image taken before thinning to see if the perforation was in exactly the area of interest. If so, the specimen was examined using a TEM. If not, further ion beam thinning was performed until an area of interest was thin enough. Fig. 3.4 b) shows the St. Séverin specimen prepared by this technique. The arrowhead indicates the area of interest which is electron transparent.

In summary, the difficulties in thin foil preparation of metal particles of the chondrite were overcome by developing a technique involving electrochemical polishing prior to ion beam thinning with the specimen embedding in Epo-Tek H20E silver glue. A schematic illustration of the thin foil preparation is shown in Fig. 3.7. Specimens prepared by this technique have permitted the direct observation and characterization of the metallic phases in the chondrite, and to the author's knowledge are the first such published data.

3.4 Structural and Chemical Analysis

In order to gain an understanding of the phase transformations in meteorites at low temperatures, various electron-optical techniques, such as electron probe microanalysis (EPMA), scanning electron microscopy (SEM), transmission electron microscopy (TEM), and analytical electron microscopy (AEM) were employed.

In the case of phase transformations that occurred above ~500°C in Fe-Ni meteorites, the resultant structures can be observed optically and the phase compositions can be measured with EPMA [Goldstein *et al.*, 1985]. Below ~500°C, however, the transformations in Fe-Ni meteorites occur on a scale of <~1μm and so are beneath the resolution limit of a typical optical microscope and the EPMA. Therefore, both microstructure and microchemistry are only accessible through higher resolution SEM, TEM and AEM techniques. In the following sections, the experimental procedures of various electron microscopy techniques are described.

3.4.1 SEM and EPMA

After etching with 2% Nital, the microstructure of the retained taenite was examined optically and/or with the SEM. The low Ni phase on the surface of the meteorite specimens is preferentially etched away and thus the surface topography is developed. To observe the surface topography, the secondary electron imaging (SEI) mode of the SEM was used.

An ETEC SEM with a W filament was used for basic examination of the microstructure. The typical spatial resolution of the ETEC SEM in SEI mode is 10 ~ 20 nm. A digitally controlled JEOL 6300 FEG-SEM equipped with an image analysis computer and an ultra thin window EDS, and a JEOL 840F FEG-SEM were employed for a detailed study of the microstructure. Due to their ability to form a very fine probe with high probe current, these SEMs have a potential spatial resolution of ~1 nm yielding SEM micrographs of 200,000X magnification or higher. Moreover, the JEOL SEMs which have a high brightness electron source can also achieve high resolution images at significantly lower accelerating voltage, as low as a few hundred eV [Nagatani *et al.*, 1987]. As discussed in the section 2.6, there are many advantages of the low voltage

SEM. Most of the SEM images using JEOL SEMs were taken at 1 ~ 5 kV accelerating voltage to observe fine details on the surface of the specimens.

Taking advantage of the high capability of HRSEM, once adequate TEM and AEM characterizations of a few meteorites are done, the HRSEM can be used to characterize a large suite of meteorites. The overlap in the magnification range between HRSEM and AEM allows for microstructural characterization of a large number of metallic phases, although HRSEM cannot analyze the structure or chemistry of the phases.

A fully automated JEOL 733 superprobe electron probe microanalyzer (EPMA) equipped with four wavelength dispersive spectrometers (WDS) and Tracor Northern TN2000 computer was used for chemical analysis of bulk specimens. For the analysis of elements Fe and Ni, pure metallic Fe and Ni were used as standards. The analysis was performed at 15 kV accelerating voltage and 40 ~ 50 nA beam current. The data were processed (ZAF correction) by Bastin's $\phi(\rho z)$ method [Bastin *et al.*, 1984] which was contained in a software package called Sandia Task.

3.4.2 Analytical Electron Microscopy

Since the phases produced at low temperatures are very fine, they can be most effectively studied using various AEM techniques. The fine structure and high spatial resolution chemistry of the metallic phases were characterized using the following facilities. A Philips EM400T AEM with a LaB_6 electron source and equipped with EDAX Li-drifted Si EDS detector controlled by a LINK AN10/85S MCA/computer system was used. It is capable of analyzing regions in the metallic phases of meteorites with a X-ray spatial resolution as small as 20 to 30 nm. The EM400T AEM was operated at 120 kV accelerating voltage.

A Vacuum Generators (VG) FEG-HB501, equipped with a Gatan 666 parallel collection electron energy loss spectrometer (PEELS) and a KEVEX Li-drifted Si EDS detector controlled by a KEVEX 8000 MCA/computer system, is one of the first of a new generation of instruments (dedicated STEM) and has a potential spatial resolution as small as 2 nm on thin meteorite samples [Zhang *et al.*, 1988]. The VG HB501 was operated at 100 kV accelerating voltage.

Quantification of the X-ray intensity data from the AEM requires prior knowledge of the Cliff-Lorimer k-factor. The k-factor for Ni with respect to Fe, k_{NiFe}, was determined for each instrument that was used using standard thin foils of known composition (determined from the EPMA). The standards used were Fe-28 wt.% Ni alloy and Fe-7 wt.% Ni alloy. Absorption by the EDS detector not only varies significantly with individual detectors but also varies with time for the same detector. The k_{NiFe} value determined in this study has shown little variation from either the theoretically calculated value or the experimental values previously determined [Reuter, 1986; Zhang, 1991]. The experimental k_{NiFe} values are 1.22 ± 0.01 for the EM400T AEM at 120 kV and 1.12 ± 0.01 for the VG HB501 at 100kV with the relative errors of 0.8 % and 1.06 % at the 95% confidence level, respectively.

The prime advantage of X-ray microanalysis using high spatial resolution AEM is the ability to measure the composition of very small particles and determine the interface compositions of various adjoining phases with high accuracy. In order to ensure the accuracy of EDS X-ray analysis, through thickness precipitates and interfaces perpendicular to the specimen surface were selected for the analysis. The specimen was carefully positioned so that the interfaces were oriented parallel to the axis of the EDS detector.

The specimen drift is an important factor which limits the practically achievable spatial resolution. Especially, epoxy supported chondrite samples showed a considerable

amount of drift. Since the epoxy is not a good thermal conductor, heat generated by electron irradiation may be built up and gives rise to distortion of the specimen. The specimen drift was corrected manually for both the EM400T AEM and the VG HB501 STEM. During the analysis, X-ray acquisition was stopped at 30 second intervals, and the specimen drift was corrected by looking at a reference feature in the STEM image.

3.5 Cooling Rate Measurement

The cloudy zone in the retained taenite of meteoritic metal is mainly composed of two phases, the high Ni island phase and the low Ni honeycomb phase. There is a Ni concentration gradient through the cloudy zone and the size of the island phase varies with local Ni concentration. It is proposed that this size variation can be used to estimate the low temperature cooling rate of the host meteorite. The width of the island phase is governed by the cooling rate and Ni concentration. Since the Ni concentration is almost constant at the outermost region of the cloudy zone, only the cooling rate controls the size of the island phase. One of the objectives of this study is to develop a relationship between the size of the island phase in the microstructure, the composition of the cloudy zone in the retained taenite of iron, stony-iron and stony meteorites, and the cooling rate of meteorites obtained by metallographic techniques.

The cloudy zone microstructure was investigated using a JEOL 6300 FEG-HRSEM, and the local Ni concentration was measured using a JEOL 733 EPMA. A typical morphology of the island phase at which the local Ni concentration is high is a dense network of cylinders rather than a globule seen at the center of the cloudy zone (See section 4.2.1). The island phase width measured (W) is defined by the length of diametral axis of circular cross section as shown in Fig. 3.8. The island phase width was measured using high magnification (>50,000X) HRSEM images taken at the boundary between the cloudy zone and the outer taenite rim of the meteorites by use of a Micro-Plan II image

analysis system (DonSanto Co.), and the local Ni concentration was measured for each image using EPMA.

4. RESULTS

4.1 Tetrataenite Rim of Retained Taenite

4.1.1 LOM/SEM Observation of the Tetrataenite Rim

The retained taenite of meteoritic metal is composed of several structural regions which include clear taenite I (CT-I), cloudy zone (CZ), clear taenite II(CT-II), and martensite (M) along the Ni concentration gradient. The outermost region of zoned taenite has been called clear taenite I (CT-I) because it appeared to be clear and bright under the light optical microscope (LOM). All iron meteorites examined in this study (Table 3.1) showed this clear and bright rim of CT-I region when observed optically as shown in Fig. 2.12. However, Holland-Duffield *et al.* [1991] have observed that, in two ordinary chondrites, St. Séverin and Kernouve, the CT-I region consisted of three different colored zones. In this study, the same microstructure as found in the Saint Séverin and Kernouve chondrites was observed in the Guareña and Richardton ordinary chondrites. In examining the mesosiderites, moreover, a microstructure containing three sub-zones which were very similar to that in ordinary chondrites was observed. Apparently, the clear taenite I region is not truly clear. Therefore, it is suggested to rename this region the "tetrataenite rim (TR)".

Fig. 4.1 is a LOM image of the Guareña (H6) ordinary chondrite. The specimen was prepared by etching with 2% Nital for 2 minutes. The proper etching condition to observe the sub-structure in the tetrataenite rim was different from meteorite to meteorite. The image contains a zoned taenite particle, which is composed of TR, CZ and CT-II, surrounded by silicate matrix (S). In the tetrataenite rim, one can clearly see the three sub-zones, which are distinguished by their color or contrast, even though the width of the tetrataenite rim is narrower than that observed in the Saint Séverin (LL6) ordinary chondrite (See Fig. 2.13b). In examining the tetrataenite rim in the chondrites, it was observed that the Saint Séverin (LL6) has a wider TR than other chondrites which are H

type (Kernouve (H6), Guareña (H6) and Richardton (H5)). The width of the tetrataenite rim in the Saint Séverin ranges from 3 μm to 4 μm, while H type chondrites have the tetrataenite rim 1 ~ 2 μm wide. In the chondrites investigated in this study, taenite particles often consist of a number of contiguous and individually zoned taenite grains. The γ/γ grain boundaries, as marked with arrows in Fig. 4.1, run centrally within interior clear etched zones in polycrystalline taenite. The taenite particle in Fig. 4.1 (Guareña chondrite) contains the clear taenite II region as well as the TR and CZ, while the taenite particle in Fig. 2.13b (Saint Séverin chondrite) consists of the TR and CZ. It is due to the fact that the bulk Ni content of the Guareña chondrite is about 10 wt.% Ni which is lower than the bulk Ni content of the Saint Séverin chondrite (~30 wt.% Ni) [Willis and Goldstein, 1983]. In addition, the cooling rate of the Guareña (~ 4.3 K/Myr) is faster than the Saint Séverin (~1.0 K/Myr) [Willis and Goldstein, 1983]. The faster cooling rate and lower bulk Ni content of the Guareña chondrite allows the central Ni content of taenite to remain in the range of the clear taenite II, which is generally 25 ~ 28 wt.% Ni [Reuter *et al.*, 1988].

Fig. 4.2a is a SEM image of a taenite particle in the Saint Séverin (LL6) ordinary chondrite which is the same as the particle in Fig. 2.13b. Fig. 4.2b is an image taken at the edge of the taenite particle surrounded by the silicate matrix (S), showing the cloudy zone and the tetrataenite rim which contains three sub-zones (1, 2, and 3). The arrow on the left shows the position of the boundary between the outer taenite rim and the cloudy zone. The arrows give the general boundaries of zone 1/zone 2 and zone 2/zone 3. The arrow on the right shows the position of the taenite/silicate (S) boundary. The microstructure shown in Fig. 4.2 is consistent with the observations of Duffield [1989].

Fig.4.3a is a light optical micrograph of a retained taenite particle surrounded by silicate matrix in the Patwar mesosiderite. The micrograph shows three distinct sub-zones in the tetrataenite rim. Fig. 4.3b is a SEM image of the edge of the tetrataenite rim and

shows the three sub-zones (1, 2, and 3). The pair of arrows indicates a general boundary between the cloudy zone and the tetrataenite rim. All the mesosiderites investigated in this study contain three sub-zones inside the tetrataenite rim. However, the time needed for proper etching of LOM samples in order to observe the sub-zones was different from one mesosiderite to another. The proper etching time with 2% Nital was 2 minutes for the Patwar and the Barea mesosiderites, and 5 minutes for the Chinguetti, Pinnaroo, Estherville, and RKPA79015 samples.

Fig. 4.4 is a series of SEM images of the tetrataenite rim of the RKPA 79015 mesosiderite. Fig. 4.4a shows the cloudy zone (CZ), the tetrataenite rim (TR) containing three sub-zones (1, 2, 3), and kamacite (K). Figs. 4.4b, c and d are the high magnification images of three sub-zones. Fig. 4.4b shows that the microstructure of the tetrataenite rim close to the cloudy zone (zone 1) includes well dispersed dark etch pits, marked with an arrow head, and highly etched boundaries. The set of arrows indicates a general boundary between the cloudy zone and the tetrataenite rim. Fig. 4.4c was taken at the center of the tetrataenite rim (zone 2). This region also contains a lot of etch pits and many highly etched boundaries which often form loops. The regions enclosed by the highly etched boundaries are smaller and more dense in zone 2 than in zone 1. This high boundary density causes zone 2 to be darker than zone 1 in light optical micrographs. Fig. 4.4d was taken at the border between two zones; the zone 2 and the outer region of the tetrataenite rim (zone 3). Approaching zone 3, the density of etch pits decreases, and essentially no pitting is observed in the outermost part of the tetrataenite rim.

The retained taenite in this sample also showed an "M"-shaped Ni concentration profile, i.e. Ni content reaches the highest value at the kamacite/taenite interface and then decreases gradually towards the center of the taenite. Fig. 4.5 shows the M-shaped Ni concentration profile obtained with the EPMA traversing the kamacite and taenite in the RKPA 79015 mesosiderite. There is a discontinuity in the Ni content at the TR/CZ

boundary. As will be discussed later, this step in the composition profile can be interpreted as evidence for the monotectoid transformation. The step was not observed at the right side of the TR/CZ interface. This may have resulted from the interface not being parallel to the incident electron beam. In other words, if the interface is not parallel to incident electron beam during X-ray analysis, X-rays generated from both regions will be collected and thus an average composition will be obtained instead of measuring the true composition from a single region. Such a Ni discontinuity has been observed previously using EPMA [Scott, 1973; Albertsen *et al.*, 1983; Reuter *et al.*, 1988].

The sub-zone structure was observed in other types of meteorites. Fig. 4.6 is a SEM image of the tetrataenite rim in the Imilac pallasite. Although boundaries between zones are not as clear as those in the chondrites and mesosiderites, one can clearly see the dark etch pits near to the border between the tetrataenite rim and the cloudy zone. Fig. 4.7 is a SEM image of the tetrataenite rim in the Carbo (IID) iron meteorite. The microstructure of the TR is similar to other meteorites shown above. Considering the M-shaped Ni concentration profile in taenite, the density of pits decreases with increasing Ni content in the tetrataenite rim, and pitting is absent in the outermost part of the tetrataenite rim. Therefore the term 'tetrataenite rim' should be applied for all meteorites, not just chondrites.

4.1.2 AEM Study of the Tetrataenite Rim

4.1.2.1 Microstructure of the Tetrataenite Rim

Since mesosiderites are the most slowly cooled meteorites, the tetrataenite rim is much wider (about 5 ~ 10μm) and the constituents of the cloudy zone are much larger than those in other meteorites. These larger structures can be easily observed in the AEM. In this study, the RKPA 79015 and the Estherville mesosiderites were selected for an AEM study to investigate the microstructure and composition of the metallic phases

produced at low temperatures. In addition, thin foil AEM samples of the Saint Séverin ordinary chondrite were prepared to compare the microstructure and composition with those of other meteorites. This is the first AEM study of the metal particles in chondrites.

Fig. 4.8a is a TEM bright field (BF) image of the tetrataenite rim of taenite in the RKPA 79015 mesosiderite. Two sets of twin structure are seen in the image. Fig. 4.8b is a centered dark field (CDF) image using the (010) superlattice reflection marked with an arrow in Fig. 4.8c, which shows one of three variants of $L1_0$ ordered FeNi. This variant is composed of numerous antiphase domains marked with an arrow. Note that the ordered domain size varies with positions. Fig. 4.8c is a selected area diffraction pattern (SADP) showing a $[100]_\gamma$ fcc zone axis with three variants of $L1_0$ ordered superlattice reflections. Fig. 4.8d is an indexing of the SADP.

Fig. 4.9 is a set of images from the tetrataenite rim and the cloudy zone of the RKPA 79015 mesosiderite at the boundary between the two structures. The set of arrows in both images indicates a boundary between those two structural regions (TR/CZ). Fig. 4.9a is a SEM image showing a microstructure of the tetrataenite rim (zone 1) which contains a number of small etch pits (P). It is worth noting here that the island phase in the cloudy zone also contains numerous etch pits, and this will be discussed later. Fig.4.9b is a corresponding TEM bright field image. The image also contains the honeycomb phase (H) and the island phase (I) in the cloudy zone, and the tetrataenite rim (TR) as seen in the SEM image, Fig. 4.9a. The tetrataenite rim contains a number of tiny precipitates (P) which correspond to the etch pits seen in the SEM image. Fig. 4.10 is another set of TEM bright field images of the RKPA79015 mesosiderite. Fig. 4.10a shows the microstructure at the border between the cloudy zone which is composed of the island phase (I) and the honeycomb phase (H), and the tetrataenite rim (zone 1). The honeycomb phase appears to be spherical shape rather than its real honeycomb-like

shape due to the combined effect of the foil thickness and crystallographic orientation of the phase. The precipitates are widely dispersed in the island phase of the cloudy zone as well as in the tetrataenite rim. Fig. 4.10b shows the precipitate loops and some scattered precipitates at the center of the outer taenite rim (zone 2), which are consistent with the SEM image of Fig. 4.4c. Fig. 4.10c is a CBED pattern from the precipitate in the tetrataenite rim which contains both a fcc $[100]_\gamma$ zone axis pattern and a bcc $[011]_\alpha$ zone axis pattern. It seems most likely that the precipitate is a bcc single crystal and the fcc $[100]_\gamma$ zone axis pattern comes from the matrix because the size of the precipitate is small (<40 nm). However, the possibility that the fcc $[100]_\gamma$ zone axis pattern comes from the precipitate itself can not be ruled out. This implies that the precipitate is a partially transformed product. Fig. 4.10d is an indexing of the CBED pattern.

Fig. 4.11 is a series of TEM images taken at the border between the TR and the CZ. Fig. 4.11a and Fig. 4.11b are a BF image and a CDF image using a $(200)_\alpha$ reflection in the $[011]_\alpha$ bcc zone axis pattern, respectively. In the CDF image, not all but some of the honeycomb phase and some of the precipitates are illuminated confirming that the honeycomb phase and the precipitates have the same crystal structure which is body centered cubic (bcc). Fig. 4.11c is another CDF image using the (100) superlattice reflection marked with an arrow in Fig 4.11d, which shows one of the three variants of $L1_0$ ordered FeNi. The antiphase domain boundary (APB) marked with an arrow is clearly seen in the image. Comparing the CDF images, the precipitates are seen to be located everywhere. However, it is likely that the APBs are responsible for the precipitate loop in the TEM images and dark, deep grooves in the SEM images. Fig. 4.11d is a SADP and Fig. 4.11e is a schematic diagram of the SADP which includes the $[100]_\gamma$ fcc matrix pattern, $[100]_\alpha$ and $[011]_\alpha$ bcc zone axis patterns, $L1_0$ superlattice reflections, and oxide spots. Fig. 4.11f is an indexing of the $[100]_\gamma$ fcc matrix pattern and superlattice reflections, and the $[100]_\alpha$ bcc zone axis pattern. Fig. 4.11g is an indexing of the $[011]_\alpha$

bcc zone axis pattern which shows a twinning orientation relationship. The twinning planes are $(020)_\gamma$ and $(220)_\gamma$. The amorphous film on the surface, which is responsible for a set of weak diffraction spots, is probably caused by ion beam thinning. Attempts to remove the oxide film by irradiating at smaller angles of beam incidence and with ions of lower energies were not successful. Also, ion beam thinning may produce surface defects, such as "black dot" defects and high density of dislocations, as discussed in the section 2.5.4. The formation of the surface defects during ion milling is independent of whether or not sample cooling is applied [Cullis *et al.*, 1985; Cullis and Chew, 1988]. Fig. 4.12a is a convergent beam electron diffraction (CBED) pattern of the matrix in the tetrataenite rim showing the oxide spots. Fig. 4.12b is an indexing of diffraction pattern containing $[100]_\gamma$ fcc matrix spots with $L1_0$ superlattice reflections and $[\bar{1}11]_{ox}$ oxide spots.

Fig. 4.13 is a set of TEM images of the tetrataenite rim and the cloudy zone of the Saint Séverin ordinary chondrite. This is the first TEM observation of the microstructure of the tetrataenite rim in an ordinary chondrite. Fig. 4.13a is a BF image. The set of arrows indicates a boundary between the TR and the CZ. Fig. 4.13b is a CDF image from a $(110)_\alpha$ bcc reflection, which shows the bright honeycomb phase in the CZ and precipitates in the TR, implying they have the same crystal structure, bcc. Electron diffraction showed that crystal structure of the TR and the CZ of the Saint Séverin ordinary chondrite are the same as that of the mesosiderites investigated in this study.

4.1.2.2 Chemical Composition of the Tetrataenite Rim

Fig. 4.14a is a TEM bright field image of the tetrataenite rim and the cloudy zone of the RKPA 79015 mesosiderite. Fig. 4.14b shows a Ni composition profile across kamacite and retained taenite in the RKPA 79015 mesosiderite. The data were obtained by X-ray microanalysis using the EM400T AEM. The tetrataenite rim in the RKPA 79015 mesosiderite contains a range of Ni contents from 46.4±0.7 wt.% Ni near the

cloudy zone to 54.1±0.7 wt.% Ni near the kamacite. The Ni content of kamacite at the TR interface was 3.6±0.2 wt.% Ni. The twinning structure found in the tetrataenite rim was also observed in other meteorites, while there was no twins observed in the kamacite. The twin does not stop at the boundary between the tetrataenite rim and the cloudy zone. In addition, there was no change in crystallographic orientation of the tetrataenite rim and the island phase in the cloudy zone. This observation confirms that the ordered structure of the tetrataenite rim and the cloudy zone (the island phase) is a single continuous crystal. The tetrataenite rim shows a fluctuation in Ni composition because it is composed of low Ni precipitates in the high Ni ordered tetrataenite matrix.

Using the VG HB501 STEM which has much better X-ray spatial resolution than the EM 400T, the composition of kamacite was obtained close to the TR interface from 4 analyses in 2 different kamacite regions in the RKPA 79015 mesosiderite. The average composition was 4.0±0.5 wt.% Ni. The Ni composition of the TR at the interface was obtained from 3 analyses in 2 different TR regions in the same mesosiderite. Close to the kamacite interface, the average Ni content was 65.5±3.3 wt.%. Fig. 4.15 is a Ni composition profile across the kamacite/tetrataenite rim interface in the RKPA 79015 mesosiderite obtained with the VG HB501 STEM. It is important to note that the Ni composition at the interface is well over 51.25 wt.% Ni (50.0 at.% Ni) which is a stoichiometric composition of FeNi and much higher than the EM400T result of 54.1 wt % Ni. The VG HB501 STEM has much higher X-ray spatial resolution than the EM 400T. Five data points at the α/γ interface in Fig. 4.15 corresponds to one data point in Fig. 4.14b.

Fig. 4. 16 is a TEM bright field image of the precipitates in the tetrataenite rim region of the Estherville mesosiderite. It is clear that the precipitates contain microtwins. The precipitates showed a range of size from 10 nm to 40 nm. No relationship between the size of the precipitates and the local Ni content of the tetrataenite rim was observed.

However, it was observed that the density of the precipitates decreases as the Ni content in the tetrataenite rim increases, and there was no precipitate in the outermost part of the tetrataenite rim. This observation is consistent with the variation in the density of etch pits in SEM images. For compositional analysis, the through-thickness precipitates were carefully selected so that their Ni contents could be measured without any contribution of X-rays from the matrix. As shown in Fig. 4.16, the size of the precipitates is less than 40 nm in general. Therefore very thin foils were required for successful analysis. The compositional analyses were always conducted on the very edge of the foil. Because the foil was thinnest here, phase overlap along with beam broadening could be minimized. A Ni composition profile across one precipitate in the RKPA 79015 mesosiderite is shown in Fig. 4.17. The Ni composition of the precipitates and matrix was measured from 32 precipitates in the tetrataenite rim using VG HB501 STEM which provided high spatial resolution. The compositions of the precipitate and matrix are 14.2 ± 1.0 wt.% Ni and 52.0 ± 1.0 wt.% Ni, respectively.

The Ni content of the matrix as a function of position within the tetrataenite rim was investigated. The Ni content was measured from 3 different positions where the precipitates were present near by. In the TR region within 1 μm of the CZ interface, 4 measurements were obtained from 4 separate matrix regions. The Ni composition from this region was 50.8 ± 1.5 wt.% Ni. In the TR region about 3 μm away from the CZ interface, 4 measurements were obtained from 4 separate island phase regions. The Ni composition from this region was 51.2 ± 1.7 wt.% Ni. In the TR region about 5 μm away from the CZ interface, 4 measurements again obtained from 4 separate island phases. The result was a Ni content of 51.6 ± 1.0 wt.% Ni. These results indicate that there is no variation in Ni content of the matrix as a function of position within the tetrataenite rim .

4.2 Cloudy Zone

4.2.1 HRSEM Study of the Cloudy Zone

Fig. 4.18 shows two SEM images of the cloudy zone of the RKPA79015 mesosiderite. The cloudy zone is basically composed of two phases; the island phase (I) and the honeycomb phase (H). The honeycomb phase which contains low Ni is preferentially etched away during chemical treatment and appears to be the dark grooves. It is important to note here that not only the tetrataenite rim but also the island phase contains the sub-structure inside; marked with an arrow in a).

Fig. 4.19 is a series of SEM images of a taenite particle in the Saint Séverin (LL6) chondrite showing the size variation of the island phase in the cloudy zone. Fig. 4.19b was taken at the region close to the tetrataenite rim interface, while Fig. 4.19c was taken at the center of the cloudy zone. Considering the "M" shaped Ni concentration in taenite particles in Saint Séverin [Holland-Duffield *et al.*, 1991], the size of the island phase decreases with decreasing Ni content.

In some retained taenite in mesosiderites, the size variation in the cloudy zone was not noticeable. Fig. 4.20a is a SEM image of the Estherville mesosiderite. Fig. 4.20b is a Ni concentration profile obtained by EPMA traversing both kamacite and retained taenite. The Ni concentration profile at the center of the cloudy zone appears to be flat. This is probably due to the fact that the mesosiderite has cooled extremely slow so that Ni has had ample time to diffuse, and that the width of the taenite is narrow so that the Ni diffusion length is relatively short.

4.2.2 AEM Study of the Cloudy Zone

Fig. 4.21 is a set of images of the cloudy zone in the RKPA 79015 mesosiderite to compare the microstructure between SEM and TEM. Fig. 4.21a is a SEM image showing the etch pits (marked with arrows) as well as honeycomb phase (H) and island phase (I). The etch pits and dark grooves were observed in the island phase. Fig. 4.21b is

a TEM bright field image showing precipitates which correspond to the etch pits in Fig. 4.21a as well as the honeycomb phase (H) which appears to be dark, and the island phase (I) which appears to be bright. Note that the precipitates contains microtwins. By electron diffraction, it was observed that the honeycomb phase had a twinning orientation relationship. Note that the contrast discontinuity in the honeycomb phase. This observation confirms that the island phase of the cloudy zone is not only composed of the ordered tetrataenite phase but also contains the precipitates, and explains what the etch pits in the SEM image are.

Fig. 4.22 is a set of TEM bright field and dark field images of the cloudy zone of the Estherville mesosiderite. The BF image (Fig. 4.22a) contains the island phase (I) which is bright, the honeycomb phase (H) which is dark, and the precipitates (P) within the island phase. Note that the precipitates contains microtwins. Fig. 4.22b is a CDF image from a (011) bcc reflection. The honeycomb phases and the precipitates are illuminated simultaneously confirming that the honeycomb phase and the precipitates have the same crystal structure which is body centered cubic (bcc). Fig. 4.22c is a SADP which is essentially the same as Fig. 4.11d. The indexing of the SADP (Fig. 4.22c) is shown in Fig. 4.22d.

Fig. 4.23a is a TEM bright field image of the cloudy zone in the Saint Séverin ordinary chondrite. This is the first TEM observation of the microstructure of the cloudy zone in an ordinary chondrite. The average Ni content of this region was 37.3 ± 1.0 wt.% Ni. Comparing the size of the phases with the HRSEM image (Fig. 4.19), the original size of the metal particle and the Ni content determined by EPMA, the location investigated can be determined. Fig. 4.23a was taken at the middle of the cloudy zone. The CZ region in the taenite particles contains two phases: the island phase which is bright and the honeycomb phase which is dark in the TEM BF image (Fig. 4.23a). The structure of the cloudy zone of Saint Severin is very similar to that of iron meteorites and stony-iron

meteorites. The selected area diffraction (SAD) pattern (Fig. 4.23c), as indexed in Fig. 4.23d, is composed of the fcc [110] zone axis pattern, two bcc [111] zone axis patterns which are in a twinning orientation relationship, and weak superlattice diffraction spots which can be observed on the negative although they are not clear on the print. The superlattice spot is due to the ordering of the parent fcc phase to tetrataenite. The twinning plane is $(002)_{fcc}$. The centered dark field (CDF) image (Fig. 4.23b) taken from a (011) bcc reflection in Fig. 4.23c shows that the honeycomb phase has a bcc structure.

Fig. 4.24a is a TEM BF image of the cloudy zone in the Saint Séverin chondrite. The island phase is labeled I. The honeycomb phase was not observed in this specimen. The region between the island phases, which is supposed to be the honeycomb phase, is filled with oxide layers. It seems that all the honeycomb phases have been etched away during electrochemical polishing. However, this specimen was good enough to examine the island phase. The black features in the island phases is thought to be the "black dots" resulting from ion beam thinning. Fig. 4.24b is a CBED pattern from the island phase showing fcc [110] zone axis pattern, and Fig. 4.24c shows the details of zero order Laue zone (ZOLZ) pattern which contains superlattice diffraction spots, and Fig. 4.24d is an indexing of the ZOLZ pattern. This observation confirms that the island phase in the Saint Séverin chondrite also has the ordered $L1_0$ superstructure.

The Ni content of the phases present in the cloudy zone was measured using the EM400T and the VG HB501. The RKPA 79015 mesosiderite, the most slowly cooled meteorite, was analyzed because the honeycomb phase was sufficiently large so that scattering of the focused electron probe (beam broadening) was not significant, and X-rays are generated solely within the honeycomb phase. Fig. 4.25 is a Ni composition profile across the honeycomb phase and the island phase in the RKPA 79015 mesosiderite obtained with the VG HB501 STEM. The Ni contents of the honeycomb phase and island phase were 9.0 ± 1.0 wt.% Ni. and 51.8 ± 1.7 wt.% Ni. The Ni

concentration of the precipitate within the island phase was measured from 12 different precipitates. Fig. 4.26 shows a Ni concentration profile across the precipitate. The Ni content of the precipitate obtained is 14.7±1.0 wt.% Ni.

The Ni content of the island phase as a function of position within the cloudy zone was investigated. The Ni content was measured from 3 different positions. In the CZ region within 3 μm of the TR interface, 3 measurements were obtained from 3 separate island phase regions. The Ni composition from this region was 51.5±1.3 wt.% Ni. In the CZ region about 15 μm away from the TR interface, 3 measurements were obtained from 3 separate island phase regions. The Ni composition from this region was 52.3±2.1wt.% Ni. In the CZ region halfway between two TR regions, at center of the CZ, 3 measurements again obtained from 3 separate island phases. The result was a Ni content of 51.7±1.7 wt.% Ni. These results indicate that there is no significant variation in Ni content of the island phase as a function of position within the cloudy zone. It is consistent with the observation of Reuter [1986].

4.3 Size Variation of the Island Phase with Cooling Rate

The island phase width was measured using high magnification (>50,000X) HRSEM images taken across the cloudy zone of 26 meteorites. The measurements of the island phase size are shown in Table 4.1 and Table 4.2. Fig. 4.27 shows the size variation of the island phase at the outermost region of the cloudy zone versus the cooling rate of meteorites. The size of the biggest island phase clearly decreases with increasing cooling rate without regard to whether the host is an iron, stony-iron or stony meteorite. The size of the biggest island phase of the meteorites that were investigated in this study varies approximately from 470 nm to 17 nm, while the cooling rate varies from 0.5 K/Myr to 325 K/Myr. Those meteorites which have cooled relatively fast (the IVA irons) have a very fine CZ microstructure, which can not be easily resolved even by employing a

HRSEM. The specimen preparation for the IVA irons was difficult because the cloudy zone was extremely narrow (usually narrower than 0.5μm) due to the fast cooling rate. The metallographic cooling rates of the meteorites that were investigated in this study were taken from previous measurements.

The cooling rate data for the iron meteorites are listed in Table 4.3. Saikumar and Goldstein [1988] have evaluated the methods to determine the cooling rates of iron meteorites considering impingement effects. They examined three iron meteorites which were included in this study, and showed that their measured cooling rates were greater by a factor of 5 compared to older cooling rates. The cooling rate data from the references [Goldstein and Short, 1967; Goldstein, 1969] were therefore multiplied by a factor of 5 for use in Fig. 4.27. Powell [1969] suggested the cooling rate of 0.1 K/Myr for mesosiderites. At this cooling rate, there appear to be two distinct size groups of mesosiderites; the first group with a width of the island phase about 460 nm including Patwar, Barea, Pinnaroo, and Estherville, and the second group with an approximately 390 nm sized island phase including Chinguetti and RKPA79015. These data suggest that the mesosiderites may have varying cooling rates. Also the cooling rates appear to vary in the IIIAB and pallasite group and in the IVA group.

5. DISCUSSION

5.1 Accuracy of the Compositions Determined by AEM

There are several sources of error in the determination of composition as measured by X-ray microanalysis. These errors include the measurement of the composition at two phase interfaces, the accuracy of the Cliff-Lorimer k_{AB}-factor, and the statistical error in accumulated X-ray counts.

Several geometric factors can lead to uncertainty in determining the composition of an element at the interface between two phases. The possible situations are illustrated in Fig.5.1 and Fig 5.2. First, the orientation of the interface must be parallel to the incident electron beam, or X-rays will be generated from both phases (Fig. 5.1a). Second, at the point of analysis, the foil must be a single phase through its entire thickness (Fig. 5.1 b and c). If one phase overlays another, an average composition will be measured instead of the true composition. Third, the specimen should be carefully positioned so that the interface is oriented parallel to the axis of the EDS detector (Fig.5.2). Extreme care has to be used to properly orient the thin foil to minimize this source of uncertainty.

The interface between the kamacite and tetrataenite rim was well defined in most cases. During the analysis, the focused electron beam was carefully positioned as close to the interface as possible, which has been oriented parallel to the incident electron beam and to the axis of the EDS detector, while still remaining entirely within the image of the phase of interest. The lowest and highest Ni content measured was defined as the representative compositions of the kamacite and tetrataenite rim, respectively, at the interface.

In the cloudy zone, island phases and honeycomb phases comprised an interlacing network resulting in overlapping two phases in addition to the interface not being parallel to the electron beam. Away from the edge of the foil, it was readily observed where island phases overlap island phases and where island phases cover part of the honeycomb

phase. With the added problem of beam broadening, little useful compositional information was obtained from each phase in the cloudy zone unless compositional analyses were conducted at the very edge of the foil. Even with careful positioning of the beam in the center of the honeycomb phase on the very edge of the foil, a contribution of Ni X-rays from the island phase was still measured in many cases. The major problem is thought to be the non-parallel interfaces between two phases. Also the island phase contains fine precipitates (<40 nm) inside. Since the nanometer scale precipitates were not readily observed in the STEM, when measuring the composition of the island phase, there was a chance that the electron beam hit a precipitate which was not observed on the screen. Therefore, in this case, the matrix composition measured was probably an average composition of the true matrix composition and some small precipitates which were included in the X-ray interaction volume. For the reasons discussed above, the lowest and highest Ni composition measured were defined as the representative compositions of the honeycomb phase and island phase, respectively.

Obtaining a true composition of the precipitates was the most difficult of all the analyses because the typical width of the precipitates is only about 10 to 40 nm. The EM400T AEM which has a relatively poor spatial resolution (30~50 nm) [Zhang, 1991] was not able to measure the Ni composition of the fine precipitates (<40 nm). All these measurements were performed using the VG HB501 STEM which has a 2 nm spatial resolution [Zhang, 1991]. The compositional analyses were always conducted on the very edge of the foil. Because the foil was thinnest here, phase overlap along with beam broadening could be minimized. Since the size of the precipitates is so small, non-through thickness precipitates and specimen drift were prominent for the analyses even if only the precipitates at the edge of the foil were examined. The typical width of the precipitates was comparable to the typical foil thickness chosen to perform the analyses in the VG STEM.

The beam broadening has to be considered in addition to the electron beam drift within the precipitate of interest. For example, if the beam is positioned on a precipitate containing 15 wt.% Ni (~13 at.% Ni) in a 20 nm thick foil, the beam broadening factor b given by Equation (2-10) will be 2.13 nm assuming a zero diameter probe. For the VG HB501 STEM with a probe diameter of 2 nm, the spatial resolution R given by Equation (2-9) will be 2.52 nm, and R_{max} will be 2.92 nm. These values are well below the foil thickness. According to this calculation, it is safe to define that the Ni content measured is a true composition of the precipitate without contribution from the matrix, so long as the precipitate is through-thickness (which means greater than the foil thickness) and the specimen does not drift. However, the specimen drift occurred during the analysis and had to be corrected.

The specimen drift was corrected manually for both the EM400T AEM and the VG HB501 STEM. During the analysis, X-ray acquisition was stopped at 30 second intervals, and the specimen drift was corrected by looking at the reference feature in the STEM image. The amount of drift was dependent on the specimen. For the chondrite specimen in which epoxy was used to hold the metal particle, large amount of drift (>100 nm / 30 sec.) was observed when using a room temperature specimen holder. In order to minimize the specimen drift, a cold specimen holder (cooling by liquid nitrogen) was used. Using the cold specimen holder, the specimen drift was significantly reduced (<10 nm / 30 sec.). The bulk metal specimens were more stable than the chondrite specimen in terms of the specimen drift. The amount of the drift was usually less than 5 nm / 30 sec. when using a room temperature specimen holder. The lack of accurate specimen drift correction is the major reason why the practically achievable spatial resolution is much lower than the theoretical values. In addition, contamination may absorb X-rays of interest emanating from the specimen and also spreads the beam prior to entering the specimen, thus reducing the spatial resolution of the microanalysis.

The second source of error is the error in the k_{AB}-factor. In order to determine k_{NiFe} for each instrument used in the analysis, at least 10 compositional analyses were obtained from a Fe-7 wt.% Ni and a Fe-28 wt.% Ni alloy whose composition was determined by the EPMA. At least 20,000 counts in the smallest peak were obtained at each analysis. Using the data, the error in the k_{NiFe} for each alloy was determined as follows;

$$\%error = \frac{t_{95}^{n-1} \cdot S_n}{\sqrt{n} \cdot \bar{k}_{NiFe}} \times 100 \qquad (5\text{-}1)$$

where t_{95}^{n-1} is the Student t value for n measurements at 95% confidence level, S_n is the standard deviation of n measurements, and $\bar{k}_{NiFe}$ is the average value of k_{NiFe}. The experimental k_{NiFe} values are 1.22±0.01 for EM400T AEM at 120 kV and 1.12±0.01 for VG HB501 at 100kV with the relative errors of 0.8 % and 1.06 % at the 95% confidence level respectively.

The third and most significant error in the AEM data is due to the poor counting statistics of the X-rays. As discussed in the section 2.5.3, the accuracy of the quantitative data obtained is ultimately limited by the counting statistics of the X-ray collection process, both in terms of experimental determination of the k-factor, and the acquisition of the raw intensity data for each element. Increasing the number of accumulated counts lowers the relative error. Since the area to be analyzed in the foil is extremely thin (10~20 nm) and probe size used is very small (2 nm), the interaction volume at which X-rays of interest are generated is very small. Thus the counting rate (counts per second) is very low even if a high brightness electron source (FEG) which gives more current is used. The lowest counting rate obtained was as low as 50 cps. Therefore, counting time had to be increased in order to obtain statistically meaningful data at given instrumental conditions. Most of the spectra were acquired for 300 seconds. However, increasing the number of

accumulated counts by increasing counting time gave rise to other problems: specimen drift and contamination.

5.2 Kamacite/Tetrataenite Rim Interface

The Ni composition of kamacite was obtained close to the TR interface in the RKPA 79015 and Estherville mesosiderites. The average composition was 3.6±0.2 wt.% Ni at the 95% confidence level.. This composition is lower than the value of 4.0±0.3 wt.% Ni obtained by Reuter [1986]. It has been reported that the Ni content in the α phase is 4.9±0.5 wt.% Ni in an Fe-Ni (P sat.) alloy held at 300°C [Romig and Goldstein, 1980]. Since the Ni solubility in α phase decreases as temperature decreases, the Ni composition in the kamacite corresponds to an equilibrium temperature below 300°C. The slower cooling resulted in a lower equilibration temperature and therefore a lower Ni content in the kamacite.

The Ni composition of the TR at the interface with kamacite was obtained from the RKPA 79015 mesosiderite. Close to the kamacite interface, the average Ni content was 65.5±3.3 wt.%. With the improved spatial resolution of the AEM, this Ni content is the highest reported for the tetrataenite rim region associated with kamacite [Reuter, 1986; Reuter *et al.*, 1988]. It is important to note that the Ni composition at the interface is well over 51.25 wt.% Ni (50.0 at.% Ni) which is the stoichiometric composition of FeNi. With the most recently proposed Fe-Ni phase diagram by Reuter *et al.* [1989b], such a high Ni concentration of the tetrataenite rim can not be explained. This higher Ni content suggests that the outermost region of the tetrataenite rim may be either Ni_2Fe or non-stoichiometric Ni_3Fe rather than FeNi. At the present stage, it seems more likely that the outermost region of the tetrataenite rim is Ni_3Fe because Ni_3Fe has been found in meteorites [Haggerty and McMahon, 1979; McMahon and Haggerty, 1980; Danon *et al.*, 1981; Rubin, 1991; Kellemeyn *et al.*, 1991; Hua, 1994]. In order to identify the crystal

structure, an electron diffraction study was conducted on the outermost region which had a Ni content of 60 wt.% or more. The lattice parameter of awaruite (Ni_3Fe phase found in meteorites), a= 3.56 Å, is very close to that of tetrataenite (FeNi, a=3.58Å) [Danon *et al.*, 1981]. Furthermore, both Ni_3Fe and FeNi are ordered superstructures, thus the electron diffraction patterns contain superlattice reflections. A fundamental question of interest is whether the superlattice reflections are due to Ni_3Fe with the $L1_2$ superlattice, or FeNi with the $L1_0$ superlattice. Unfortunately, if all three variants of the $L1_0$ structure are included in one diffraction pattern, the superlattice reflections that appear will be in the same positions as those arising from the $L1_2$ structure. One method to distinguish between the two structures would be to obtain a CBED pattern from a single ordered domain. In the [001] orientation, all three superlattice reflections, (001), (010), and the (100) will appear if the structure is $L1_2$. Only one of the three will occur if the structure is $L1_0$. The CBED patterns obtained by traversing along the kamacite/tetrataenite rim interface contained all three variants of superlattice reflections indicating that the crystal structure could be Ni_3Fe. However, there is still an uncertainty about the crystal structure because the beam may not be confined within a single ordered domain.

As pointed out above, there is a indirect evidence of the presence of Ni_3Fe as a meteoritic mineral. A natural mineral of Ni_3Fe (awaruite) has been observed in various chondrites: Allende [Haggerty and McMahon, 1979; McMahon and Haggerty, 1980; Rubin, 1991], Ningqiang CK3 [Kellemeyn *et al.*, 1991; Hua, 1994], and Parambu [Danon *et al.*, 1981]. Danon *et al.* [1981] reported no awaruite associated with tetrataenite or kamacite in the Parambu LL chondrite. Recently, however, Rubin [1991] found awaruite associated with tetrataenite in the Allende chondrite. The composition range of awaruite reported from EPMA measurements is 63.7 to 68.2 wt.% Ni, not 75 %Ni [Hua, 1994]. which is consistent with the Ni composition obtained in this study.

5.3 Three Sub-Zones in the Tetrataenite Rim

Three sub-zone structures in the tetrataenite rim were first observed in two ordinary chondrites, Kernouve and Saint Séverin, by Duffield [1989]. It was originally argued that this structure was unique to the non-phosphorus containing metal particles found in the chondrites. In the light optical micrographs of the chondrites and mesosiderites as shown in Figs. 2.13, 4.1, and 4.3, however, one can clearly see the three sub-zone structure within the tetrataenite rim. In general, iron meteorites have a narrow tetrataenite rim, therefore it would be very difficult to observe the sub-zones when examining optically, even if the sub-zones exist. They can be observed by using HRSEM as shown in Fig. 4.7. The metallic phases in iron meteorites and mesosiderites contain phosphorus as well as sulfur [Buchwald, 1975]. This observation suggests that the three sub-zone structure may be a general feature, not unique to chondrites, and may exist in the tetrataenite rim of all kinds of meteorites. In other words, the clear taenite I region is not truly clear, therefore it is better called the tetrataenite rim.

The HRSEM observation revealed that the three sub-zone structure occurred because the tetrataenite rim contained numerous etch pits and highly etched boundaries (Figs. 4.2, 4.3, 4.4 4.6, and 4.7) which gave rise to differences in contrast in LOM images. It was confirmed, by comparing SEM images with TEM images, that the etch pits corresponded to the precipitates as shown in Fig. 4.9. As will be discussed in the next section, the precipitates are a low Ni phase, thus they were preferentially etched away during chemical treatment resulting in etch pits. The precipitates are well dispersed, and the density of precipitate decreases with increasing Ni content in the tetrataenite rim, and the precipitate is absent in the outermost part of the tetrataenite rim. Also, according to the CDF images of a single ordered variant, deep dark grooves in SEM images correspond to antiphase boundaries (APBs) along with precipitates in TEM images. The APB is a boundary between ordered domains. Because the APBs have a higher energy than the

surrounding ordered region they would be attacked preferentially under etch conditions in a similar way a grain boundary is preferentially attacked. Moreover, the presence of precipitates at the APBs make the grooves deeper. The TEM image of an APB consists of alternating black and white fringes running parallel to the intersection of the habit plane with the foil surface [Edington, 1976]. These fringes will appear by imaging the superlattice reflection. Because the extinction distance for FeNi ordered structures is much larger than the typical foil thickness chosen to perform the imaging [Reuter, 1986], one can see only one fringe as shown in Fig. 4.8 and Fig. 4.11. Note that the size of ordered domains changes across the tetrataenite rim. They are large (approximately 500~1000 nm) at the TR/CZ interface, and are small (approximately 200~500 nm) in the middle of the TR (Figs. 4.8, 4.10, and 4.11). This variation is consistent with the SEM observation (Fig. 4.4). However, this size variation of ordered domain observed in this study does not agree with the previous observations by Reuter [1986] and Albertsen et al. [1983]. They observed that the linear dimensions of the ordered domains increased with increasing the average Ni content: small at the TR/CZ interface and large at the TR/kamacite interface in iron meteorites.

In order-disorder transformation [Rudman, 1967; Haasen, 1974; Reynaud, 1982], unlike in precipitation and decomposition process, no large concentration differences arise, which necessitate transport of material over large distance. It is much more a question of atomic exchange between neighboring sites. The preferential occupation by one atomic species can start in a nucleation process resulting in ordered domains. The ordered domains then extend outwards into the disordered region until they meet other growing domains, forming antiphase boundaries. The APB is defined by the boundary between ordered domains. Finally, the metastable domain structure coarsens until an ordered crystal free of APBs is obtained because the APBs contain additional energy. Concurrently with these processes, the degree of order within each domain defined by Eq.

(2-6) is changing with time [Haasen, 1974]. In addition, the domain coarsening is related to the composition and temperature [Poter and Esterling 1981]. Assuming the ordering in the tetrataenite rim occurs at the same temperature (T_c = 320°C, see section 5.6), the region away from the stoichiometric composition (51.2 wt.%) will have a smaller domain size. Therefore, one can expect larger domains in center of the tetrataenite rim where the matrix has a stoichiometric composition and smaller domain size at the TR/CZ interface, which conflicts with the observation in this study. This is quite puzzling, and it is difficult to explain this discrepancy at the present stage.

The color change in the tetrataenite rim seen in the LOM image (Fig. 4.3) can be explained by changes in the density of etch pits as shown in Fig. 4.4. The region close to the TR/CZ boundary (zone 1) has the highest density of etch pits but a less dense network of APBs. This region corresponds to the layer of light gray color in the LOM image. The middle of the TR (zone 2) has a higher density of APBs associated with etch pits while the density of etch pits is lower than that in zone 1. This region corresponds to the layer of dark gray color in the LOM image. Zone 2 appears to be darker than zone 1, although zone 2 has less precipitates than zone 1. This observation is most likely because zone 2 has a denser network of APBs associated with precipitates, which has been more heavily attacked by the chemical etch than the precipitates themselves. The outer region of the TR has no etch pits and corresponds to the bright white color in the LOM image.

The possible presence of a second phase in the tetrataenite rim has been reported by Albertsen and coworkers [1983]. In examining the iron meteorites, Cape York and Dayton, using TEM, they have observed etch pits in the clear taenite I region and the cloudy zone. They concluded that the second phase was a low Ni fcc taenite because the low Ni phases could be easily etched away resulting in the etch pits, and no bcc phase was detected by Mössbauer spectroscope. However, the only evidence presented by

Albertsen and coworkers for the presence of a low Ni fcc phase was its absence. No positive evidence for its existence was presented in the BF images or in the diffraction patterns. In addition, It was found that the Mössbauer spectroscopy was not sensitive enough to detect the small amount of phase [Reuter, 1986].

5.3.1 Precipitates in the Tetrataenite Rim

The compositional analyses were always conducted on the very edge of the foil. Because the foil was thinnest there, phase overlap along with beam broadening could be minimized. For the analysis, the through-thickness precipitates were carefully selected by comparing the size of precipitates with the foil thickness so that their Ni contents could be measured without contribution of X-rays from the matrix. One can assume that the precipitate is through-thickness if the size of the precipitate is bigger than the thickness of foil. The foil thickness was measured by the log ratio method [Malis *et al.*, 1988] using electron energy loss spectroscopy (EELS). The typical thickness of foil chosen for the analysis was 10 ~ 20 nm. The Ni composition of the precipitates was measured from 32 precipitates in the tetrataenite rim using the VG HB501 STEM. The Ni content of the precipitate is 14.2 ± 1.0 wt.% Ni. This Ni content is significantly higher than that of α kamacite (3.6 ± 0.2 wt.% Ni) which is the equilibrium phase. This difference implies that the precipitate is a metastable phase possibly either α_2 or supersaturated γ.

By electron diffraction from the meteorites investigated in this study, the crystal structure of the precipitates was identified as body centered cubic (bcc). From the diffraction patterns, it can not be discerned whether the structure is kamacite, a=2.864 Å [Pear, 1958] or martensite, a=2.875 Å [Breedis and Wayman, 1962] because the lattice parameters are so similar. However, the fact that the Ni composition is about 14 wt.% implies that the structure is martensitic. The identity of precipitates will be discussed in sections 5.4.2 through 5.5.

5.3.2 Composition Profile in the Tetrataenite Rim

Fig. 4.14 shows a Ni composition profile across kamacite and retained taenite in the RKPA 79015 mesosiderite. The data were obtained by X-ray microanalysis using the EM400T AEM. The tetrataenite rim in the RKPA 79015 mesosiderite contains a range of Ni contents from 46.4±0.7 wt.% Ni near the cloudy zone to 54.1±0.7 wt.% Ni near kamacite. Since the tetrataenite rim is composed of numerous fine precipitates which have low Ni, in the high Ni matrix, it shows a fluctuation in Ni composition. Also because the spatial resolution of the EM400T AEM is 30~50 nm, the matrix composition measured was probably an average composition of the true matrix composition and some small precipitates which were included in the X-ray interaction volume. This average composition can be defined as a local Ni composition before the precipitation process.

Taking advantage of the high spatial resolution of the VG HB501 STEM, the compositions of the matrix at the kamacite interface and around the precipitates could be determined more accurately. Close to the kamacite interface, the average Ni content was 65.5±3.3 wt.%. The Ni composition of the matrix as a function of position was investigated in this study. Within the precision of the analysis, no variation in the Ni content of the matrix where the precipitates exist near by (in zone 1 and 2) was observed. The average Ni content was 51.2±1.4 wt.% Ni. Combining compositional results and the electron microscopy results, the possible Ni concentration profile can be schematically illustrated as shown in Fig. 5.3. Assuming that the Ni composition of the precipitate does not change through the tetrataenite rim, the Ni decrease through the TR must be due to an increase in the volume fraction of the precipitate. This is consistent with the SEM and TEM results.

5.4 Cloudy Zone Structure

It has been known that the cloudy zone was composed of island phases which had high Ni and honeycomb phases which had low Ni [Scott, 1973; Lin *et al.*, 1977]. The mechanism responsible for the formation of the cloudy zone is believed to be spinodal decomposition. Jago *et al.* [1982] suggested that the CZ in the Santa Catherina meteorite formed through spinodal decomposition of the γ to ordered γ' and low Ni γ. With further cooling the transformation continued to produce γ' and low Ni α. Guimarães *et al.* [1980] suggested the possibility of a spinodal decomposition in the Fe-Ni system based on data from the literature on Invar behavior and on iron meteorites. Albertsen *et al.* [1983] and Reuter *et al.* [1988] suggested that the CZ formed through a spinodal decomposition mechanism that was magnetically induced. [Reuter *et al.*, 1989b]. The mechanism of the CZ formation will be discussed in section 5.6.2.

5.4.1 Island Phase

In this study, it was observed that the island phase was not a single phase but a two phase mixture which was composed of low Ni fine precipitates in the high Ni matrix. In agreement with previous investigations [Albertsen *et al.*, 1980; Novotny *et al.*, 1982; Christiansen *et al.*, 1984; Reuter *et al.*, 1984], the structure of the matrix of the island phase was confirmed as ordered $L1_0$ by electron diffraction. The composition of the island phases in RKPA 79015 was measured as a function of position within the cloudy zone. No compositional variation with position was observed, within the precision of the analysis, and an average Ni composition of 51.8 ± 1.7 wt.% Ni resulted. This value overlaps the Ni content range of 50.9 ± 1.4 wt.% Ni measured by Reuter *et al.* [1988, 1989b]. The result of this study is consistent with that of Reuter *et al.* [1088, 1989b]. The cloudy zone shows a fluctuation in Ni composition as shown in Fig. 4.14. This fluctuation is due to the fact that the cloudy zone is composed of a low Ni honeycomb

phase and precipitate, and a high Ni island phase. Also, an improved X-ray spatial resolution is responsible for this compositional fluctuation. The composition profile obtained with the EPMA shows a smooth decrease in Ni content in the cloudy zone as shown in Fig. 4.5, since the EPMA measures the Ni content on a micron scale.

5.4.2 Honeycomb Phase

The honeycomb phase has been identified by different research groups as α [Scott, 1973], α_2 [Novotny, 1982; Reuter *et al.*, 1984, 1988,1989b] and γ [Albertsen *et al.*, 1980, 1983; Christiansen *et al.*, 1984]. In this study, the RKPA 79015 mesosiderite, one of the most slowly cooled meteorites, was analyzed because the honeycomb phase was sufficiently large in this meteorite so that scattering of the focused electron probe (beam broadening) was not significant, and X-rays are generated solely within the honeycomb phase. The Ni content of the honeycomb phase obtained in this study is 9.0 ± 1.0 wt.% Ni. This Ni content is significantly higher than that of the equilibrium α phase (3.6 ± 0.2 wt.% Ni) implying that the honeycomb phase is a metastable phase possibly either α_2 or supersaturated γ. By electron diffraction, however, a bcc structure was observed. In addition, it was observed that the honeycomb phase had a twinning orientation relationship (Figs. 4.21 and 4.23). In the Fe-Ni lath martensite, the martensite packet consists of blocks of parallel laths separated by high-angle boundaries which may be twin-related [Marder and Marder, 1969; Krauss and Marder, 1971]. The fine structure of the honeycomb phase is filled with dislocations and has a lath-like appearance, as observed by Novotony [1982]. In order to confirm that the honeycomb phase is martensite, the possible effect of sample preparation on the martensitic transformation should be considered. Recently, there was a controversy developed over the identity of the honeycomb between Reuter et al. [1984, 1988,1989b] and Albertsen *et al.* [1980, 1981, 1983], considering sample preparation procedure.

Based on Mössbauer data, the honeycomb phase was identified as a paramagnetic fcc γ phase, containing less than 25 wt.% Ni as analyzed by Albertsen *et al.* [1980, 1983] and Christiansen *et al.* [1984]. The Mössbauer spectra are actually composed of two overlapping spectra: one with six lines corresponding to ordered FeNi with $L1_0$ superstructure, and the other with a single line which is located at the center corresponding to a paramagnetic phase containing less than 25 wt.% Ni. No evidence was found for ferromagnetic martensite or kamacite. Reuter et al. [1988] argued that this paramagnetic phase is most likely CT-2 (25 to 28 wt.% Ni) and the sample preparation technique (acid-etching process) used by Albertsen *et al.* [1980, 1983] is the cause of the discrepancy. The long acid-etching process to separate the taenite regions from the surrounding kamacite could etch away any bcc phases within the taenite region resulting in the lack of evidence for martensite as a part of the CZ. Reuter et al. [1988] also found that, even if α_2 were present in the CZ, the Mössbauer spectroscopy was not sensitive enough to detect the small amount.

According to Warlimont [1961] and Klostermann and Burgers [1964], by making a sample electron transparent, the γ (Fe-Ni) may transform to α_2 due to thin-foil effects which increases M_s (the temperature at which the transformation of austenite to martensite starts during cooling). They suggested that the activation energy for α_2 nucleation is reduced (increasing the M_s temperature) because the strain energy term in calculations of the critical embryo size is reduced when the embryo size and the specimen thickness have the same order of magnitude. Reuter et al. [1988] investigated the CZ of Estherville in both the thick and the thin areas using the high voltage electron microscope (HVEM) to see if α_2 is only seen in the thin areas due to thin-foil effects [Gaggero and Hull, 1962]. Using 1MeV electrons which can penetrate up to 2 μm of stainless steel [Thomas and Lacaze, 1973], Reuter et al. [1988] observed bcc reflections in selected area diffraction patterns from both the thin and the thick areas. Reuter et al. [1988] also

pointed out that, in all of the studies on the increase in M_s temperature due to decreasing foil thickness [Warlimont, 1961; Klostermann and Burgers, 1964], the alloys studied contained about 30 wt.% Ni for which the M_s is about room temperature. The thin foil effect may increase M_s from below room temperature to above room temperature. Since the M_s temperature for 12 wt.% Ni which was the Ni content of the honeycomb phase obtained by Reuter et al. [1988] was ~430°C, and the TEM sample was prepared at or below room temperature, the suggestion that α_2 is a product of an increased M_s due to thin-foil effects was also shown to be false.

Another argument against martensite forming in the honeycomb phase is the slow cooling rate that meteorites experienced. It is well known that the martensitic transformation in a Fe-Ni alloy is a diffusionless athermal process [Porter and Easterling, 1981; Nishiyama, 1978]. Martensite is thus able to grow independently of thermal activation. In the athermal transformation, the amount of martensite is governed solely by the temperature, and the position of the M_s temperature is independent of the cooling rate while the critical range is dependent on the cooling rate [Mirzayev et al., 1979a, 1979b; Kamenetskaya et al., 1983; Wilson, 1984; Thadhani and Meyers, 1986; Jicheng and Zhanpeng, 1990]. The critical cooling rate range for the martensitic transformation in the literature is well above the cooling rate range of meteorites implying that the martensitic transformation is unlikely to occur.

However, α_2 is observed by LOM and SEM in the center of the retained taenite of many meteorites [Buchwald, 1975; Lin et al., 1977]. Therefore, the martensitic transformation occurs despite the slow cooling process that these meteorites experienced. Consequently, from the evidence discussed above, it is concluded that the honeycomb phase is martensite containing 9.0 ± 1.0 wt.% Ni.

5.4.3 Precipitates in the Island Phase

The compositional analyses were always conducted on the very edge of the foil in the same manner used for the precipitate in the TR. The Ni content of the precipitate measured by the VG HB501 STEM is 14.7±1.0 wt.% Ni. This is essentially the same as the Ni content of the precipitates found in the TR (14.2±1.0 wt.% Ni). By electron diffraction, the crystal structure of precipitates was identified as body centered cubic (bcc). In dark-field images (Figs. 4.11b, 4.13b and 4.22b), the honeycomb phases and the precipitates are illuminated simultaneously confirming that the honeycomb phase and the precipitates have the same crystal structure. However, it was observed that the Ni content of the precipitates is higher than that of the honeycomb phase (9.0±1.0 wt.% Ni). As will be discussed in following section, the martensitic transformation in small particles is easily suppressed (lower M_s). Therefore, one can expect even lower Ni content in the small precipitates. However, it is expected that the Ni content of the precipitates is the same as that of the honeycomb phase because below 200°C Ni diffusion is essentially stopped (see section 5.6 for further discussion). This discrepancy may be due to the beam broadening, small size of the precipitates (<40 nm) and the specimen drift. It was assumed that the precipitate is through-thickness if the size of the precipitate is bigger than the foil-thickness. Even if care was taken to select the through-thickness precipitates, the possibility that the Ni content of precipitates could be measured with some contribution of X-rays being generated from the high Ni matrix can not be completely ruled out. Two possible examples are shown in Fig. 5.1c and Fig. 5.2. In both cases, the measured Ni content will be higher than the true composition of the precipitates due to the contribution of the high Ni matrix. Another contribution to the high Ni content of the precipitates is the specimen drift. Even if the electron probe was positioned so X-rays were only being generated from the precipitate, any specimen drift during analysis would result in Ni X-rays also being generated from the matrix. Therefore,

it seems most likely that the precipitates and the honeycomb phase have the same structure (martensite) with the same Ni content. The martensitic transformation occurred in these small precipitates (<40 nm) is discussed in next section.

5.5 Martensitic Transformation in small precipitates

The precipitates in the tetrataenite rim and the island phase contains low Ni (~14 wt.% Ni). The Ni content of the precipitates is possibly even lower than 14 wt. % as discussed above (9 wt.%). However, it was observed that the precipitates showed a characteristic morphology of the plate martensite which often occurred in the high Ni Fe-Ni alloys. As seen in Figs. 4.10, 4.16, 4.21 and 4.22, the precipitates contains microtwins. It is well known that there is a transition of lath martensite to plate martensite at about 29 at.% Ni (below which plate martensite is suppressed by lath martensite) [Patterson and Wayman, 1966; Krauss and Marder, 1971; Porter and Easterling, 1981]. In other words, martensite formed at higher temperatures (lower Ni and higher M_s) grows by a slip mechanism resulting in lath martensite, while martensite formed at lower temperatures (higher Ni and lower M_s) grows by a twinning mode resulting in plate martensite. In order to answer the question: how do the precipitates with a low Ni have a characteristic morphology of plate martensite?, the martensitic transformation in small particles is considered.

Cheh and Turnbull [1956] investigated martensitic transformation in Fe-Ni particles of 30~100 μm and observed that M_s decreased remarkably with decreasing particle size. This result was interpreted as due to the lack of favorable nucleation sites. A similar conclusion was drawn by Kachi et al. [1962]. Easterling and Swann [1971] also observed that the martensitic transformation was suppressed by reducing particle size. They examined the Fe-Ni particles over a size range of 2~200 nm, and observed that the particles of low Ni transformed to martensite. Recently, Kajiwara et al. [1987, 1991] and

Zhou et al. [1990, 1991] suggested that the decreasing M_s in small particles was due to the fact that the accommodation of plastic deformation in austenite became difficult in the fine particles owing to the lack of lattice dislocations, not due to the lack of favorable nucleating sites.

There are two possible explanations for the morphology found in the precipitates. First, a decrease in size of the precipitates (10~40 nm) effectively lower the M_s, and make possible the transition to the plate morphology. The twinning becomes easier to occur compared to the slip deformation with decreasing M_s [Krauss and Marder 1971]. Consequently, upon cooling, plate martensite with twins forms in the precipitates. However, it is not known whether the precipitates are completely transformed to plate martensite or are a mixture of lath martensite and plate martensite. In addition, the possibility that some of precipitates are only partially transformed to martensite can not be ruled out (Fig. 4.10). It was difficult to observe the internal structure of the small precipitates (< 40 nm). Second, prior to the martensitic transformation, the twinning occurs presumably in order to accommodate better the local transformation stresses resulting from tetragonality of ordered matrix. And then the twinned precipitates transformed to lath martensite with twin.

Kajiwara et al. [1991] investigated ultrafine particles of size ranging from 20 to 200 nm prepared by a hydrogen plasma reaction method, which contain 12 ~ 35 at.% Ni, and found that the martensitic transformation was unlikely to occur below room temperature. A similar result was obtained by Zhou et al. [1990, 1991]. These observations imply that the plate martensite forms above room temperature, if the first hypothesis is correct. However, the plate martensite is unlikely to occur above room temperature in Fe-Ni alloys [Krauss and Marder, 1971]. Therefore, it seems most likely the second hypothesis is more favorable to occur.

5.6 Low Temperature Fe-Ni Phase Diagram

The AEM data from RKPA 79015 are used to define the Fe-Ni phase diagram at 200°C. At 200°C, Ni diffusion has essentially stopped because the Ni diffusion coefficient is very small at this temperature ($\sim 10^{-32}$), more than 10^9 years are needed for one atomic jump at 200°C, which is comparable to the age of the solar system (4 Gyr)[Wasson, 1985]. The more slowly a meteorite is cooled, the lower its equilibration temperature. Because RKPA 79015 is one of the most slowly cooled meteorites, mesosiderites, the lowest possible equilibration temperature is assumed. Even with its extremely long cooling history, however, true thermodynamic equilibrium has not been attained in the taenite region. Hence, the low temperature transformations occurring in the retained taenite are metastable. The lack of equilibrium is manifested in the Ni composition profiles of the taenite regions as shown in Figs. 4.5, 4.14, and 4.15.

The chemical and structural data obtained in this study can be used to generate the stable and metastable phase boundaries below ~400°C on the Fe-Ni phase diagram. Fig. 5.4 is the modified Fe-Ni phase diagram proposed in this study. The structure and Ni content of each region in the meteorite are summarized in Table 5.1. The easiest way to consider the possible configurations of the various phase fields observed in this study is to start by examining the most recent Fe-Ni phase diagrams which are the theoretical diagram proposed by Chuang *et al.* [1986b] (Fig. 2.9) and its modified diagram proposed by Reuter *et al.* [1989b] (Fig. 2.10), and see how these phase diagrams can be modified to account for the data obtained in this study. The symbols used on the phase diagram and in the following discussions are defined as follows: α is a low Ni bcc phase kamacite, γ is a high Ni fcc phase taenite, γ_1 is a low Ni paramagnetic fcc phase, γ_2 is a high Ni ferromagnetic fcc phase, γ' is ordered Ni_3Fe, γ'' is ordered FeNi, and α_2 is martensite. These symbols are consistent with the previous literature [Chuang *et al.* 1986b; Reuter *et al.* 1989b].

The $\alpha/(\alpha+\gamma)$ and $(\alpha+\gamma)/\gamma$ phase boundaries in Chuang *et al.*'s diagram and Reuter *et al.*'s diagram agree reasonable well with previous data based on measurements of Fe-Ni alloys by Romig and Goidstein [1980]. Data obtained by Romig and Goldstein [1980] are shown as open squares in Fig. 5.4. These boundaries are left essentially unchanged in the modified phase diagram (Fig. 5.4). As discussed in the section 2-2, Chuang *et al.* [1986a, 1986b] constructed the Fe-Ni phase diagram by using thermodynamic calculations taking account into the magnetic effect on the Gibbs free energy. Based on thermodynamic calculation, a tricritical point was introduced at 462°C and 48.8 wt.% Ni associated with a miscibility gap resulting in the formation of a monotectoid equilibrium at 389°C as given below:

$$\gamma_1 \text{ (41.2 wt.\% Ni)} \Leftrightarrow \alpha \text{ (6.6 wt.\%Ni)} + \gamma_2 \text{(47.5wt.\%Ni)}$$

The tricritical point was based on the rapid change in Curie temperature (T_c) with Ni content and the resultant magnetic contributions to the Gibbs free energy of the fcc γ phase [Lin and Chang, 1988]. Below the tricritical point, the fcc γ phase splits into the low Ni γ_1 paramagnetic and the high Ni ferromagnetic γ_2 phases. The tricritical point was also accepted by Reuter *et al.* [1989b] in constructing the Fe-Ni phase diagram as shown in Fig. 2.10. Since no data on the γ_2 phase field were obtained in this study, the tricritical point is left essentially unchanged in the modified phase diagram (point t in Fig. 5.5). Recently, Zhang *et al.* [1994] studied the decomposition of Fe-Ni martensite by aging martensitic Fe-Ni alloys at temperatures between 300°C and 450°C. Their results are shown as open triangles in Fig. 5.4. By means of X-ray analyses, they proposed the monotectoid reaction in the temperature range between 400°C and 450°C. Because no data points are available between 400°C and 450°C in the paper [Zhang *et al.*, 1994], 400°C has been accepted as the temperature of the monotectoid reaction in the new phase diagram (Fig. 5.4). According to Zhang *et al.* [1994], at 400°C, the solubility limits of Ni

in α and γ are ~10 wt.% Ni with the error of ±3wt.% Ni and ~50wt.% Ni with the error of ±3wt.% Ni, respectively. The solubility limits of Ni in α is higher than the values given by Romig and Goldstein [1980], and Chuang *et al.* [1986b]. This discrepancy is possibly due to the fact that the growth of γ precipitates is governed by partial interface control as suggested by Zhang *et al.* [1994]. Thus the Ni content for the matrix phase (α) is higher than the equilibrium value. In addition, the solubility limit of Ni in γ calculated by Chuang *et al.* [1986b] fits within the error range given by Zhang *et al.* [1994]. Therefore, the solubility limits of Ni in α and γ calculated by Chuang *et al.* [1986b] are accepted in the new phase diagram.

Below the temperature at which the monotectoid reaction occurs, the miscibility gap ($\gamma_1+\gamma_2$) is continued and is shown as dashed lines representing the metastable phase boundaries. Spinodal boundaries were also calculated by Chuang *et al.*, and are shown as lines with cross hatching in Fig. 2.9. Evidence supporting the existence of a miscibility gap in the Fe-Ni and similar systems can be found in the literature as follows. Direct evidence for a miscibility gap has been observed for the Fe-Pd system [Raub et al., 1963]. Because thermodynamic and physical properties of the Fe-Pd system are similar to the Fe-Ni system [Kubaschewski et al., 1977; Kubaschewski, 1982], the presence of a miscibility gap in the Fe-Pd system suggests that a miscibility gap may also exist in the Fe-Ni system. Kubaschewski et al. [1977] also suggested a miscibility gap in the Fe-Ni system using thermodynamic measurements. Chamberod *et al.* [1978, 1979] observed phase separation in the 30~50wt.% Ni range during irradiation. They reported that γ separated into two phases, one rich in Ni and the other poor in Ni. The possibility of this two phase separation was also used to explain the anomalous behavior observed in the Invar alloys [Schlosser, 1971; Morita *et al.*, 1984].

The cloudy zone structure in meteorites is formed by a spinodal decomposition process [Jago *et al.*, 1982; Guimarães *et al.*, 1980; Albertsen *et al.*, 1983; Reuter *et al.*,

1988, 1989b]. Therefore, Reuter *et al.* modified the low temperature portion of miscibility gap and spinodal boundaries of Chuang *et al.*'s diagram based on the AEM results obtained from meteorites. Since the honeycomb phase and the island phase are the product of a spinodal decomposition, the Ni content of the honeycomb phase and the island phase defines the low Ni and high Ni boundaries of the miscibility gap, respectively. Also spinodal boundaries can be defined by the low Ni end and high Ni end of the cloudy zone. With the improved X-ray spatial resolution, these boundaries can be re-defined using the AEM results obtained in this study as shown in Fig. 5.4. The high Ni boundary of the miscibility gap defined by the Ni content of the island phase is 51.8 wt.% Ni (Table 5.1), which is consistent with the observation of Reuter *et al.* considering statistical error in X-ray microanalysis. The low Ni boundary of the miscibility gap defined by the Ni content of the honeycomb phase is 9.0 wt.% Ni (Table 5.1), which is lower than 11.7 wt. % observed by Reuter *et al.* [1989b]. This discrepancy is due to the fact that the X-ray spatial resolution of the VG HB501 used in this study is much better than that of the EM400T used by Reuter *et al.* [1989b].

The high Ni spinodal boundary is defined by the Ni content at the TR/CZ interface. In this study, the high Ni spinodal boundary is 46.4 wt.% Ni which is consistent with the observation of Reuter *et al.* [1989b]. Since, the meteorites investigated in this study contain only tetrataenite rim and cloudy zone, the low Ni spinodal boundary, 28 wt.% Ni, determined by Reuter *et al.* [1989b] at the CT2/CZ boundary for iron meteorites is used in the new phase diagram (Fig. 5.4). In addition, the low Ni spinodal boundary at temperatures higher than 200°C has been determined by Reuter *et al.* [1989a, 1989b] using an electron irradiation experiment (shown as filled squares in Fig. 5.4). This boundary is also accepted in the new phase diagram (Fig. 5.4).

A major discrepancy between Chuang *et al.*'s phase diagram (Fig. 2.9) and Reuter *et al.*'s phase diagram (Fig. 2.10) is the presence of the FeNi field as an equilibrium phase.

In Chuang *et al.*'s phase diagram, there is no γ'' (FeNi) single phase field, but, at ~50 wt.% Ni, a $\alpha+\gamma'$ (Ni_3Fe) two phase field is predicted. However, the results of many investigations [Clarke and Scott, 1980; Peterson *et al.*, 1977; Reuter *et al.*, 1988], including studies using irradiation to enhance the diffusion rates [Chamberod *et al.*, 1979; Reuter *et al.*, 1989a], show that the γ'' ($L1_0$ ordered FeNi) phase exists. Therefore the FeNi phase field was included in Reuter *et al.*'s phase diagram as an equilibrium phase. However, the high Ni content at the kamacite/tetrataenite interface observed in this study can not be explained with the Reuter *et al.*'s phase diagram. Thus the γ' (Ni_3Fe) and γ'' (FeNi) phase fields are modified as shown in Fig. 5.4 using the AEM results obtained in this study (Table 5.1) and the phase diagram calculations of Chuang *et al.* [1986b]. Chuang *et al.* predicted a eutectoid reaction at 345°C for the Fe-Ni alloy system as given below:

$$\gamma_2\ (50.5\ \text{wt.\% Ni}) \Leftrightarrow \alpha\ (6.2\ \text{wt.\%Ni}) + \gamma'\ (63.7\text{wt.\%Ni})$$

Heumann and Kartesen [1963] also suggested a eutectoid reaction at 345°C with a eutectoid composition of 53.2 wt.% Ni based on X-ray analysis and electron microscopy. The eutectoid composition of 53.2 wt.% Ni given by Heumann and Kartesen [1963] is 2.7 wt.% higher than the value calculated by Chuang *et al.* [1986b]. In order to obtain alloys that are in equilibrium at a given temperature, Heumann and Kartesen [1963] applied two different methods: for the range 230~360°C, they used the decomposition of Ni- and Fe-carbonyls, and for alloys above 370°C, they used the transpiration method. The eutectoid composition suggested by Heumann and Kartesen [1963] agrees with measurement by Zhang *et al.* [1994] and is accepted in the new phase diagram (Fig.5.3).

In the phase diagram proposed in this study, α and γ' (Ni_3Fe) phases are in equilibrium at low temperatures, while γ'' (FeNi) phase is present as a metastable phase shown as a dotted line in Fig. 5.4. Van Deen and Van der Woude [1980, 1981] determined

the Fe-Ni phase diagram in the γ' (Ni_3Fe) phase region using Mössbauer spectroscopy. They measured the critical ordering temperature of γ' (Ni_3Fe) which reached a maximum at 74wt.% Ni and 516°C. The low temperature portion of the $(\alpha+\gamma')/\gamma'$ boundary is determined by the Ni content of tetrataenite rim at the TR/kamacite interface, which is 65.5 wt.% Ni in this study. Meanwhile, the γ'' (FeNi) phase is present as a metastable line compound of which the critical ordering temperature is 320°C at 52 wt.% Ni as shown in Fig. 5.4. This ordering temperature was first determined by Paulevé *et al.* [1962] using neutron irradiation and electrical resistivity measurements of Fe-Ni alloys and recently confirmed by Reuter *et al.* [1989a] using 1MeV electron irradiation. The composition of the γ'' (FeNi) phase is coincident with the dashed line which defines the high Ni side of the miscibility gap.

5.7 Mechanisms of Taenite Decomposition

The proposed phase diagram in Fig. 5.4 and Fig. 5.5 can now be used to understand the decomposition of taenite and the transformations for Fe-Ni alloys cooled below 400°C. The observed microstructure in the meteorites is interpreted in terms of the new Fe-Ni phase diagram. In order to discuss the mechanisms for taenite decomposition, the bulk Ni content of the RKPA 79015 mesosiderite (9.87 wt.% Ni) is considered [Clarke and Mason, 1982], and the vertical line (a-b) is drawn through this composition in Fig. 5.5. The upper segment of this line between points a and d is drawn as a solid line, while the lower segment between points d and b is shown as a dashed line. The solid portion falls into a single γ phase region. The dashed segment d-b lies in two phase regions ($\alpha+\gamma$, $\alpha+\gamma_2$, $\alpha+\gamma'$). As meteorites cooled below 900°C (a $\rightarrow$ b), the line a-b intersects the $(\alpha+\gamma)/\gamma$ solvus line and the equilibrium transformation $\gamma \rightarrow \alpha + \gamma$ occurred resulting in the Widmanstätten pattern. That is, at ~700°C, the kamacite with the Ni content of c nucleates form the taenite with the Ni content of d. Upon cooling to 400°C,

the Ni content of γ phase increases along the $(\alpha+\gamma)/\gamma$ solvus line (d $\rightarrow$ f), and will be the highest Ni content at the kamacite interface of 41 wt.% Ni which is the Ni content of the monotectoid point (f). The Ni content of α phase changes along the $\alpha/(\alpha+\gamma)$ solvus line (c $\rightarrow$ e). A schematic Ni concentration profile just above the monotectoid temperature, T_1 (~400°C), is shown in Fig. 5.6 along with the phase diagram. The Ni composition profiles in Fig. 5.6 are only a part drawn with a high Ni M-profile development which is symmetric. The Ni content of the center of the M-profile could be lower if bulk Ni concentration is low and the cooling rate is fast.

5.7.1 Tetrataenite Rim

According to the new phase diagram (Fig. 5.5), at 400°C, the monotectoid reaction, $\gamma_1 \rightarrow \alpha + \gamma_2$, occurs. Therefore, the γ_1 phase with 41 wt.% Ni (point f) transforms to the γ_2 phase containing 48 wt.% Ni (point g) and α phase containing 7 wt.% Ni (point e). There will be no γ containing from 48 wt.% Ni to 41wt.% Ni to transform at lower temperatures. This is consistent with the EPMA result (Fig. 4.5) which has a discontinuity from 47 wt.% Ni to 42 wt.% Ni. This discontinuity in Ni composition profile has been observed by Reuter et al. [1989b], Scott [1973] and Scott and Clarke [1979]. The step in the composition profile can be interpreted as evidence for the monotectoid transformation. Since the EPMA measures the Ni content on a micron scale, the results from EPMA represent the composition of the higher temperature transformation products. After the monotectoid reaction occurred, the Ni content of the kamacite and taenite at the kamacite/taenite interface follows the solvus lines e-h and g-i, respectively, until the eutectoid temperature (345°C) is reached. The Ni concentration profile below the monotectoid temperature, T_2 (~380°C), is shown in Fig. 5.6 along with the phase diagram. Below 400°C, Ni diffusion is no longer able to keep up, equilibrium is no longer maintained. Thus, as will be discussed, the taenite remains as supersaturated

solid solution. No spinodal reaction occurs until the meteorite cools down to ~320°C because there is no γ containing from 48 wt.% Ni to 41wt.% Ni, which falls within the spinodal region (hatched region). At about 345°C, the high Ni γ_2 phase undergoes an eutectoid reaction, $\gamma_2 \rightarrow \alpha + \gamma'$, and transforms to α phase containing about 6 wt.% Ni (point h) and γ' phase containing about 64 wt.% Ni (point j) at the kamacite interface. The retained taenite behind the kamacite/taenite interface still remains as supersaturated solid solution because of the kinetics. As predicted in the monotectoid reaction, there will be no γ containing Ni contents from 53 wt.% to 63 wt.% Ni. Therefore one may expect another discontinuity in the composition profile. However, it is difficult to observe such a discontinuity because it occurs within a narrow spatial region (~ 100 nm) at the very edge of the tetrataenite rim. The Ni concentration profile below the eutectoid temperature, T_3 (~340°C), is shown in Fig. 5.6.

The region containing the range of Ni content from 46 wt.% (high Ni spinodal boundary) to 63 wt. % (at the kamacite interface) corresponds to the tetrataenite rim. The region ranging from 46 wt.% Ni up to 52 wt.% Ni is located within the miscibility gap, outside the spinodal boundary. According to the classical theory of spinodal decomposition, as discussed in section 2.1.2, alloys outside the spinodal but within the miscibility gap can transform only by nucleation and growth mechanism. This transformation requires overcoming an activation energy barrier and therefore, is more difficult to accomplish than spinodal decomposition. Therefore, the 46 ~ 52 wt.% Ni region remains initially as supersaturated solid solution. When this region cools below 320°C, ordering of FeNi occurs because it requires only local atomic motion, not nucleation. The ordered domains then coarsen as the meteorite cools to 200°C, after which no further diffusion occurs. As cooling continues, the undercooling (ΔT) increases. Thus the driving force for the precipitation becomes large enough for precipitation to occur. Once a critical undercooling (ΔT_c) is reached this supersaturated solid solution

transforms to the ordered matrix with a Ni content defined by the high Ni miscibility gap and the precipitates with a Ni content defined by low Ni miscibility gap. As shown in Fig. 2.2, the driving force (ΔG_n) can be related to the ΔX, and it explains why the density of the precipitate decreases with increasing Ni content in the TR region. The schematic Ni concentration profile at 200°C is shown in Fig. 5.7 along with the phase diagram. The dashed line represents the average Ni composition.

There is time for the nucleated precipitates in TR to grow to their observed size. Using the equation for the Ni diffusion coefficients at different temperatures determined by Dean and Goldstein [1986], this precipitation can be justified. Dean and Goldstein [1986] determined the diffusion coefficients of Ni in α and γ for the binary Fe-Ni and the ternary Fe-Ni-P systems at temperatures below 900°C. The expression for the binary diffusion coefficient is given by:

$$D_{binary} = \exp(-1.89 + 0.00519 \times C_{Ni}) \times \exp\{-(69845 - 11.6 \times C_{Ni}) / RT\} \qquad (5\text{-}2)$$

where C_{Ni} is the Ni content in at.%, R is the gas constant and T is the temperature in K. In ternary system, the ternary diffusion coefficient is 10 times bigger than the binary diffusion coefficient if the alloy is P saturated. Assuming the meteorite is P saturated, the Ni diffusion coefficient is $D = 20.24 \times \exp(-3.49 \times 10^4 / T)$ in the FeNi. The size of the precipitate can be estimated using the equation $x = \sqrt{Dt}$ where the x is the diffusion distance and the t is time [Porter and Easterling, 1981]. The time t can be calculated from the cooling rate of the given meteorite (0.5 K/Myr). For the temperature range from 300°C to 200°C, one can expect the precipitates of ~70 nm. This size is in good agreement with the size of the precipitates found in the meteorite.

5.7.2 Cloudy Zone

The formation of the CZ also can be understood through Figs. 5.5, 5.6 and 5.7. As cooling continues below 400°C, the composition range behind TR (<41 wt.%) remains as supersaturated solid solution and then falls into the spinodal region around 320°C. The segment a-b on the phase diagram in Fig. 5.6 corresponds to the CZ region in the mesosiderite investigated in this study. The point a could be lower for the iron meteorites which have been cooled faster. Once the taenite falls into the spinodal region, decomposition occurs spontaneously producing Ni-rich (island phase) and Ni-poor (honeycomb phase) regions defined by the miscibility gap. At 300°C for example, the region containing the highest Ni content, about 41wt.% Ni, decomposes into Ni-rich regions containing ~51 wt.% Ni and Ni-poor regions containing ~26 wt.% Ni. The Ni-rich regions undergo the ordering transformation. As temperature decreases, the Ni-rich region increases in Ni content , while the Ni-poor regions decreases in Ni content along the miscibility gap. Close to 260°C, the Ni-poor regions undergo a further transformation to α_2 as indicated by the intersection of the miscibility gap and M_s line. As the meteorite cools, The higher Ni region transforms spinodally first, followed at lower temperature by regions of lower Ni content. Therefore the higher Ni regions have more time to grow and coarsen, which is consistent with the size variation found in the CZ, Fig. 4.19. This spinodal decomposition as a mechanism responsible for producing CZ structure has been proposed by various research groups [Jago *et al.*, 1982; Guimarães *et al.*, 1980; Albertsen *et al.*, 1983; Reuter *et al.*, 1988, 1989b].

As observed in this study, the island phase of the CZ contains precipitates. A similar explanation to that made for the precipitate formation in the TR can be applied for the precipitates in the island phase. Fig. 5.8 is a schematic diagram showing the precipitation process in the island phase. The upper diagram is a part of the Fe-Ni phase diagram (Fig. 5.4), and the lower diagram shows a schematic Ni composition profile developed in the island phase during cooling. Since the spinodal decomposition occurs at

low temperature (<320°C), as discussed above, Ni diffusion is so sluggish that Ni piles up at the edge of the island phase. Therefore the island phase will have its own M-shaped profile inside. For example, consider the region containing 40 wt. % Ni (point a in Fig. 5.8). Upon cooling this region remains as supersaturated state until spinodal boundary is reached (point b in Fig. 5.8). At T_1 (~300°C), this region is spinodally decomposed into a disordered γ with low Ni (point c) which forms the honeycomb phase and an ordered γ' with high Ni (point d) which forms the island phase. As temperature decreases ($T_1 \rightarrow T_2$), the island phase grows and increases in Ni content following miscibility gap (d→g). However, the center of the island phase remains as supersaturated γ' with a Ni content of point f due to the sluggish diffusion rate. Once a critical undercooling (ΔT_c) is reached the supersaturated region inside the island phase decomposes into the high Ni island phase containing Ni content defined by the high Ni miscibility gap (point g) and the precipitates containing Ni content defined by low Ni miscibility gap (point g).

In summary, the taenite decomposition process was described using the new phase diagram. The final microstructures at low temperature formed by various, complicated transformation mechanism. The development of microstructures in the TR and the CZ of meteorites during cooling is schematically illustrated in Fig. 5.9.

5.8 Cooling Rate of Meteorites

5.8.1 New Cooling Rate Indicator

The cloudy zone in the retained taenite of meteoritic metal contains spinodally decomposed high Ni island phases. There is a concentration gradient through the cloudy zone and the size of the island phase varies with local Ni concentration as discussed in section 4.2.1. The constituents of the cloudy zone grow as the host meteorite cools and the size of the island phase is controlled by the cooling rate and Ni concentration. However, since the Ni concentration at which the cloudy zone starts to develop is almost

constant (about 46 wt% Ni), one can choose to measure the size of the island phase in the cloudy zone at this interface. This procedure eliminates Ni concentration as a variable. At this interface, the cloudy zone of any specific meteorite has the highest local Ni content and the biggest island phase. As shown in Fig. 4.27, there is a clear relationship between the size of the biggest island phase and the cooling rate of meteorites. Consequently, it is proposed that this size variation can be used to estimate the low temperature cooling rate of the meteorite [Yang *et al.*, 1993, 1994]. The size of the biggest island phase decreases with increasing cooling rate without regard to whether the host is an iron, stony-iron or stony meteorite. Therefore, this method is applicable to metal in iron, stony-iron meteorites and chondrites. However, there is a potential source of error in measurement of the biggest island size. The size of the biggest island phase is measured on the sectioned surface. Assuming the cylindrical shape of the island phase, the width of the island phases will be underestimated if the island phase has not been sectioned through its center. Therefore, increasing the number of measurements will provide a reliable result. In this study, more than 30 measurements were performed for each meteorite.

5.8.2 Cooling Rate Variation

There appear to be two size groups of mesosiderites as shown in Table 4.2; the first group with a width of the island phase about 460 nm including Patwar, Barea, Pinnaroo, and Estherville, and the second group with an approximately 390 nm sized island phase including Chinguetti and RKPA79015. These data suggest that the mesosiderites may have varying cooling rates. According to the AEM data obtained in this study, the Ni content measured at the kamacite in Estherville, 2.9±0.1 wt.% Ni, which is in the first group is lower than that in RKPA 79015, 3.6±0.2 wt.% Ni, which is in the second group. The slower cooling resulted in a lower equilibration temperature and therefore a lower Ni content in the kamacite because the solubility limit of Ni in α

decreases with decreasing temperature below ~400°C (Fig. 5.4). This implies that Estherville has cooled more slowly than RKPA 79015. The AEM result is consistent with the new cooling rate method.

Even if pallasites are classified as a stony-iron meteorite, the metallic phases in pallasites have Ni, Ge, and Ga contents that are similar to those in group IIIAB iron meteorites [Dodd, 1981; McSween, 1987]. In Fig. 4.27, the cooling rates appear to vary in the IIIAB-pallasite group meteorites. The measured island size and cooling rate are shown in Table 5.2 along with bulk Ni content. The cooling rate variation observed in this study suggests that pallasites and IIIAB iron meteorites do not form in one parent body. Buseck and Goldstein [1967] proposed that only a few of the iron meteorites formed together with the pallasites if the pallasites occurred in different parent bodies from the iron meteorites, or at least from the bulk of the iron meteorites. They suggested these iron meteorites belong to group IIIB based on the Ni content, similarities in trace elements, structures, and cooling rates.

An interesting case here that is in dispute is the range of cooling rates in IVA iron meteorites. Early papers reported IVA cooling rates negatively correlated with Ni content, ranging from 100 K/Myr at the low Ni extreme to ~5 K/Myr at the high Ni extreme [Moren and Goldstein, 1978, 1979]. In this study, however, the correlation of cooling rate with bulk Ni composition was not observed. Instead, it was found that the cooling rates vary randomly with Ni concentration for the IVA group iron meteorites as shown in Fig. 4.27 and Table 5.3. Recently, Scott *et al.* [1994] suggested that the parent body of the group IVA iron meteorites was catastrophically fragmented while the core was cooling between 1400°C and 1200°C, and that fragments of core and mantle were reassembled; cool mantle fragments and hot core fragments were probably mixed together. Therefore, the cooling rates may vary randomly with Ni concentration, which is consistent with the results obtained in this study.

6. SUMMARY

Various AEM techniques were used to investigate the microstructure and microchemistry of the low temperature phase transformation products in the Fe-Ni system. The results of this study are summarized below.

(1) The tetrataenite rim is composed of low Ni bcc precipitates in a high Ni $L1_0$ ordered FeNi matrix. The outermost layer of the TR is most likely the $L1_2$ (Ni_3Fe) ordered structure. Close to the kamacite interface, the average Ni content is 65.5 ± 3.3 wt.%. The measured Ni content of precipitates in RKPA 79015 is 14.2 ± 1.0wt.% Ni. Considering beam broadening, small size of the precipitates and specimen drift, the true Ni content of the precipitates is possibly the same as the Ni content of the honeycomb phase (9.0 ± 1.0 wt.% Ni). The Ni content of kamacite at the TR interface was 3.6 ± 0.2 wt.% Ni. The Ni content of the matrix as a function of position within the tetrataenite rim was investigated. The Ni composition of the ordered FeNi matrix is consistent throughout the TR in RKPA 79015. The average Ni composition measured was 51.8 ± 1.7 wt.% Ni.

(2) The sub-zone structure within the tetrataenite rim, which corresponded to the clear taenite I region, was observed in iron, stony-iron and stony meteorites. It is likely that the sub zone structure is a general feature of all kind of meteorites. Each zone can be distinguished by its color in the LOM image. Apparently, clear taenite I region is not truly clear. Therefore, it is suggested to rename this region the "tetrataenite rim (TR)" because of its structural features. This sub-zone structure is due to the fact that the tetrataenite rim is composed of low Ni precipitates in a high Ni ordered FeNi matrix. The low Ni precipitates are easily etched away during the chemical treatment for the LOM observation, resulting in dark contrast in the LOM images. The density of the precipitates decreases with increasing Ni content in the TR, and the precipitate is absent in the outermost part of the TR. The region close to the TR/CZ boundary (zone 1) has the

highest density of precipitates but a less dense network of APBs. This region corresponds to the layer of light gray color in the LOM image. The middle of the TR (zone 2) has a higher density of APBs associated with the precipitates while the density of precipitates is lower than that in zone 1. This region corresponds to the layer of dark gray color in the LOM image. Zone 2 appears to be darker than zone 1, although zone 2 has less precipitates than zone 1. This observation is most likely because zone 2 has a denser network of APBs associated with precipitates, which has been more heavily attacked by the chemical etch than the precipitates themselves. The outer region of the TR (zone 3) has no precipitates and corresponds to the bright white color in the LOM image.

(3) The TR in the Saint Séverin ordinary chondrite also consists of low Ni bcc precipitates and high Ni $L1_0$ ordered FeNi matrix. The CZ structure of this chondrite is very similar to other meteorites examined in this study. This is the first TEM observation of an ordinary chondrite.

(4) The cloudy zone is composed of low Ni honeycomb phases and island phases with precipitates inside. The honeycomb has a bcc structure in RKPA 79015, Estherville, and Saint Severin. In RKPA 79015, the Ni composition of the honeycomb phase is 9.0 ± 1.0 wt.% Ni. The island phase exhibits $L1_0$ superlattice reflections. In RKPA 79015, the Ni composition is 51.8 ± 1.7 wt.% Ni indicating that the island phase is ordered FeNi with the $L1_0$ superstructure. The crystal structure of the precipitate within the island phase is identified as a bcc by electron diffraction. The measured Ni content of the precipitates in RKPA 79015 is 14.7 ± 1.0 wt.%. This Ni content is essentially the same as the Ni content of the precipitates in the TR. Considering possible contribution of X-rays from the high Ni matrix by beam broadening and specimen drift, the true Ni content of the precipitates may be the same as the Ni content of the honeycomb phase (9.0 ± 1.0 wt.%

Ni). Investigating the Ni content of the island phase as a function of position within the CZ, it was observed that the Ni composition of the island phase is consistent throughout the CZ in RKPA 79015. The average Ni composition measured is 51.8 ± 1.7 wt.% Ni. This is consistent with the Ni content obtained from the ordered FeNi matrix in the TR.

(5) The low temperature Fe-Ni phase diagram is modified using the AEM data obtained from meteorites in this study. A monotectoid reaction ($\gamma_1 \rightarrow \alpha + \gamma_2$) at about 400°C and a eutectoid reaction ($\gamma_2 \rightarrow \alpha + \gamma'$) at 345°C are incorporated in the new phase diagram. At low temperatures, α and γ' (Ni_3Fe) phases are in equilibrium , while γ'' (FeNi) phase is present as a metastable phase.

(6) A new method to determine the low temperature cooling rate of the meteorite has been established. By measuring the size of the biggest island phase in the CZ, one can estimate the low temperature cooling rate of the meteorite. The size of the biggest island phase clearly decreases with increasing cooling rate without regard to whether the host is an iron, stony-iron or stony meteorite. The size of the biggest island phase of the meteorites that were investigated in this study varies approximately from 470 nm to 17 nm, while the cooling rate varies from 0.5 K/Myr to 325 K/Myr. The cooling rates appear to vary in the IIIAB-Pallasite group meteorites. The cooling rates vary randomly with Ni concentration for the IVA group iron meteorites.

Table 2.1 Comparison of chemical and structural classifications for iron meteorites [McSween, 1987]

Chemical Groups	Structural Classes						
	Hexahedrites	Octahedrites					Ataxites
	H	Ogg	Og	Om	Of	Off	D
IAB			******	******			
IC			******				
IIAB	*******	******					
IIC						******	
IID				******	******		
IIE			******	******			
IIIAB			******	******			
IIICD					******	******	*******
IIIE			******				
IIIF		******	******	******	******		
IVA					******		
IVB						******	

Table 2.2 Classification of chondrites [Dodd, 1981]

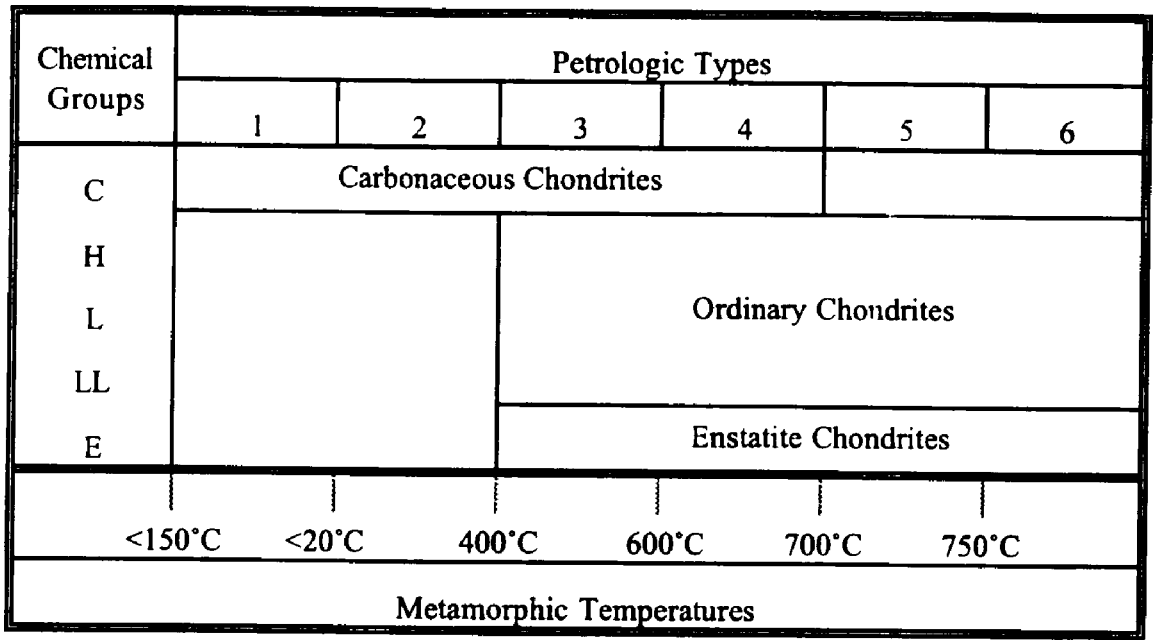

Table 3.1 Iron meteorites examined in this study

Name of Meteorite	Class	Group	Bulk wt.%Ni
Toluca	Octahedrite(Og)	IAB	8.14
Carbo	Octahedrite(Om)	IID	10.2
Cape York	Octahedrite Om)	IIIAB	7.84
Cumpas	Octahedrite(Om)	IIIAB	8.04
Spearman	Octahedrite(Om)	IIIAB	8.61
Grant	Octahedrite(Om)	IIIAB	9.34
Tazewell	Octahedrite(Off)	IIICD	16.9
Dayton	Octahedrite(Off)	IIICD	17.6
Bishop Canyon (USNM 770)	Octahedrite(Of)	IVA	7.76
Gibeon (USNM 1497b)	Octahedrite(Of)	IVA	7.93
Bristol (USNM 1324)	Octahedrite(Of)	IVA	8.07
Duchesne	Octahedrite(Of)	IVA	9.37
New Westville (USNM 1412)	Octahedrite(Of)	IVA	9.40
Chinautla (USNM 742)	Octahedrite(Of)	IVA	9.44

Table 3.2 Stony meteorites examined in this study

Name of Meteorite	Class	Group
Richardton (USNM 595)	ordinary chondrite	H5
Guareña (USNM 1469)	ordinary chondrite	H6
Kernouve	ordinary chondrite	H6
Saint Séverin	ordinary chondrite	LL6

Table 3.3 Stony-iron meteorites examined in this study

Name of Meteorite	Class
Barea (USNM 1468)	mesosiderite
Chinguetti(USNM 3250)	mesosiderite
Estherville	mesosiderite
Patwar (USNM 1243)	mesosiderite
Pinnaroo (USNM 2312)	mesosiderite
RKPA 79015	mesosiderite
Imilac	pallasite
Glorieta Mountain	pallasite
Newport	pallasite

Table 4.1 Measurements of the biggest island phase in the cloudy zone of iron meteorites

Name of Meteorite	Type	Cooling Rate (K/Myr)	Island Phase	
			Width (nm)	σ (nm)
Toluca	Iron (IAB)	25.0	110.5	10.1
Carbo	Iron (IID)	5.0	133.6	12.5
Cape York	Iron (IIIAB)	15.0	47.6	4.6
Cumpas	Iron (IIIAB)	11.0	50.6	6.7
Spearman	Iron (IIIAB)	10.0	59.3	7.6
Grant	Iron (IIIAB)	7.5	56.6	4.9
Tazewell	Iron (IIICD)	10.0	91.5	3.3
Dayton	Iron (IIICD)	10.0	99.0	9.5
Bishop Canyon	Iron (IVA)	325.0	23.2	3.9
Gibeon	Iron (IVA)	250.0	33.2	5.3
Bristol	Iron (IVA)	250.0	23.2	2.3
Duchesne	Iron (IVA)	60.0	33.4	3.3
New Westville	Iron (IVA)	35.0	17.8	2.6
Chinautla	Iron (IVA)	40.0	38.7	2.9

Table 4.2 Measurements of the biggest island phase in the cloudy zone of stony-iron and stony meteorites

Name of Meteorite	Type	Cooling Rate (K/Myr)	Island Phase	
			Width (nm)	σ (nm)
Guareña	Chondrite (H6)	4.3	126.3	15.7
Kernouve	Chondrite (H6)	17.0	91.2	6.3
Saint Séverin	Chondrite (LL6)	3.0	240.3	37.1
Barea	mesosiderite	0.5	463.5	34.5
Chinguetti	mesosiderite	0.5	389.1	47.0
Estherville	mesosiderite	0.5	462.9	31.7
Patwar	mesosiderite	0.5	468.7	31.5
Pinnaroo	mesosiderite	0.5	462.6	57.0
RKPA 79015	mesosiderite	0.5	386.5	20.1
Imilac	pallasite	2.5	171.7	21.9
Glorieta Mountain	pallasite	2.0	178.5	17.5
Newport	pallasite	5.0	158.4	16.9

Table 4.3 References for the metallographic cooling rates of iron meteorites

Name	Cooling Rate (K/Myr)					
	S(88)	R(82)	MG(79)	WW(78)	G(69)	GS(67)
Toluca	25.0				2.0	1.6
Carbo					1.0	1.0
Cape York					3.0	
Cumpas					2.2	
Spearman						4.0
Grant					1.5	5.1
Tazewell	10.0				2.0	2.2
Dayton					2.0	6.5
Bishop Canyon		96.0			65.0	
Gibeon		56.0	6.0	25.0	50.0	20.0
Bristol	150-300				50.0	20.0
Duchesne		2.0	4.0		12.0	9.0
New Westville			3.0	13.0	7.0	
Chinautla			6.0		8.0	

S(88) : Saikumar et al. [1988]

R(82) : Rasmussen [1982]

MG(79) : Moren and Goldstein [1979]

WW(78) : Willis and Wasson [1978]

G(69) : Goldstein [1969]

GS(67) : Goldstein and Short [1967]

Table 5.1 Measured Ni content of the various regions in the meteoritic metal

Location		Symbol	Ni Content (wt.%)
Kamacite	K/TR	α	3.6±0.2
TR	TR/K	γ'	65.5±3.3
	Matrix	γ''	51.2±1.4
	PPT	α_2	14.2±1.0
	TR/CZ	$\gamma''+\alpha_2$	46.4±0.7
CZ	Island	γ'	51.8±1.7
	Honeycomb	α_2	9.0±1.0
	PPT	α_2	14.7±1.0

Table 5.2 The cooling rate variation in the group IIIAB iron and Pallasite meteorites.

Name of Meteorite	Type	Cooling Rate (K/Myr)	Island Phase Width (nm)	Bulk Ni (wt.%)
Cape York	Iron (IIIAB)	15.0	47.6	7.84
Cumpas	Iron (IIIAB)	11.0	50.6	8.04
Spearman	Iron (IIIAB)	10.0	59.3	8.61
Grant	Iron (IIIAB)	7.5	56.6	9.34
Imilac	pallasite	2.5	171.7	11.32
Glorieta Mountain	pallasite	2.0	178.5	12.00
Newport	pallasite	5.0	158.4	10.83

Table 5.3 The cooling rate variation in the group IVA iron meteorites.

Name of Meteorite	Type	Cooling Rate (K/Myr)	Island Phase Width (nm)	Bulk Ni (wt.%)
Bishop Canyon	Iron (IVA)	325.0	23.2	7.76
Gibeon	Iron (IVA)	250.0	33.2	7.93
Bristol	Iron (IVA)	250.0	23.2	8.07
Duchesne	Iron (IVA)	60.0	33.4	9.37
New Westville	Iron (IVA)	35.0	17.8	9.40
Chinautla	Iron (IVA)	40.0	38.7	9.44

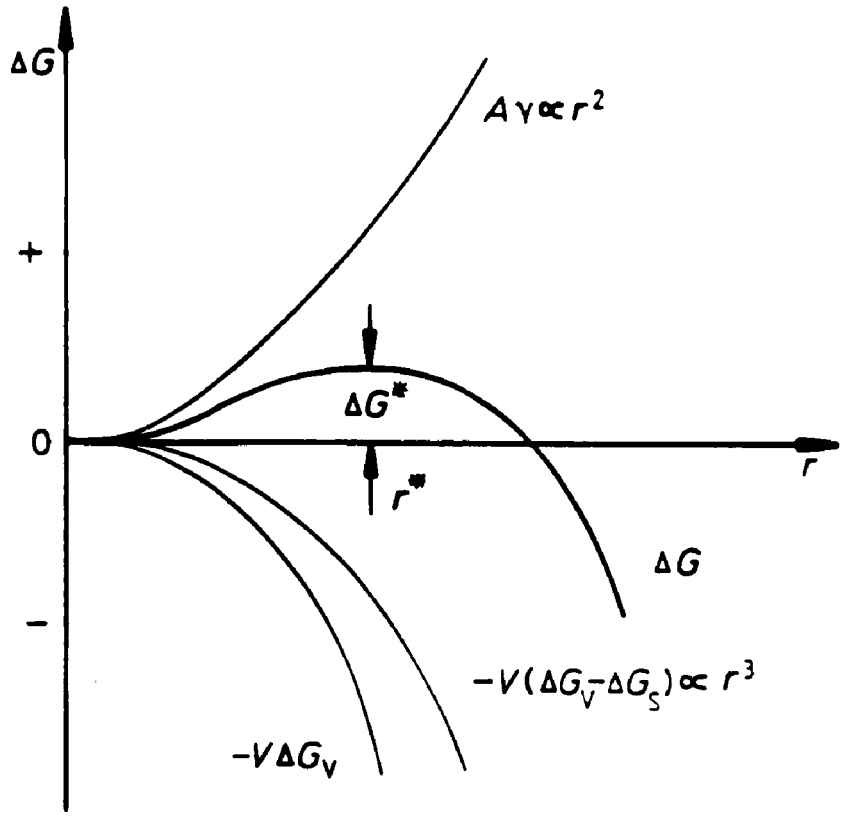

Fig. 2.1 The variation of ΔG with radius r for a nucleus. ΔG is the free energy change due to the formation of a homogeneous nucleus. There is an activation energy barrier ΔG^*. [Porter and Easterling, 1981]

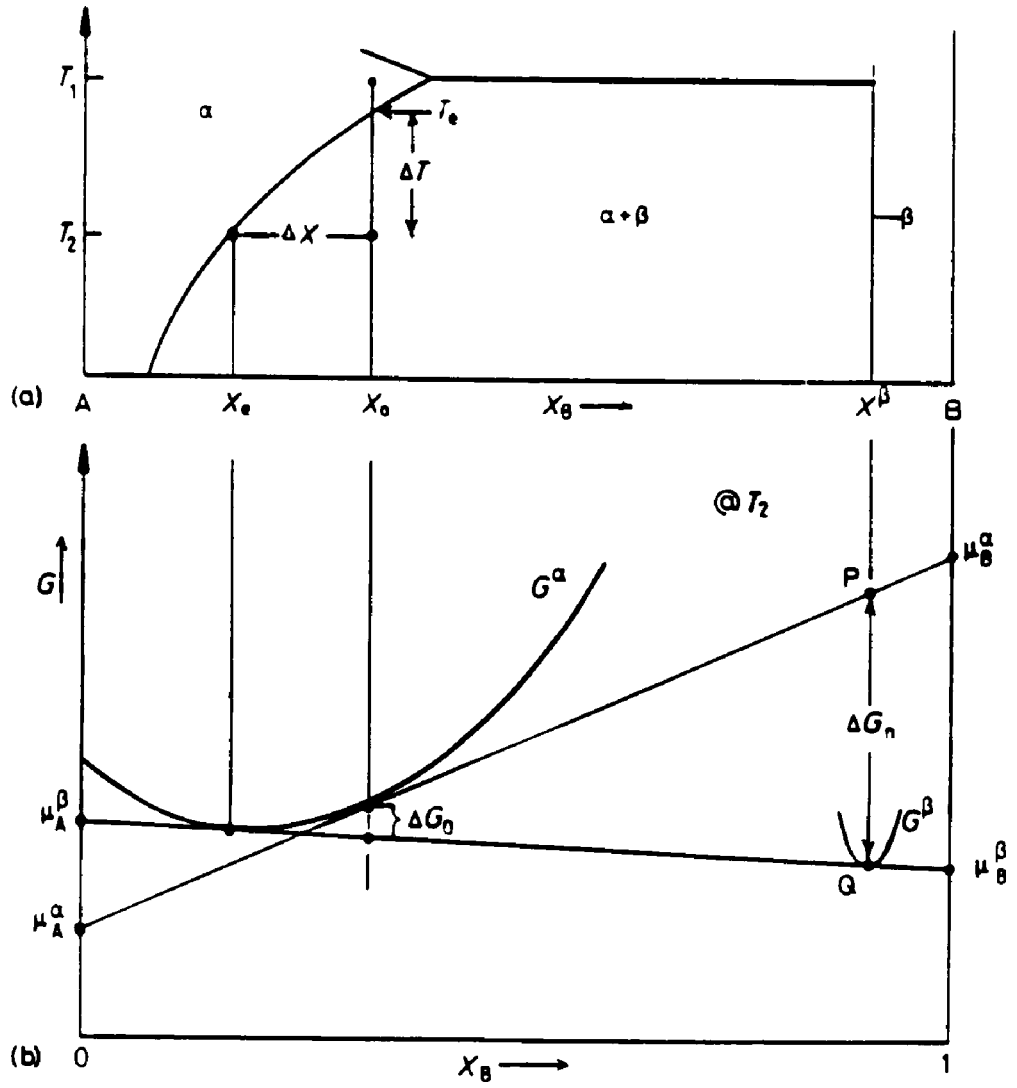

Fig. 2.2 Free energy changes during precipitation. The driving force for the first precipitates to nucleate is ΔG_n. ΔG_0 is the total decrease in free energy when precipitation is complete and equilibrium has been reached. [Porter and Easterling, 1981]

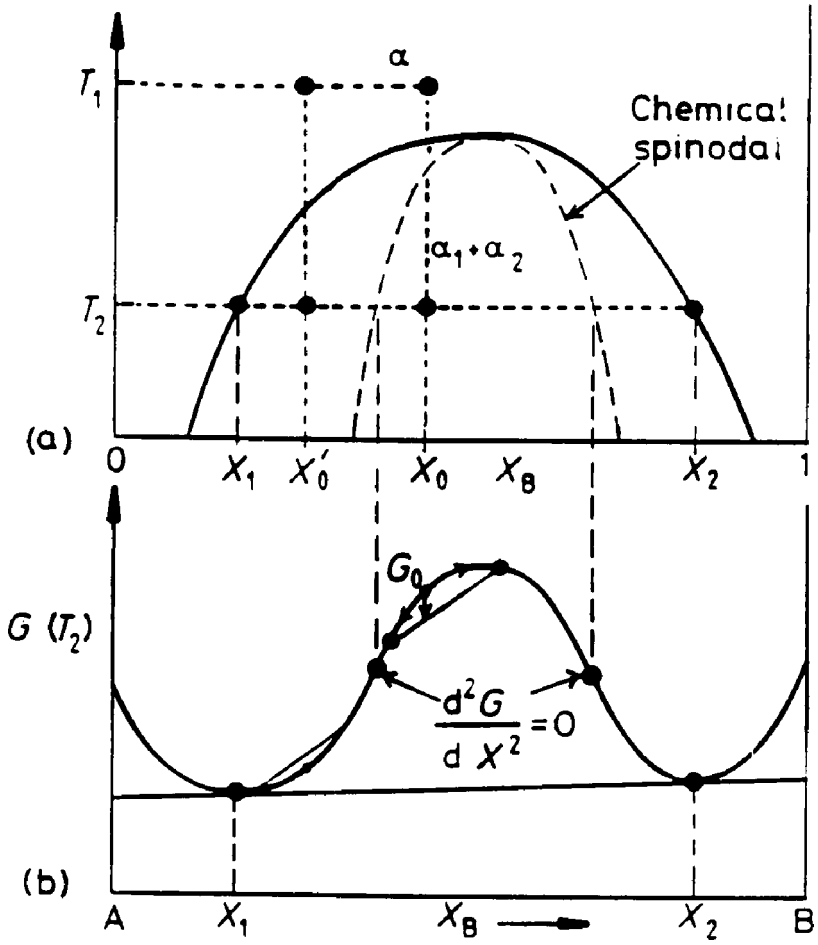

Fig. 2.3 A schematic phase diagram and accompanying free energy (G) versus composition (X) diagram of solid solution exhibiting a spinodal decomposition. Alloys between the spinodal points are unstable and can decompose into two coherent phases α_1 and α_2 without overcoming an activation energy barrier. Alloys between the coherent miscibility gaps and the spinodal are metastable and can decompose only after nucleation of the other phase. [Porter and Easterling, 1981]

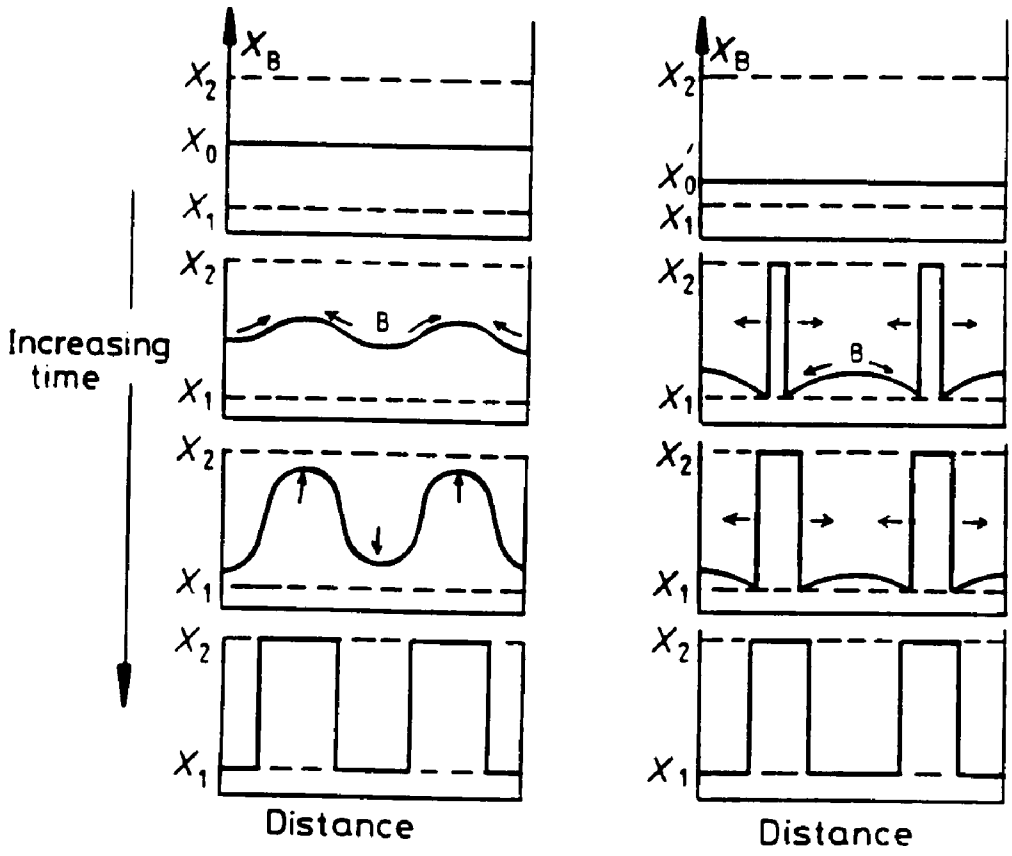

Fig. 2.4 Schematic composition profiles at increasing times in an alloy quenched a) into the spinodal region (X_0 in Fig. 2.3), and b) outside the spinodal points (X_0' in Fig. 2.3)

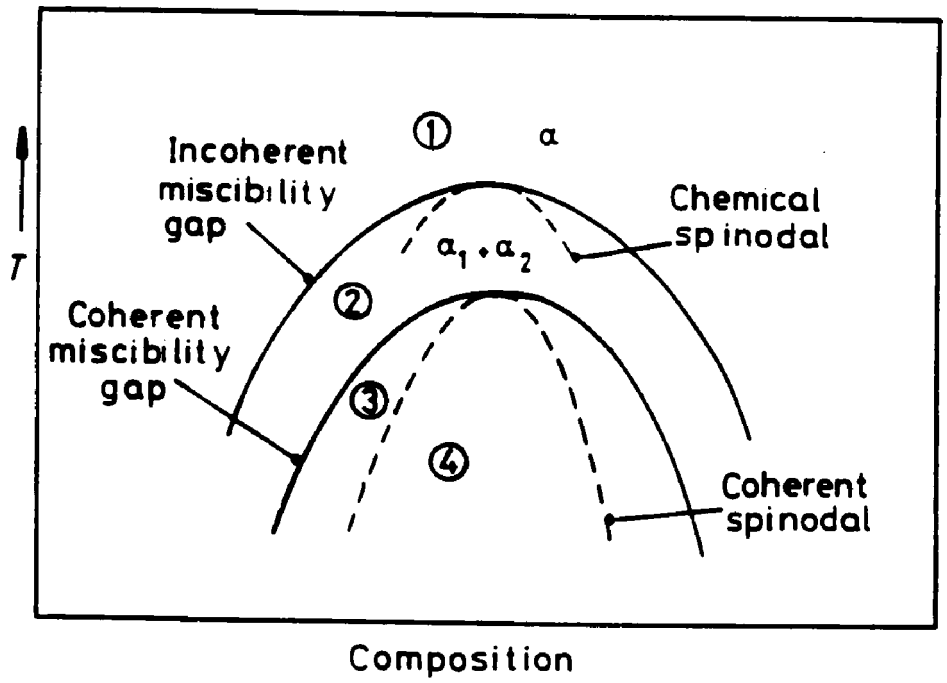

Fig. 2.5 Schematic phase diagram for a clustering system. [Porter and Easterling, 1981]

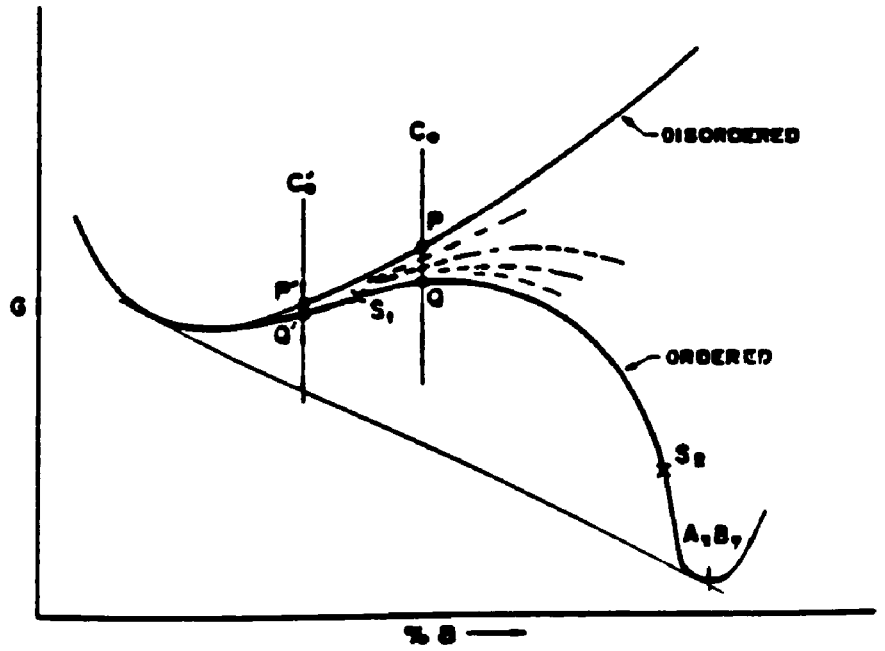

(a)

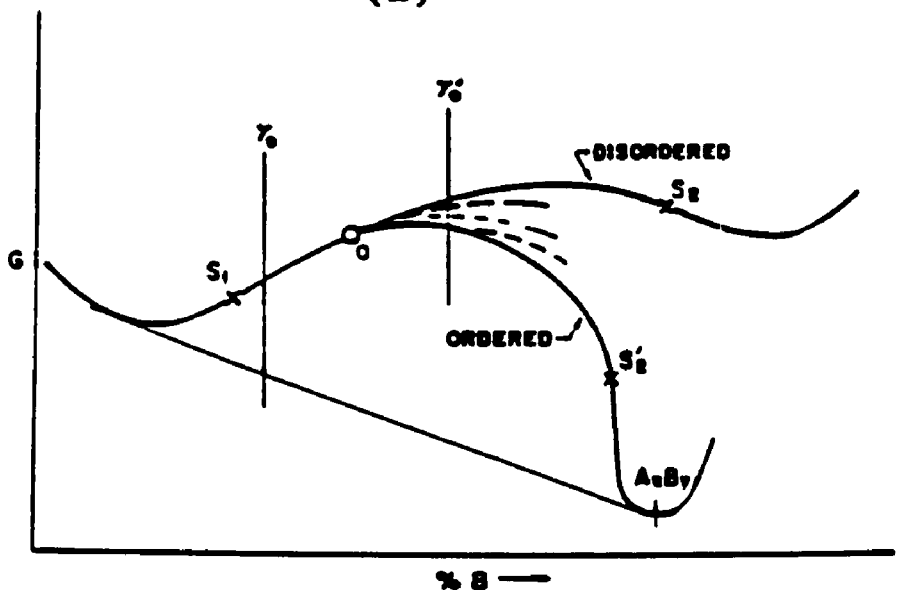

(b)

Fig. 2.6 Schematic free energy-composition diagrams for homogeneous disordered and ordered solid solution showing various possible paths of decomposition [Soffa and Laughlin, 1982].

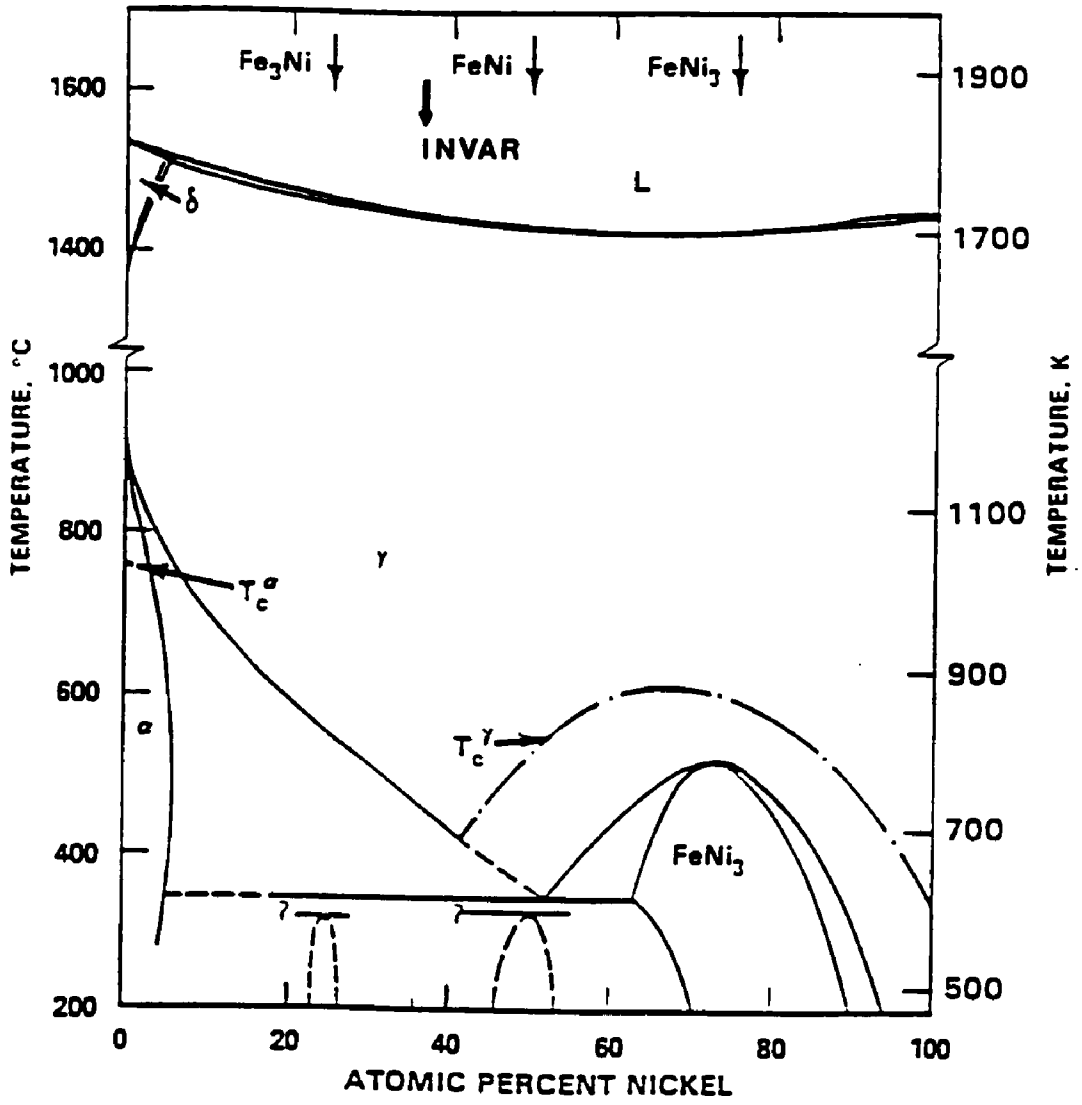

Fig. 2.7 Complete Fe-Ni phase diagram assessed by Kubaschewski [1982].

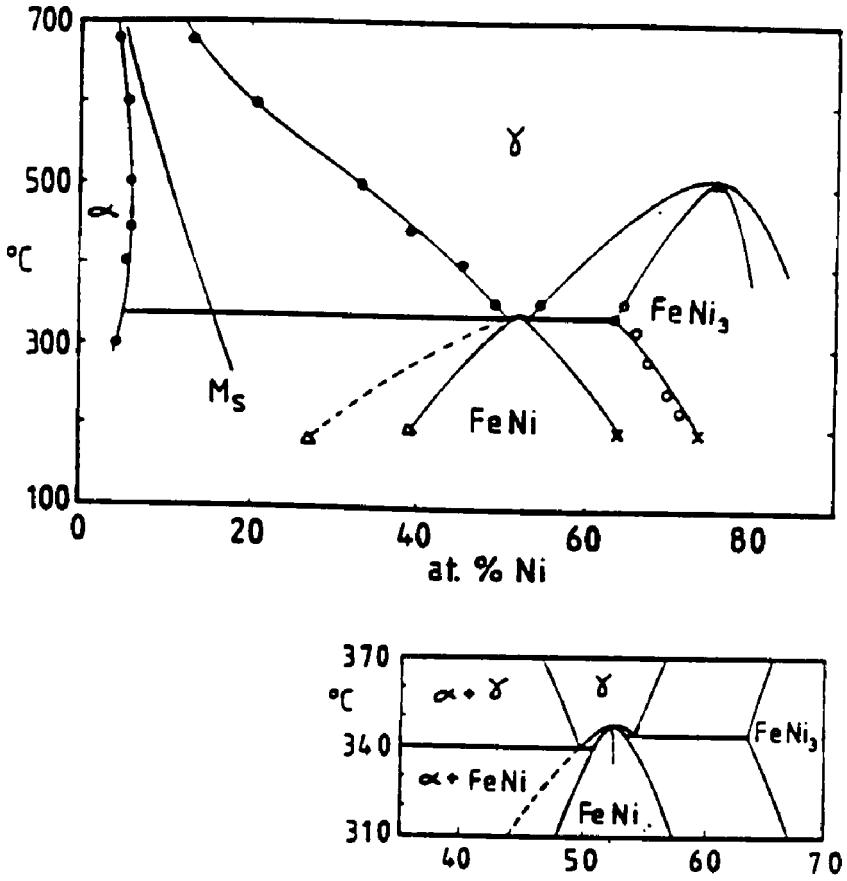

Fig. 2.8 Fe-Ni phase diagram proposed by Rossiter and Jago [1984] based on the investigation of iron meteorite structures.

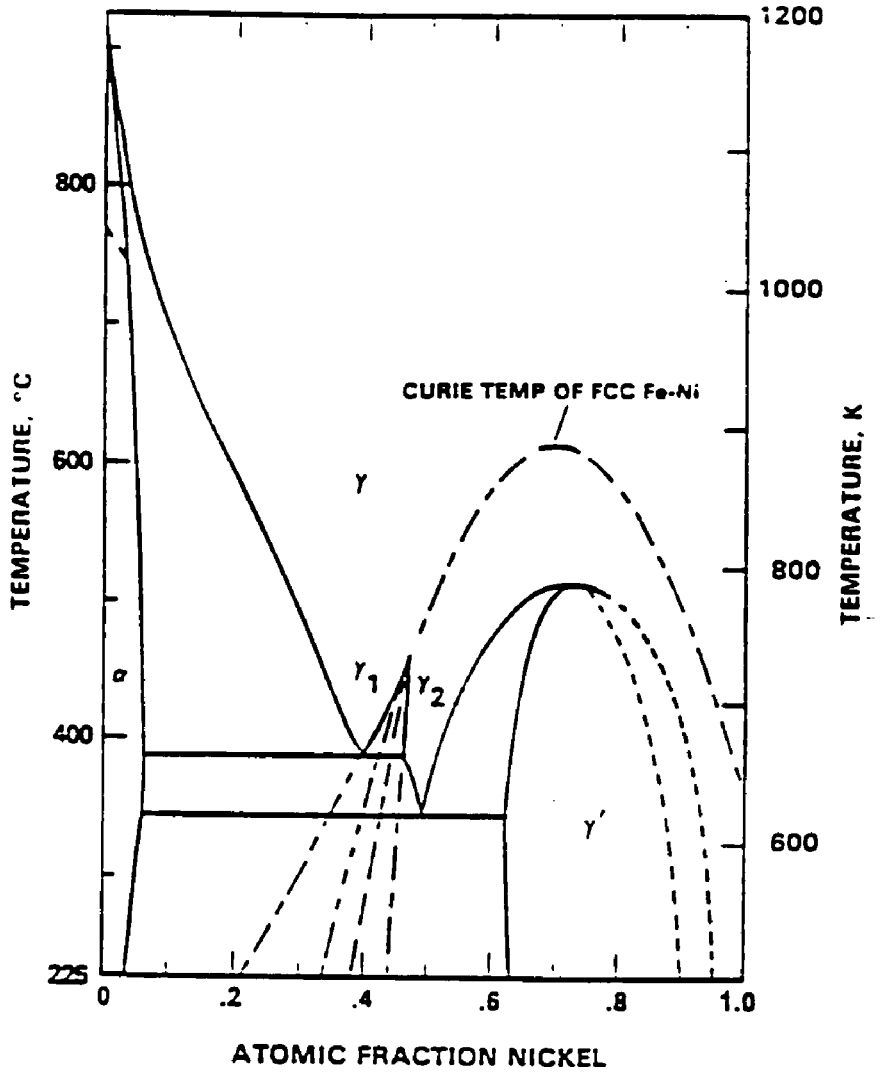

Fig. 2.9 Fe-Ni phase diagram proposed by Chuang *et al.* [1986b]. A miscibility gap induced by magnetic transition is proposed.

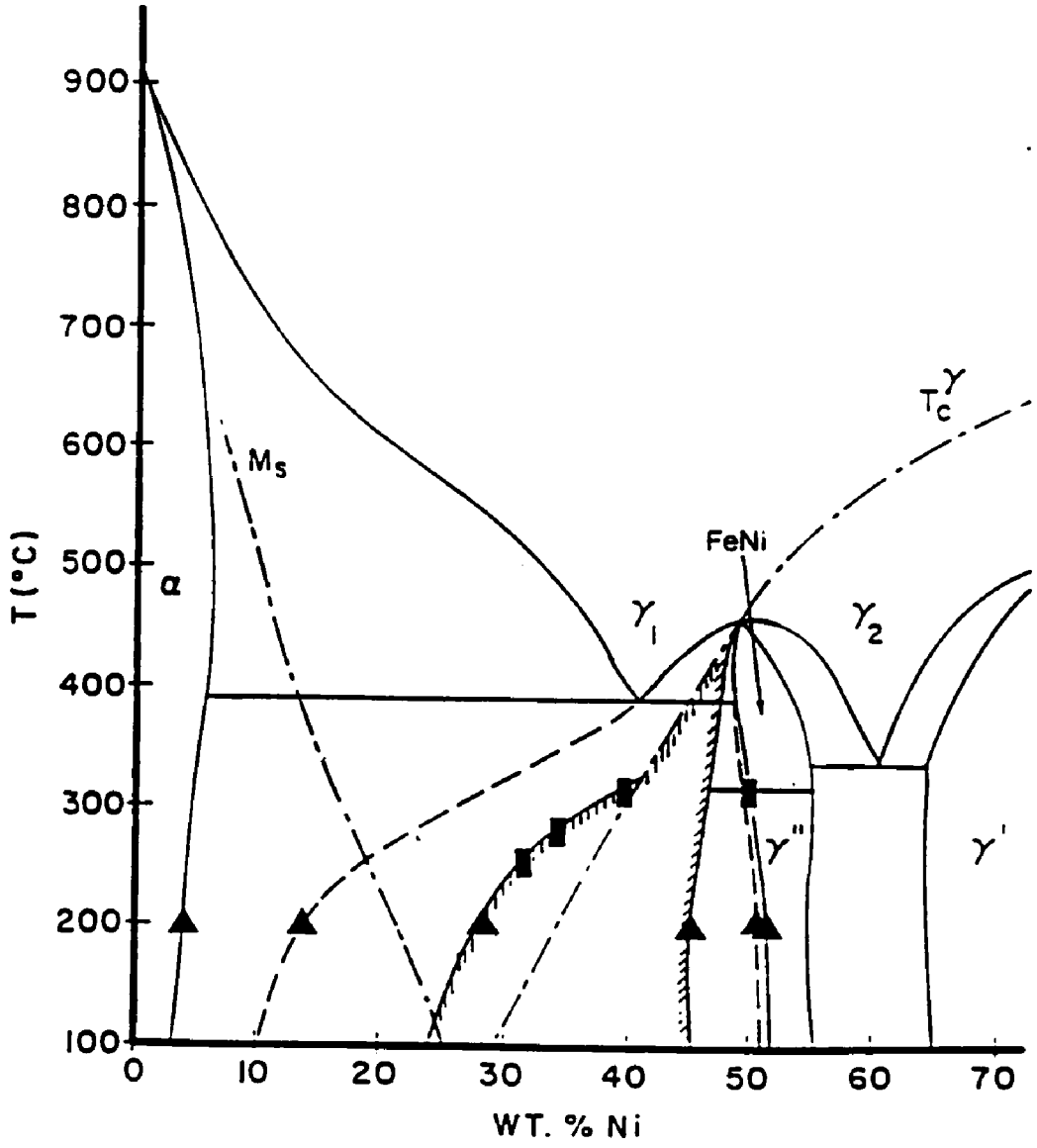

Fig. 2.10 Fe-Ni phase diagram proposed by Reuter *et al.* [1988] based on the investigation of iron meteorite structure and electron irradiated alloys, and the calculated diagram by Chuang *et al.* [1986b].

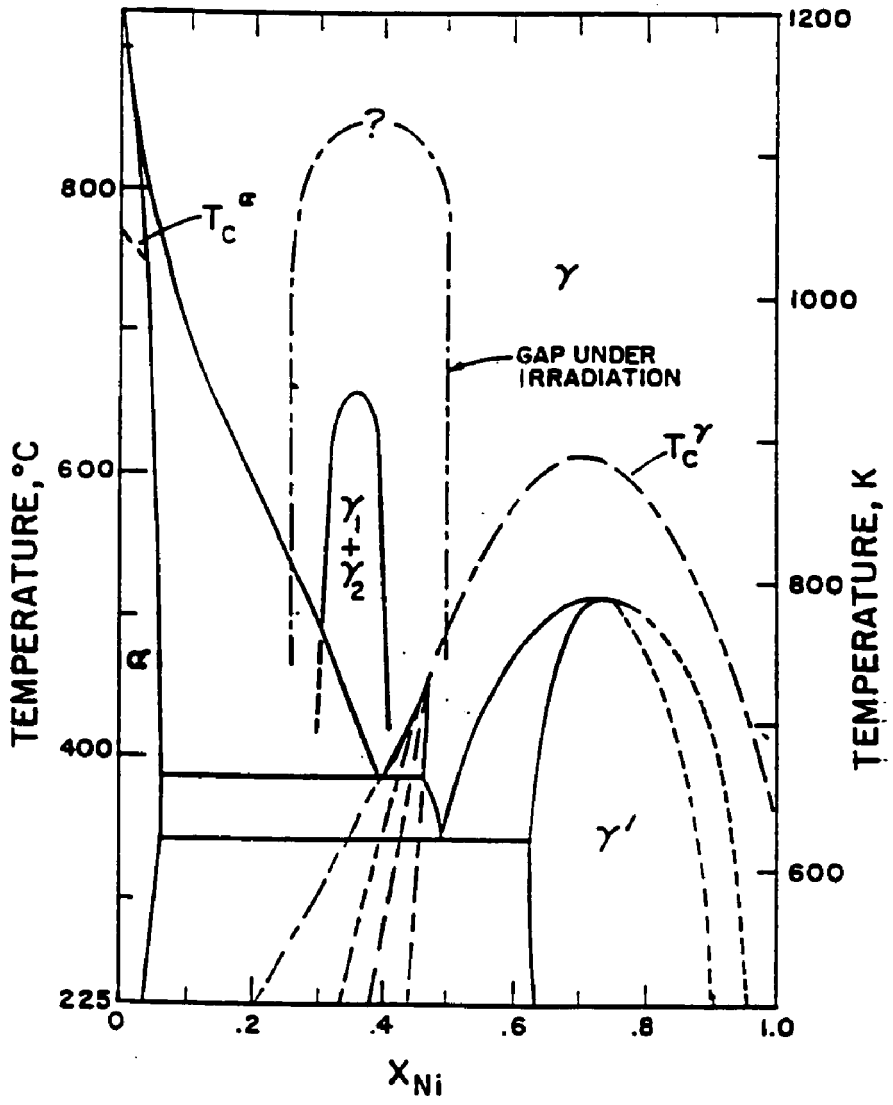

Fig. 2.11 Fe-Ni phase diagram proposed by Russell and Garner [1992] based on the investigation of neutron irradiated alloys. High temperature coherent miscibility gaps for thermally annealed and for irradiated alloys are incorporated.

Fig. 2.12 Light optical micrographs of the Dayton (IIICD) iron meteorite. a) a typical microstructure of the Widmanstätten pattern. b) a typical microstructure of retained taenite.

(a)

(b)

Fig. 2.13 Light optical micrographs of the Saint Séverin (LL6) ordinary chondrite. a) a low magnification image showing taenite (T) and kamacite (K) surrounded by silicates (S). b) a typical microstructure of retained taenite in the Saint Séverin chondrite; TR: tetrataenite rim, CZ: cloudy zone

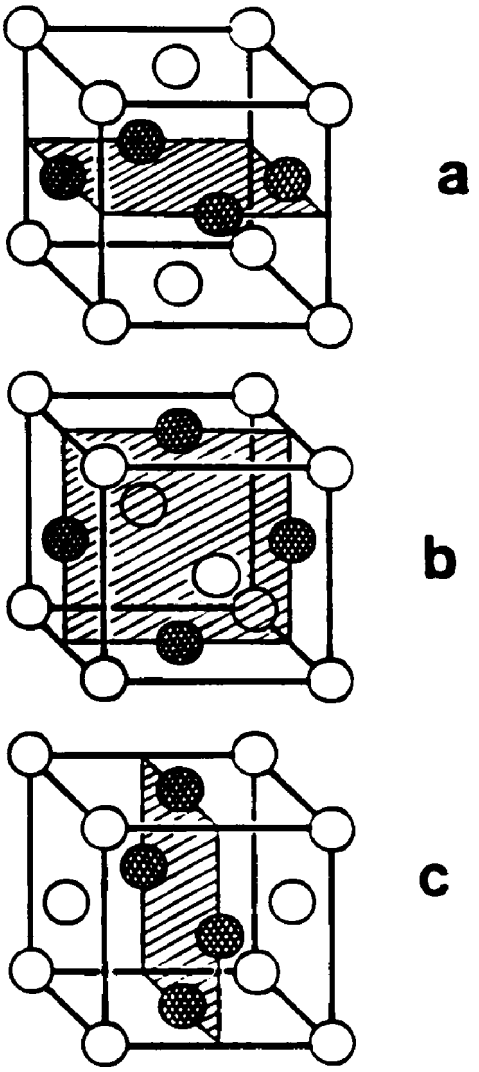

Fig. 2.13 Schematic representation of the $L1_0$ superstructure showing three possible variants.

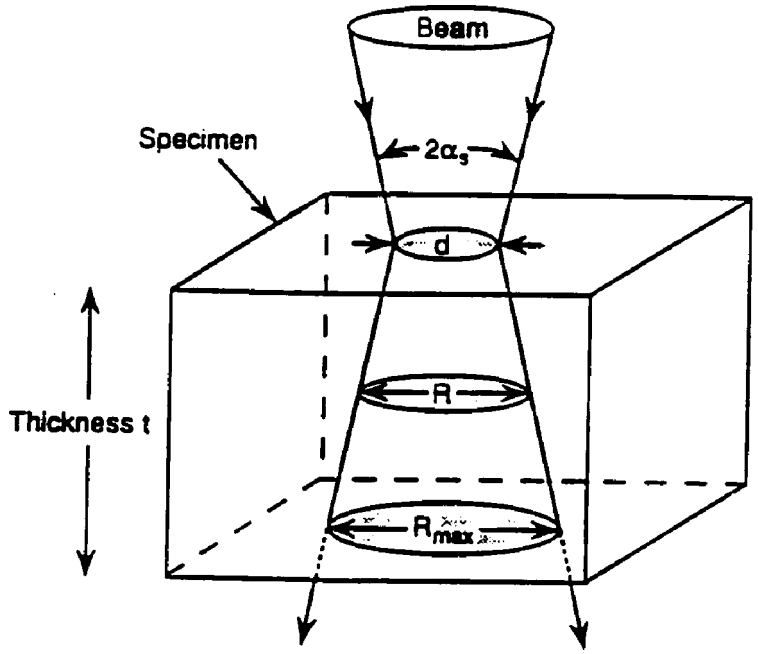

Fig. 2.14 Schematic diagram showing the definition of spatial resolution R in thin foil X-ray microanalysis in AEM [Goldstein *et al.*, 1990].

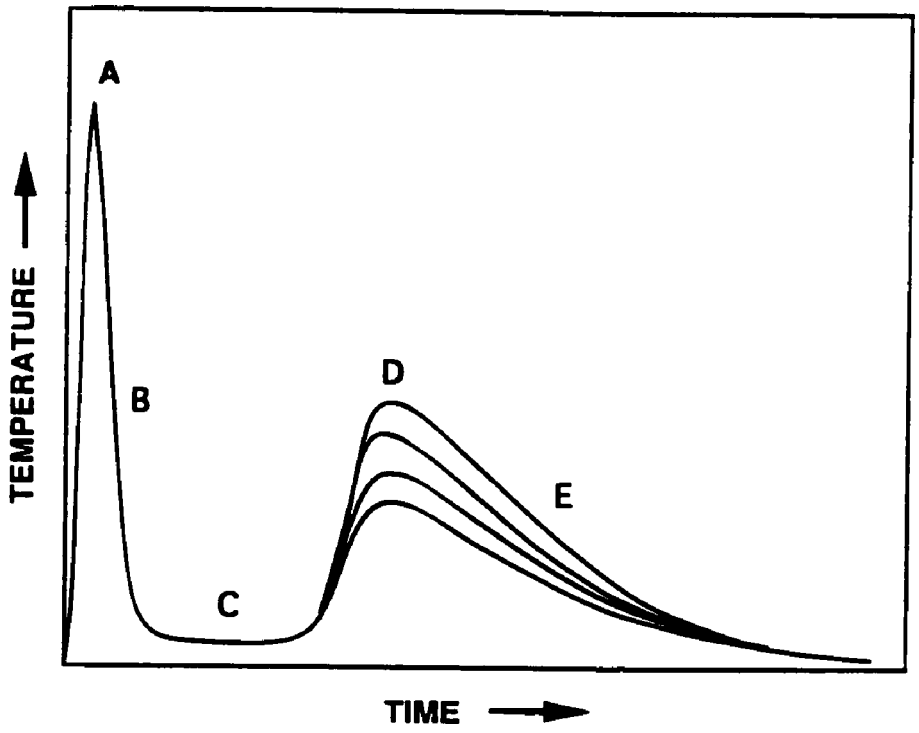

Fig. 3.1 Schematic representation of the thermal history of chondrites
Region A - Primary heating
Region B - Rapid cooling
Region C - Accretion
Region D - Reheating
Region E - Slow cooling

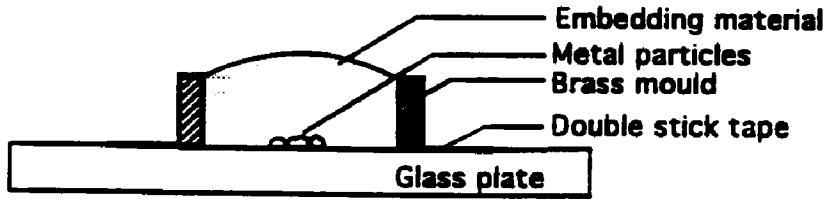

Side View

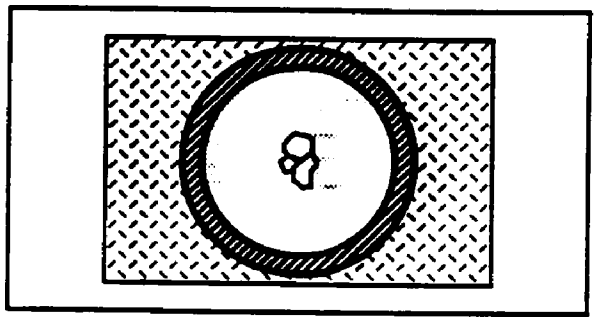

Top View

Fig. 3.2 Schematic illustration of the preparation of 3 mm disc from metal particles.

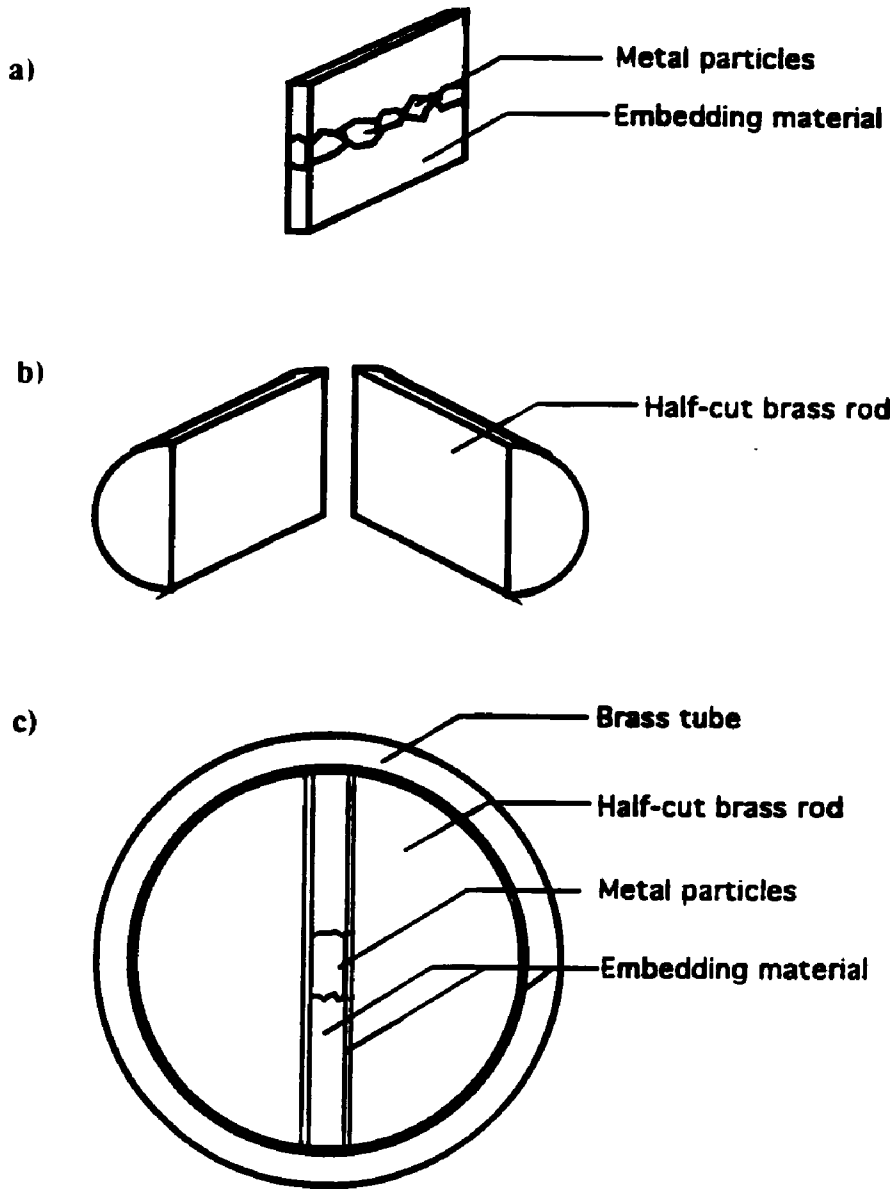

Fig. 3.3 Schematic illustration of the sandwich-type disc preparation.

Fig. 3.4 Photographs of a TEM specimen. a) a light optical micrograph of a TEM specimen before dimple grinding (briefly etched with 2% Nital). b) a SEM micrograph of a TEM specimen after jet polishing and ion beam thinning.

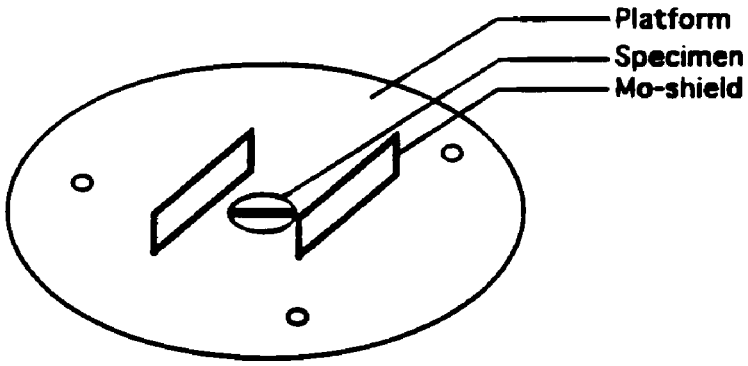

Fig. 3.5 Schematic diagram of the platform of the Mo-shielded specimen holder.

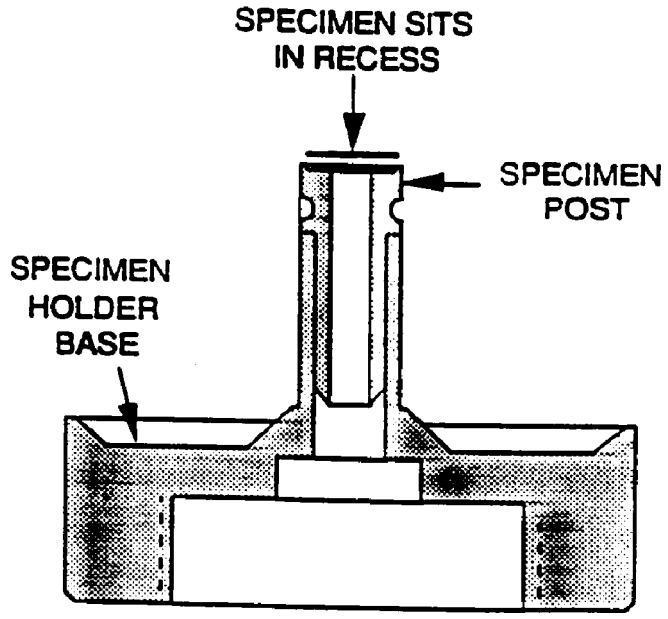

Fig. 3.6 Construction of the single-side low angle specimen holder (Gatan). The specimen post can be removed easily with tweezers to facilitate loading specimens in the holder.

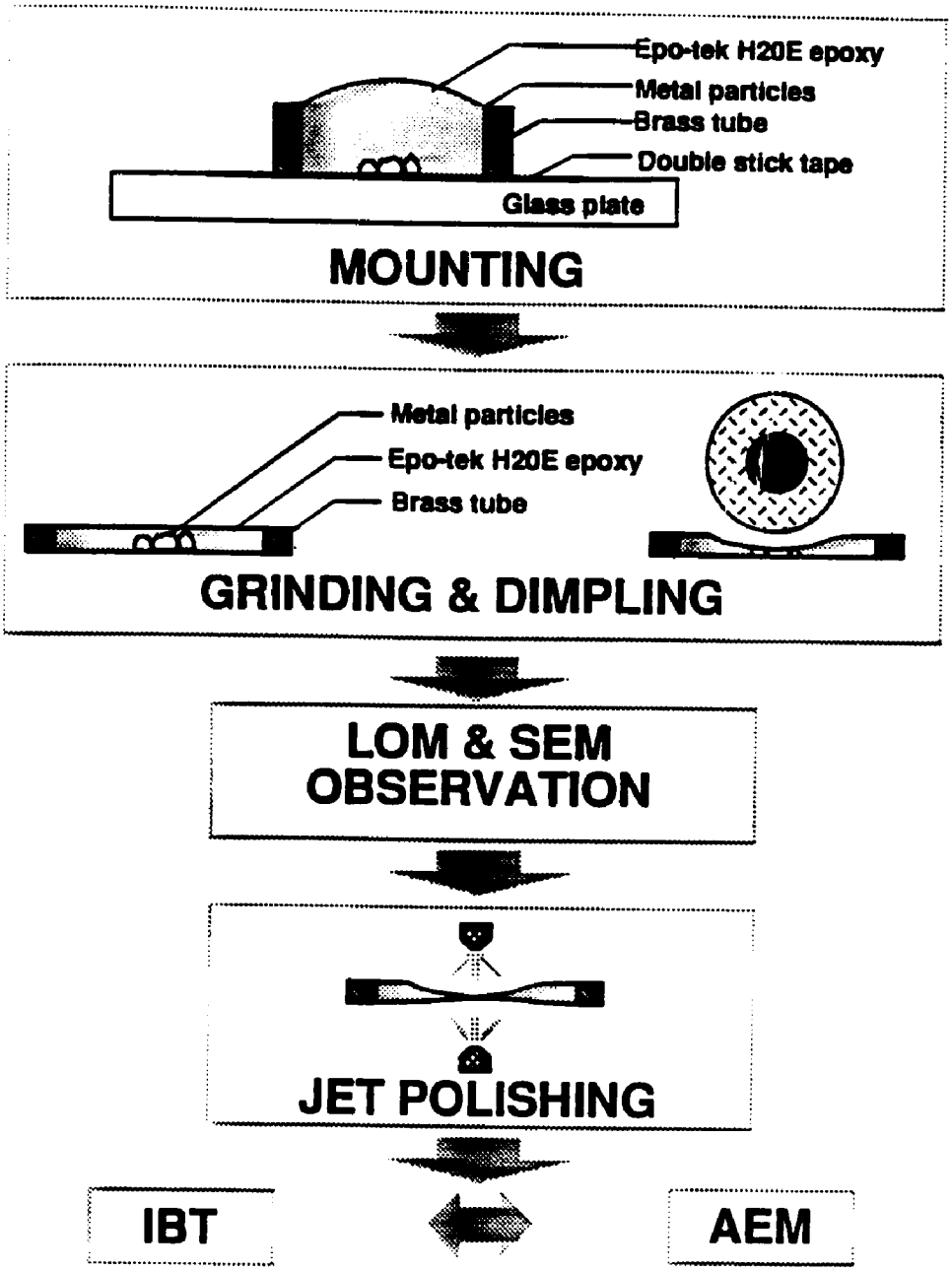

Fig. 3.7 Schematic illustration of the thin foil specimen preparation technique. Metal particles are extracted from the bulk chondrite sample and then mounted into the electro-conducting epoxy (silver glue). After curing, a 3 mm disc is pre-thinned (grinding and dimpling) and jet polished to produce electron transparent regions in the metal particle. If necessary, further ion beam thinning is performed.

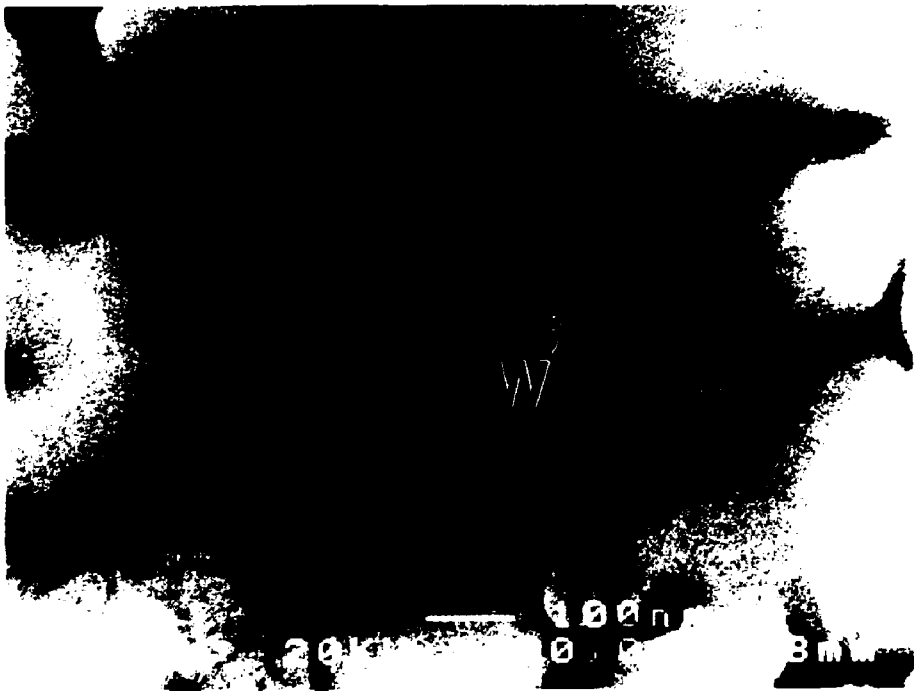

Fig. 3.8 A HRSEM image of the cloudy zone at the region which is close to the outer taenite rim showing the width of the island phase, W.

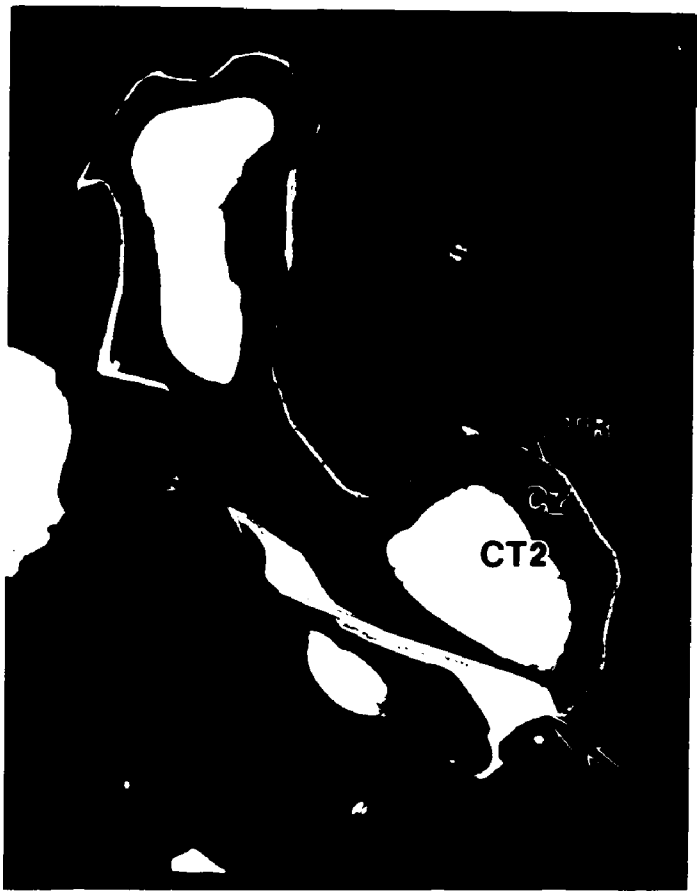

Fig. 4.1 A LOM image of the retained taenite particle in the Guareña (H6) ordinary chondrite.

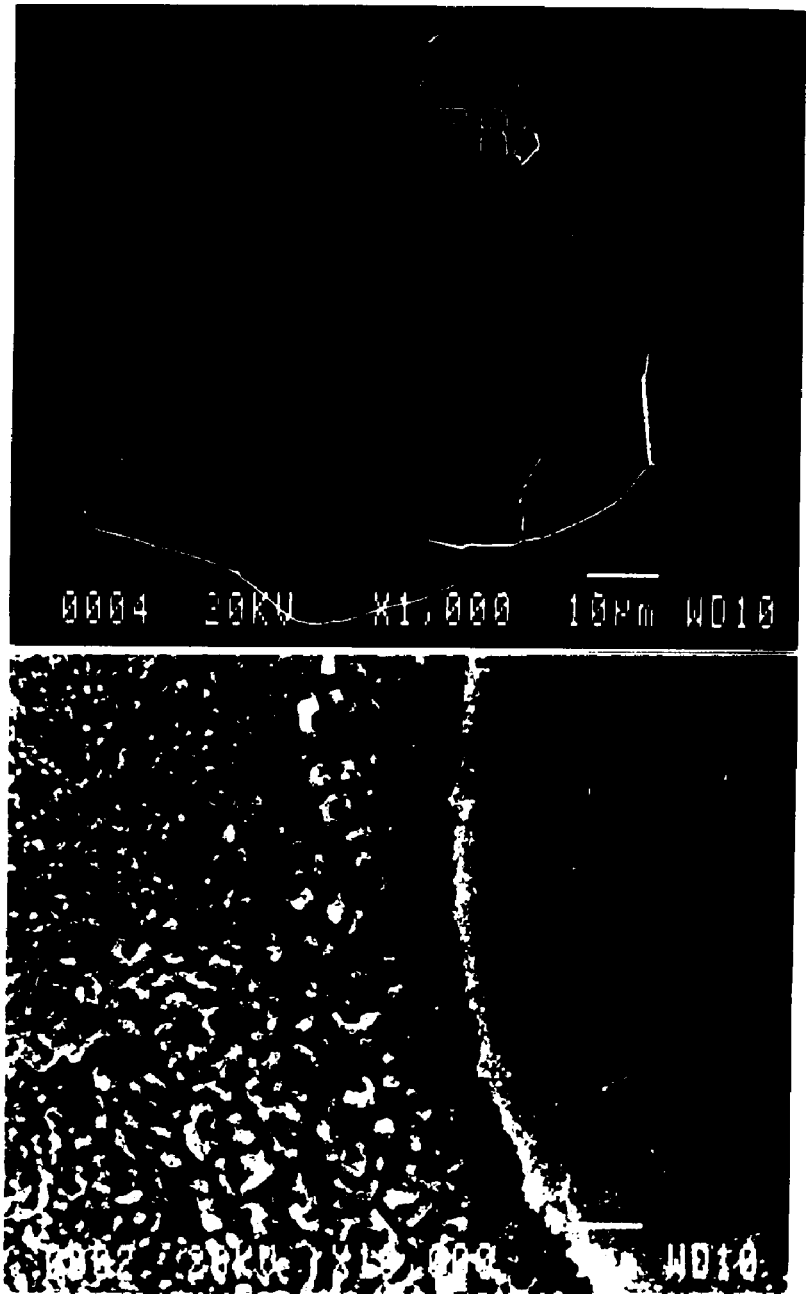

Fig. 4.2 SEM images of a taenite particle in the St. Séverin (LL6) ordinary chondrite. a) is a low magnification image, and b) is a image taken at the edge of the taenite particle surrounded by silicate matrix (S), showing the cloudy zone (CZ) and the tetrataenite rim (TR) which contains three sub-zones (1, 2, and 3). The arrow on the left shows the position of the taenite/cloudy zone (CZ) boundary. The three zones in the tetrataenite rim are observed. The arrows give the general boundaries of zone 1/zone 2 and zone 2/zone 3. The arrow on the right shows the position of the taenite/silicate (S) boundary.

(a)

(b)

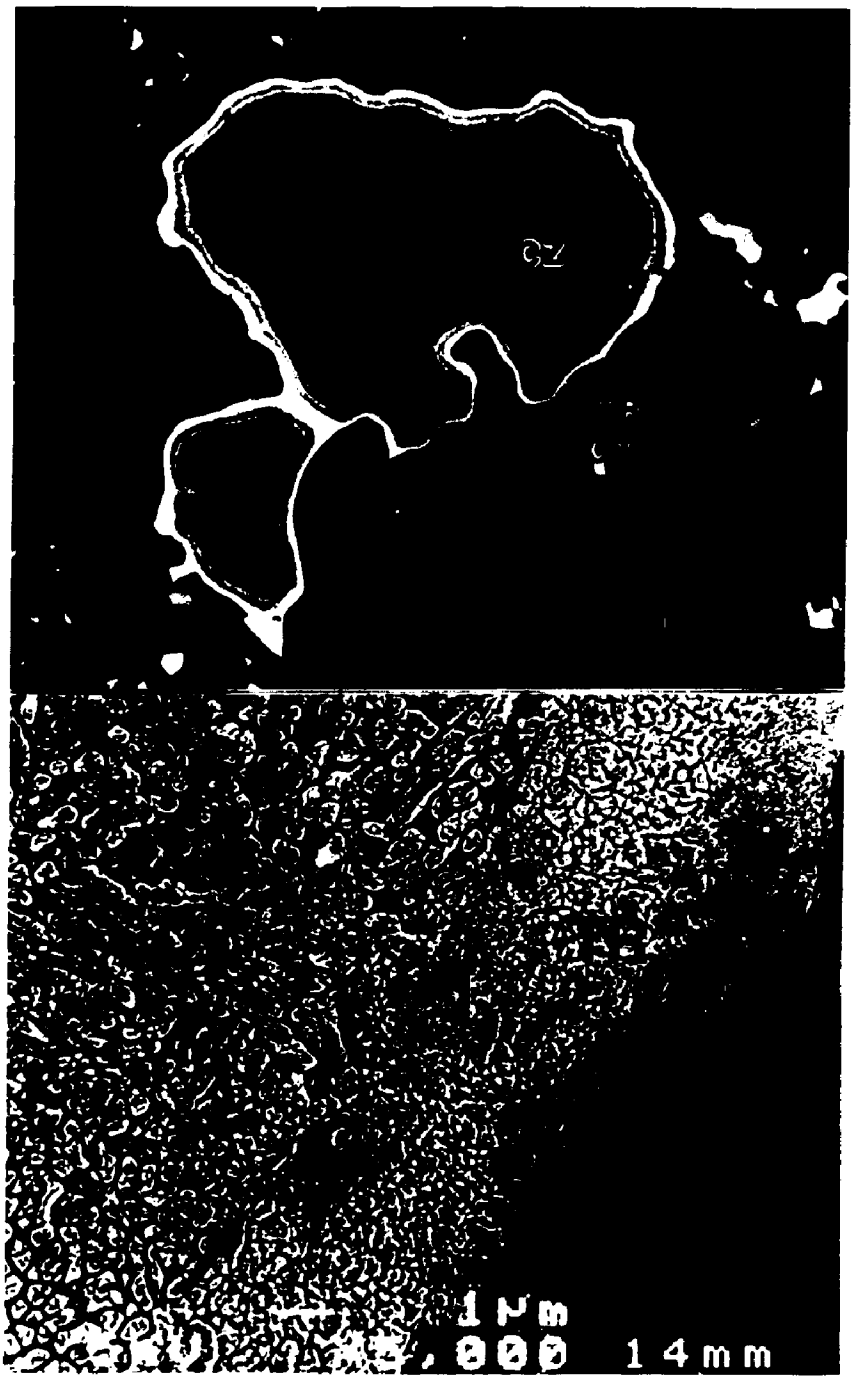

Fig. 4.3 a) a light optical micrograph of retained taenite surrounded by silicate matrix in Patwar mesosiderite. b) a SEM image of the outer taenite rim which shows three sub-zones (1, 2, 3). T: retained taenite, TR: tetrataenite, CZ: cloudy zone, S: silicate matrix.

(a)

(b)

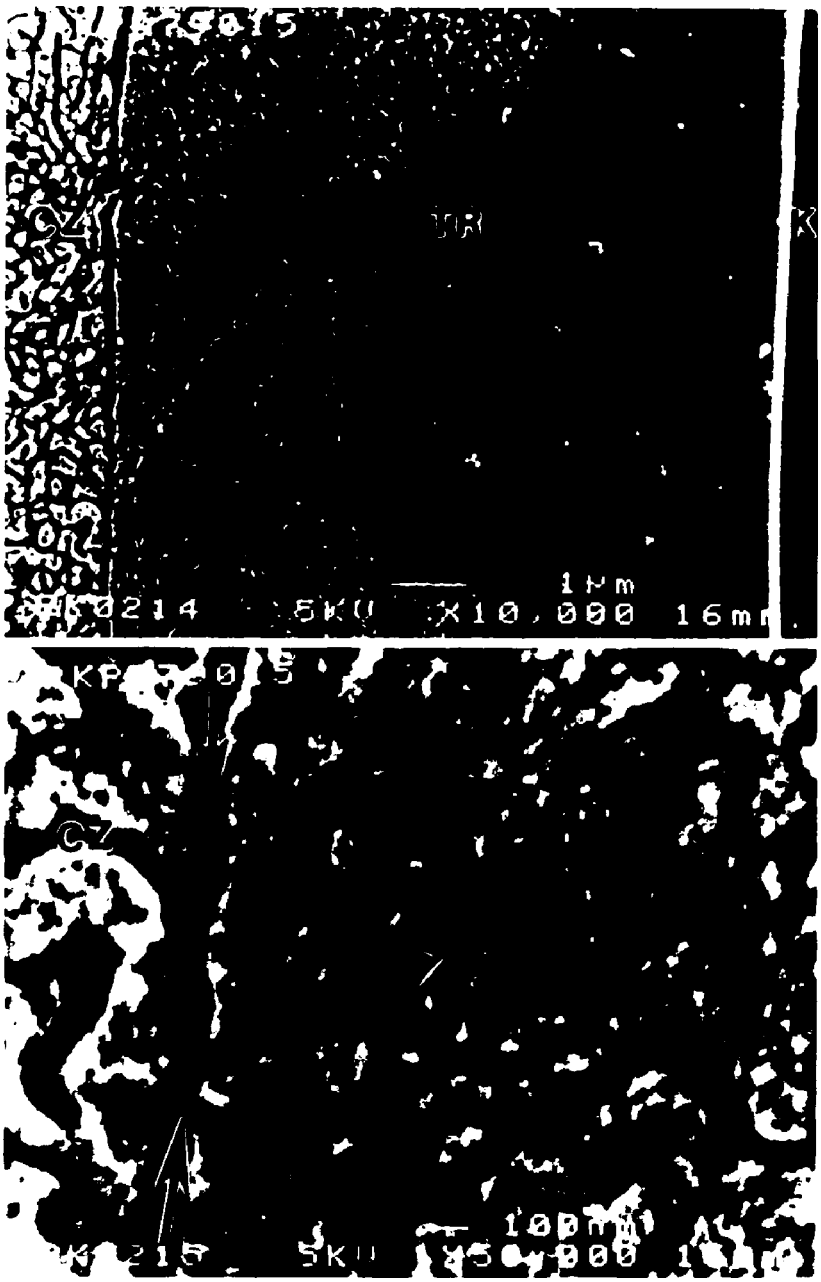

Fig. 4.4 The SEM images of the outer taenite rim of the RKPA79015 mesosiderite. a) an image of the cloudy zone (CZ), the outer taenite rim (TR) containing three sub-zones(1, 2, and 3), and kamacite (K). b), c) and d) are high magnification images of three sub-zones; zone 1, zone 2 and zone 3, respectively.

(c)

(d)

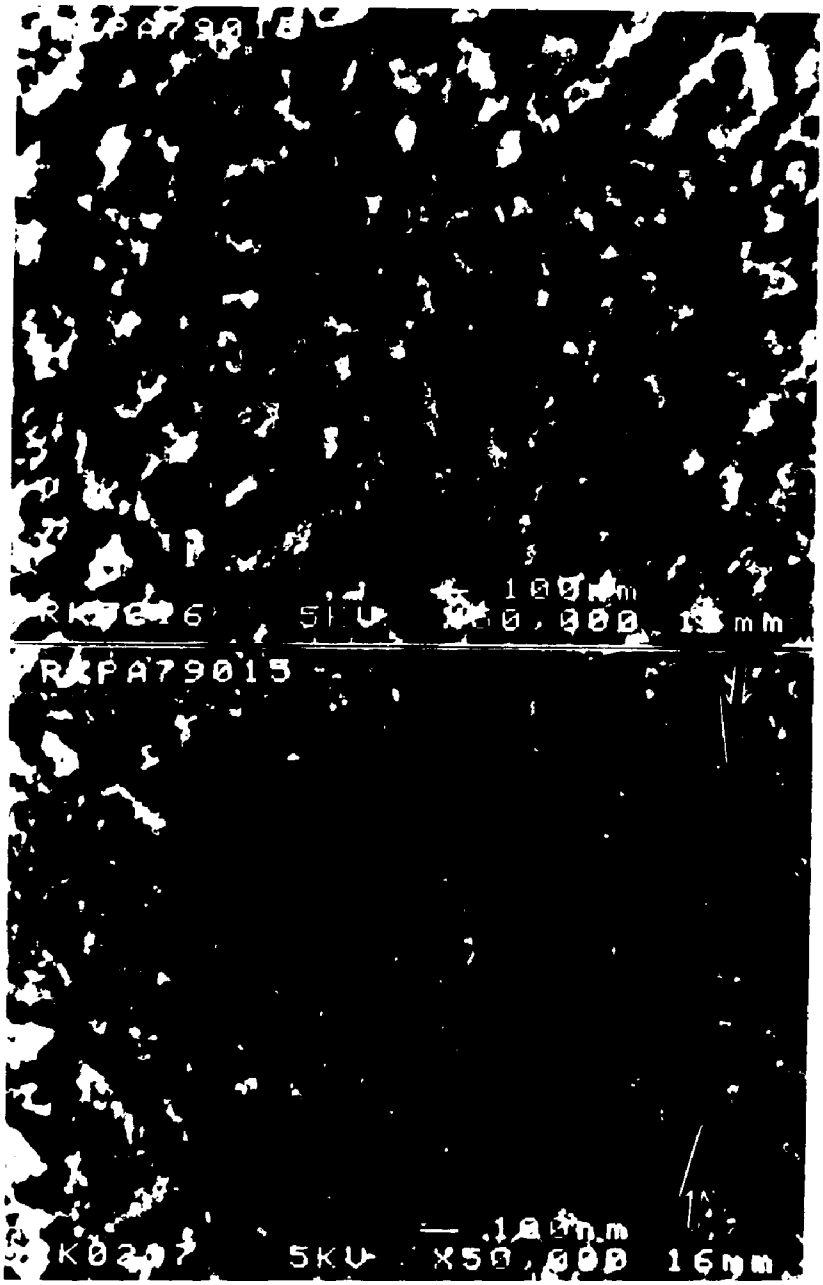

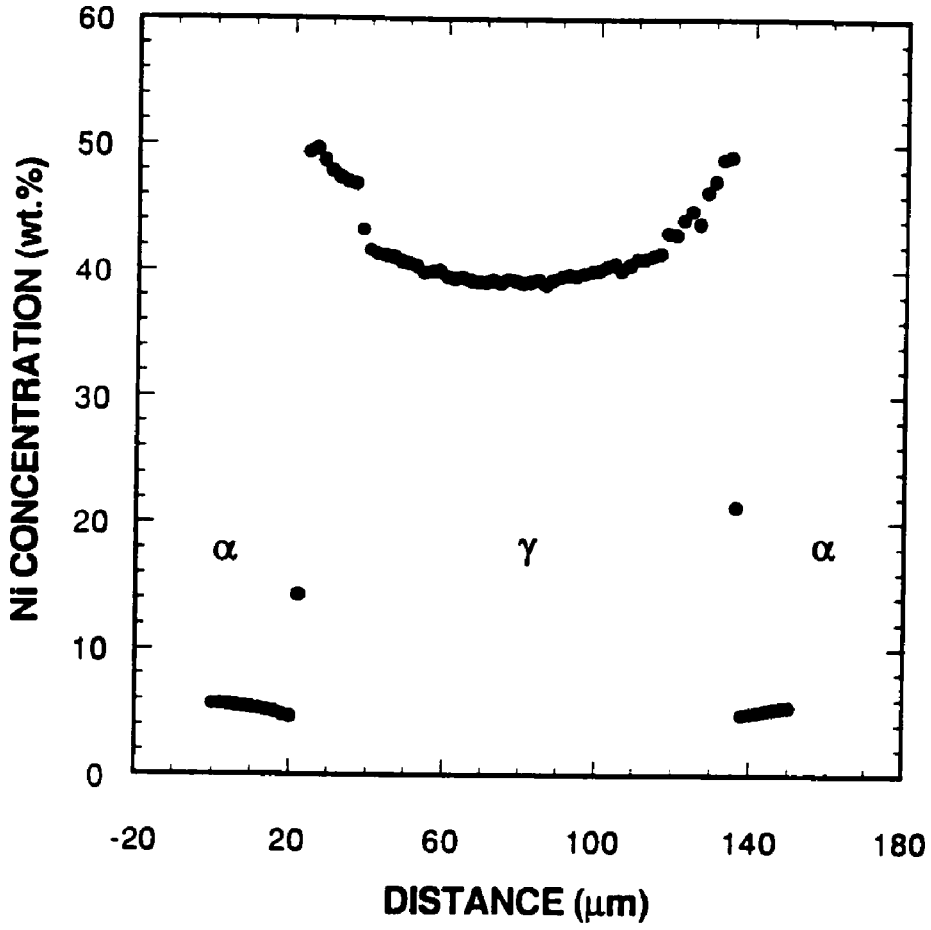

Fig. 4.5 Ni concentration profile obtained with EPMA traversing kamacite, TR and CZ in the RKPA 79015 mesosiderite showing well known "M" shaped profile. Note the discontinuity in the Ni content at the TR/CZ boundary.

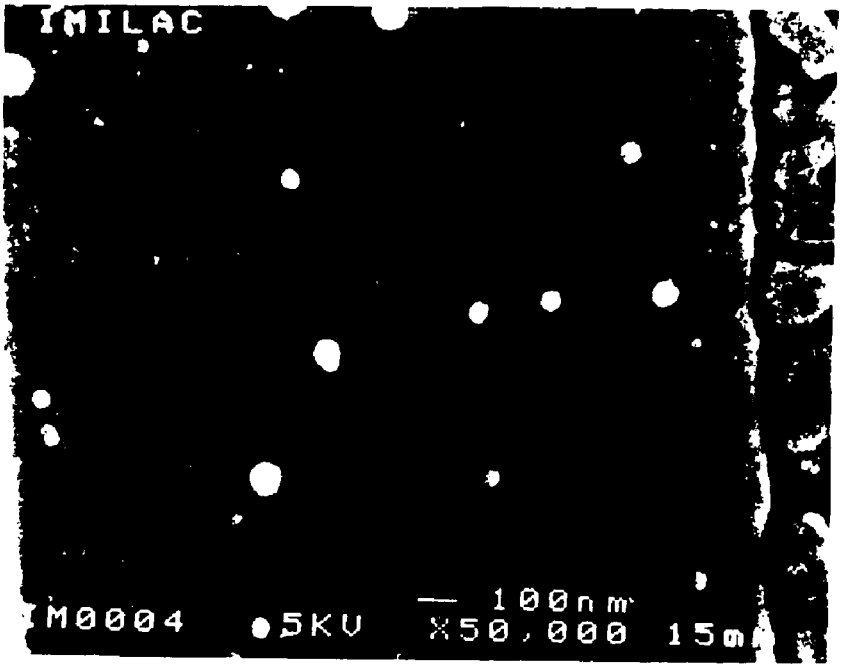

Fig. 4.6 A SEM image of the tetrataenite rim in the Imilac pallasite.

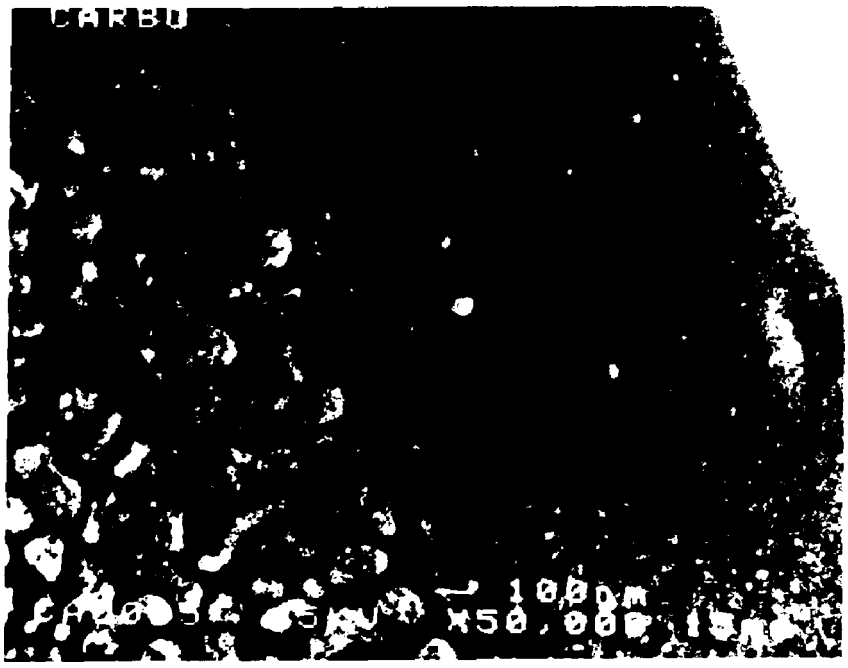

Fig. 4.7 A SEM image of the tetrataenite rim in the Carbo (IID) iron meteorite.

(a)

(b)

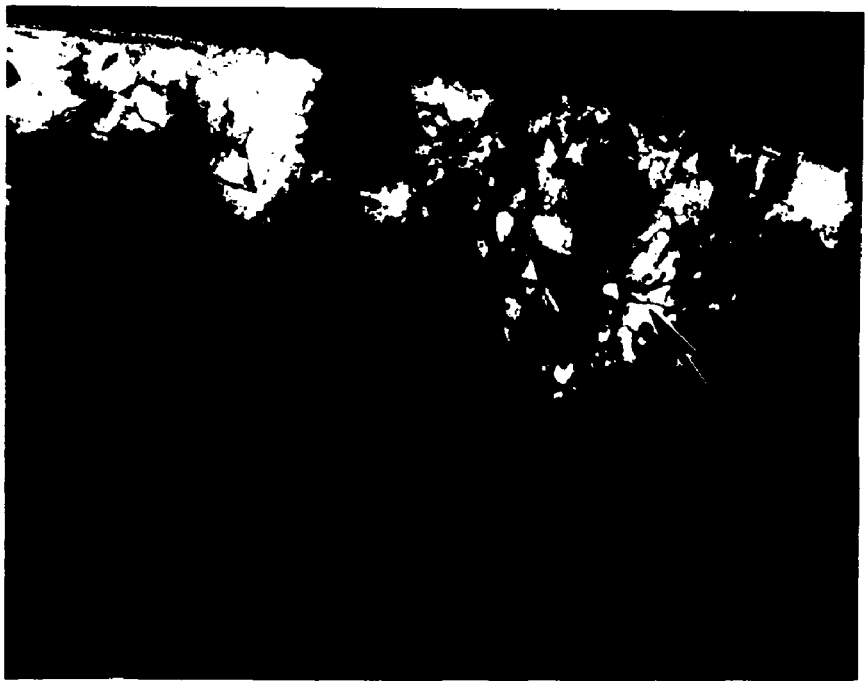

Fig. 4.8 A series of TEM images of the tetrataenite rim of taenite in the RKPA 79015 mesosiderite. a) BF image, b) CDF image using the (010) superlattice reflection, c) SADP showing a $[100]_{fcc}$ zone axis pattern with three variants of the $L1_0$ ordered superlattice reflections, and d) indexing of the SADP.

(c)

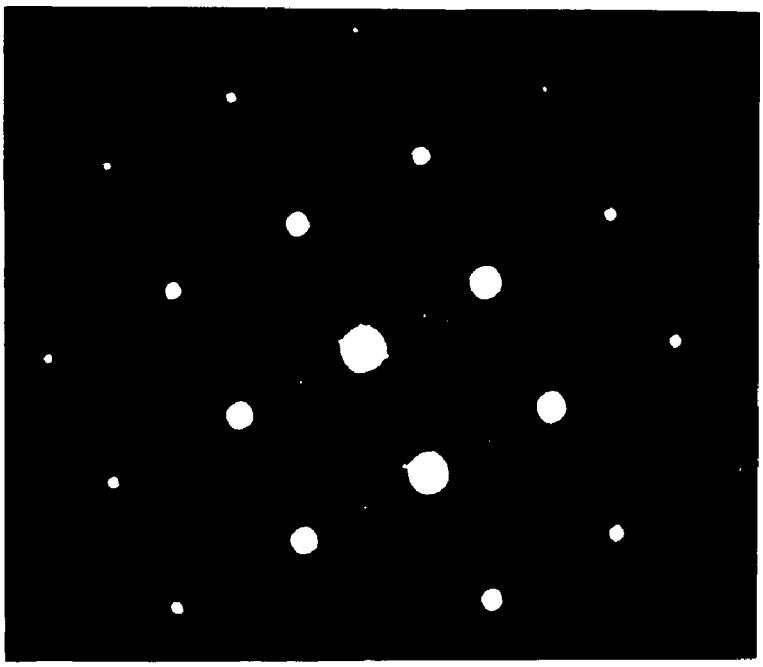

(d)

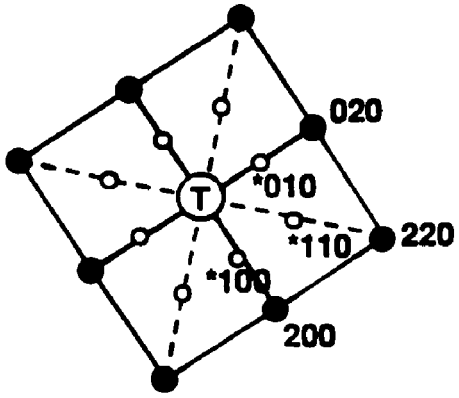

● fcc [100] zone axis
o superlattice reflections

(a)

(b)

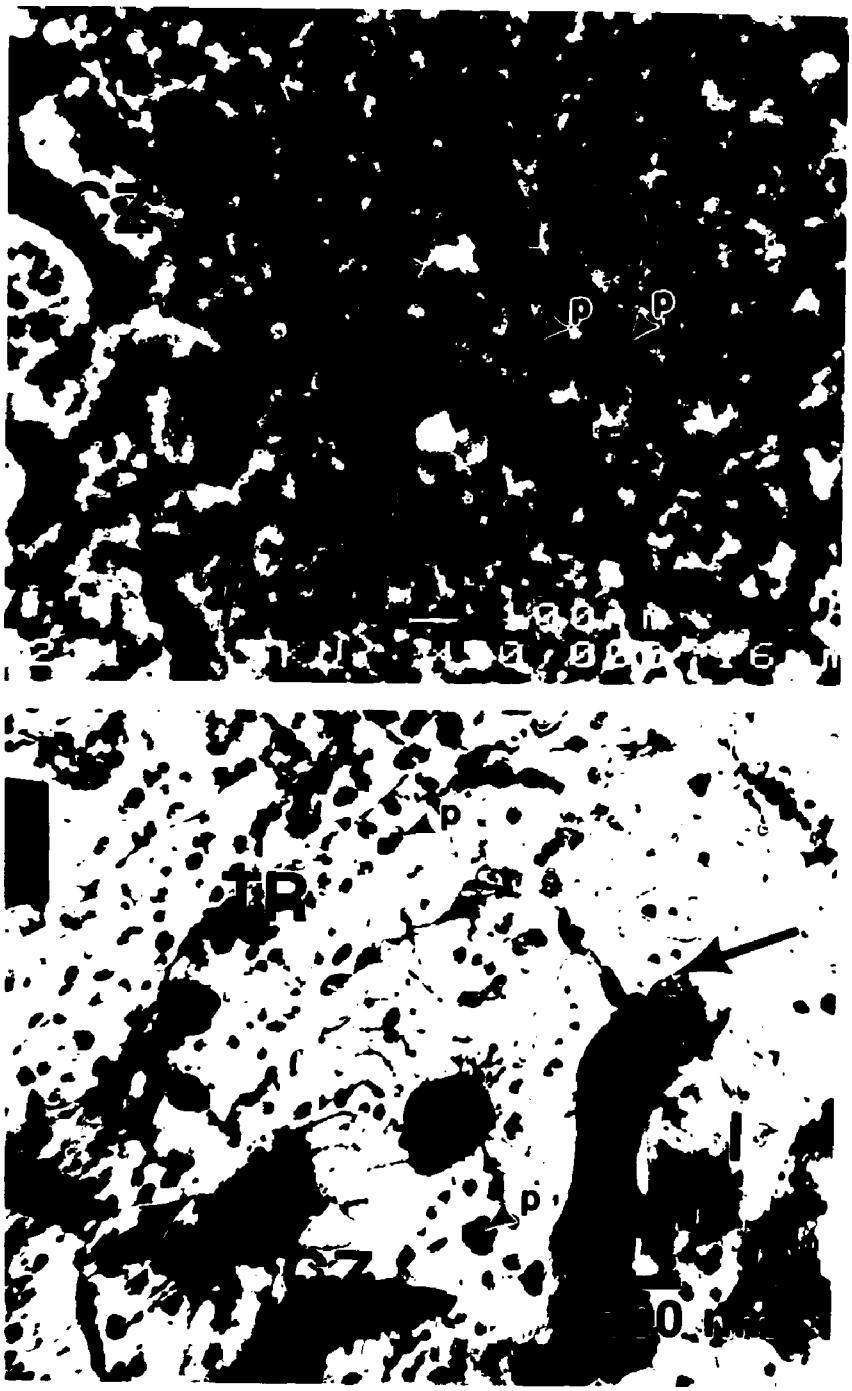

Fig. 4.9 A set of images from the tetrataenite rim and the cloudy zone of the RKPA 79015 mesosiderite at the boundary between the two structures. a) SEM image showing the etch pits b) TEM bright field image showing precipitates which correspond to the etch pits in a).

(a)

(b)

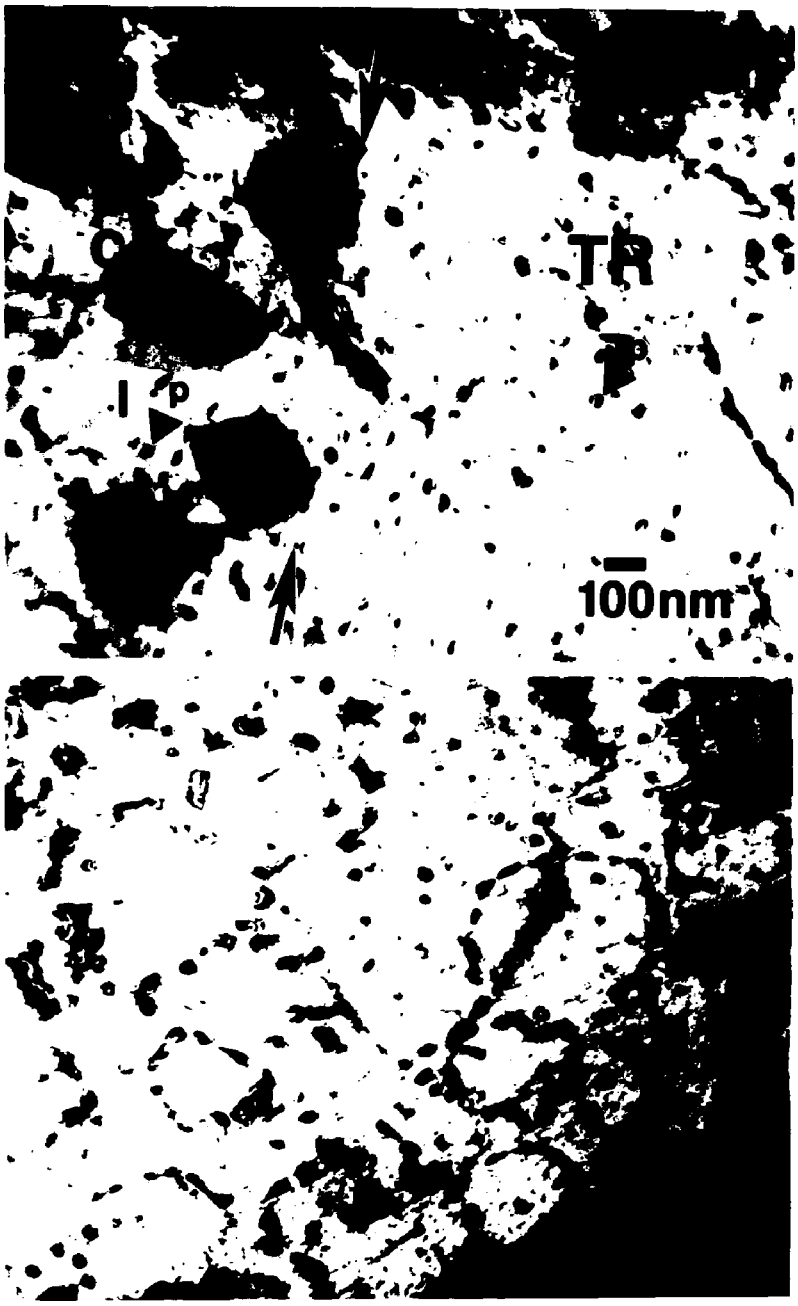

Fig. 4.10 A set of TEM bright field images of the RKPA79015 mesosiderite. a) BF image of the tetrataenite rim and the cloudy zone at the boundary between the two structures. b) BF image showing the precipitate loop and some scattered precipitates at the center of the tetrataenite rim (zone 2). c) CBED pattern from a precipitate in the TR containing a fcc $[100]_\gamma$ matrix pattern with a bcc $[011]_\alpha$ precipitate pattern. d) indexing of the CBED pattern.

(c)

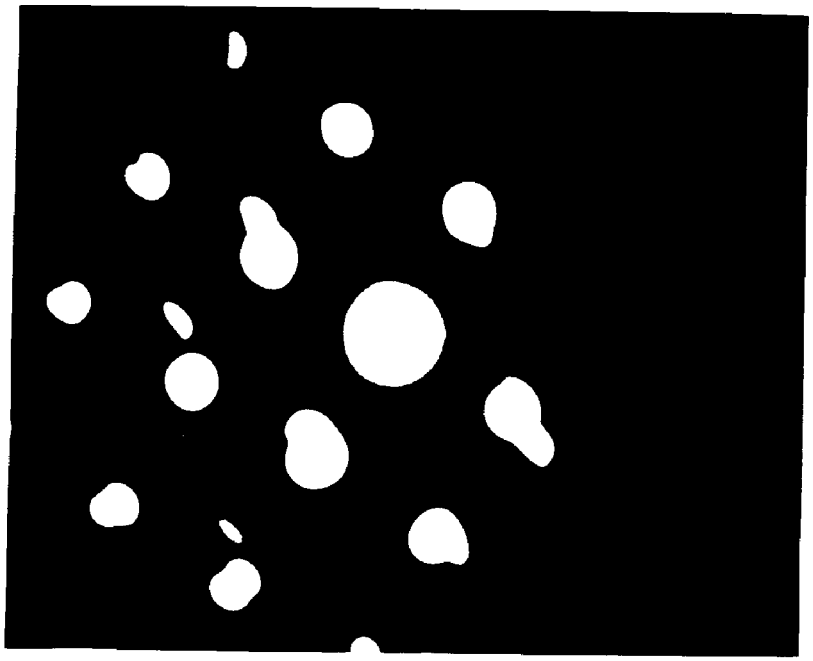

(d)

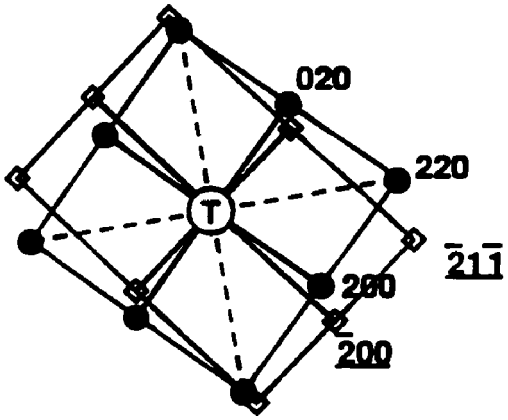

● fcc [100] zone axis

□ bcc [$0\bar{1}\bar{1}$] zone axis

(a)

(b)

Fig. 4.11 A series of TEM images taken at the border between the TR and the CZ. a) BF image, b) CDF image using a $(200)_\alpha$ reflection of bcc $[011]_\alpha$ zone axis pattern, c) CDF image using a (100) superlattice reflection, d) SADP, e) schematic diagram of the SADP, f) indexing of the $[100]_\gamma$ fcc matrix pattern and superlattice reflections, and the $[100]_\alpha$ bcc zone axis pattern, and g) indexing of the $[011]_\alpha$ bcc zone axis pattern.

(c)

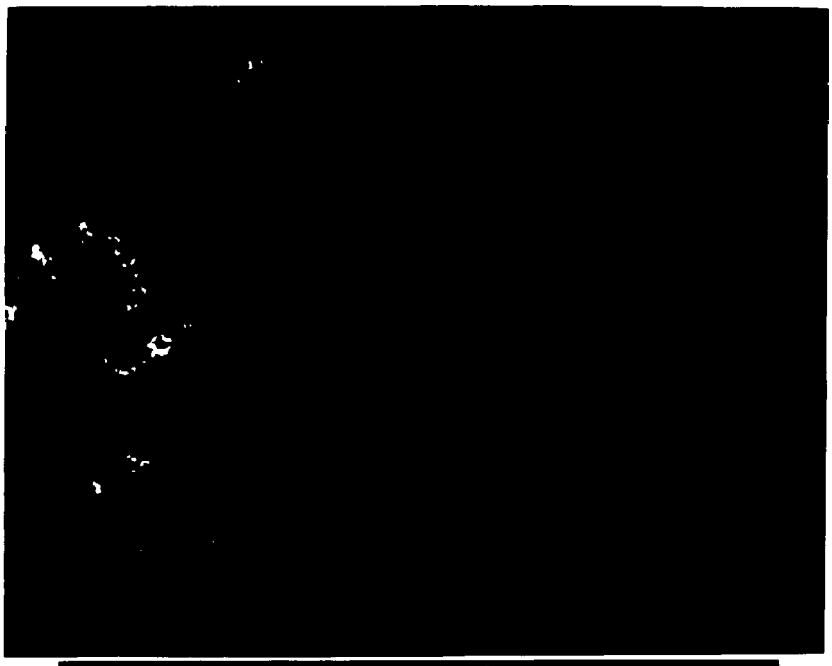

(d)

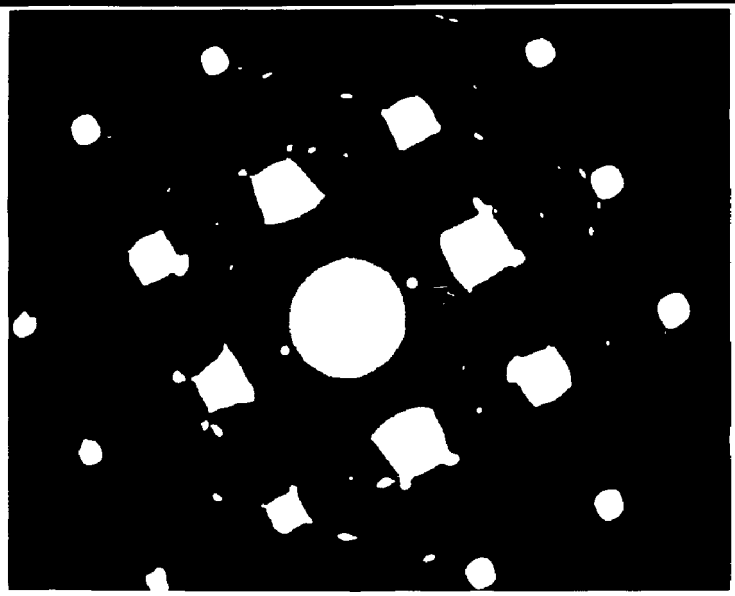

(e)

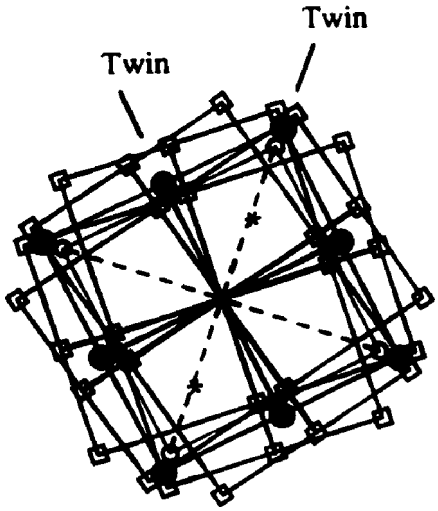

(f)

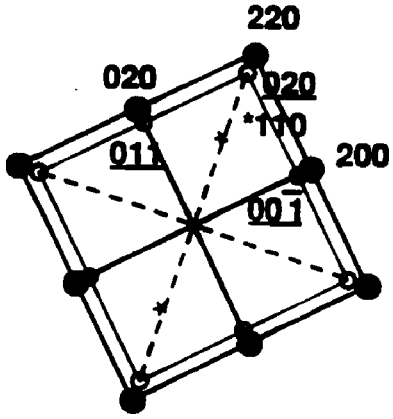

● fcc [100] zone axis
○ bcc [100] zone axis
★ superlattice reflections

(g)

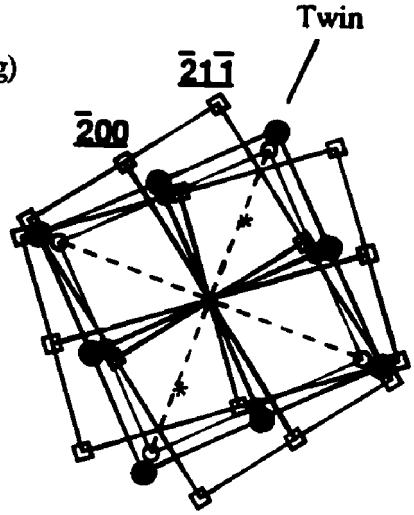

□ bcc [011] zone axis

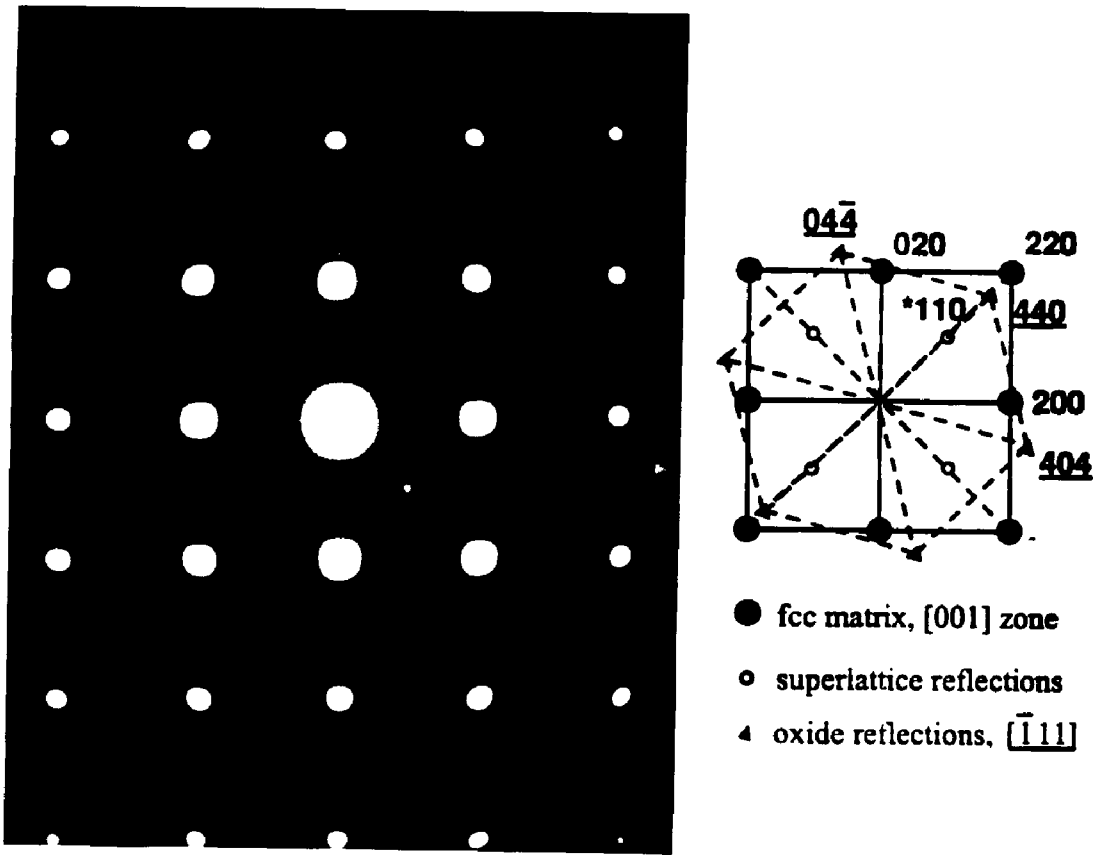

Fig. 4.12 a) Convergent beam micro-diffraction pattern of the tetrataenite matrix in the outer taenite rim, b) Indexing of the diffraction pattern containing $[100]_\gamma$ fcc matrix spots with superlattice reflections and $[\bar{1}\,11]$ oxide spots.

(a)

(b)

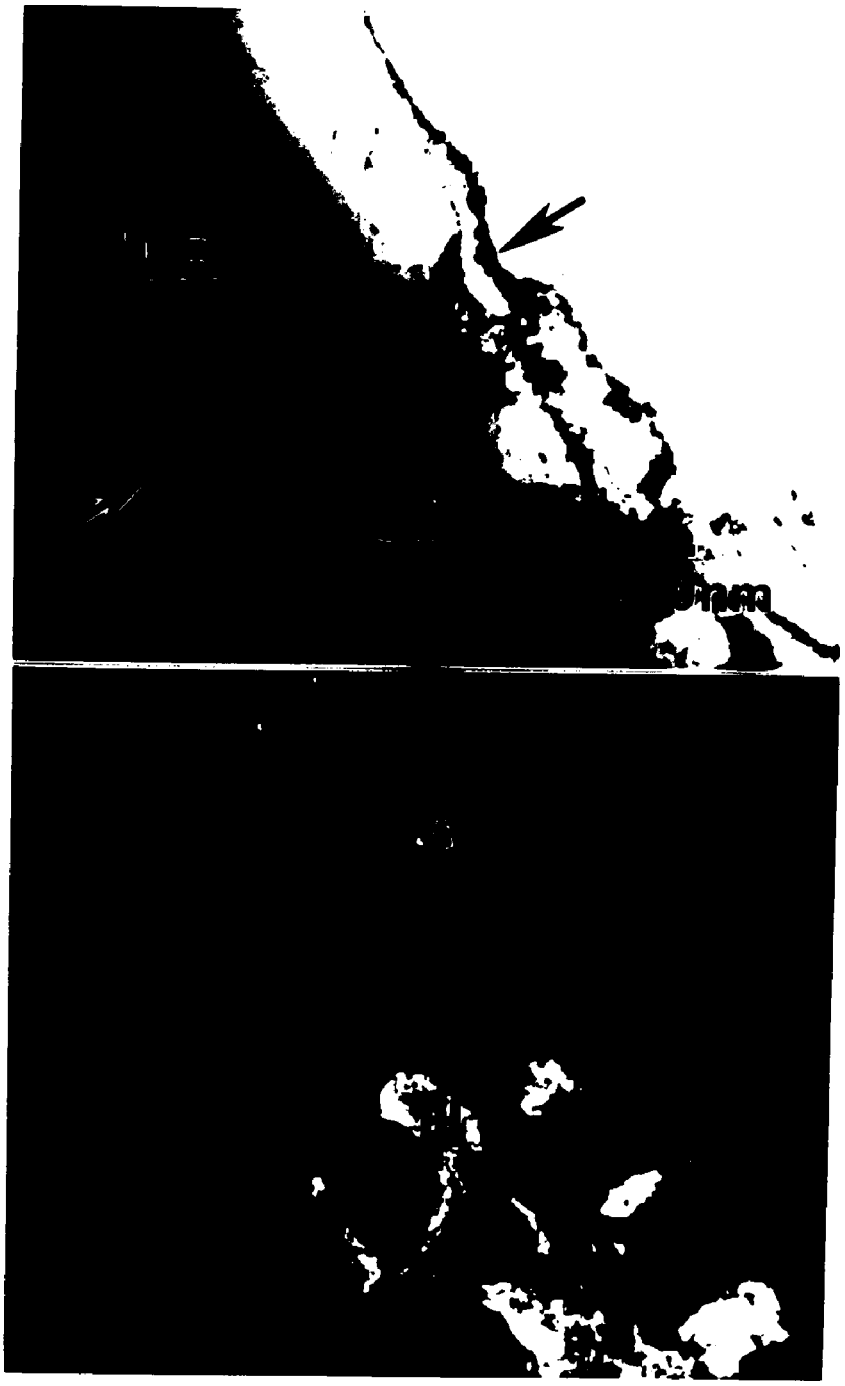

Fig. 4.13 A set of TEM images of the tetrataenite rim and the cloudy zone of the Saint Séverin ordinary chondrite. a) BF image at TR/CZ. The set of arrows indicates TR/CZ boundary, b) CDF image showing the honeycomb phase and precipitates which are illuminated.

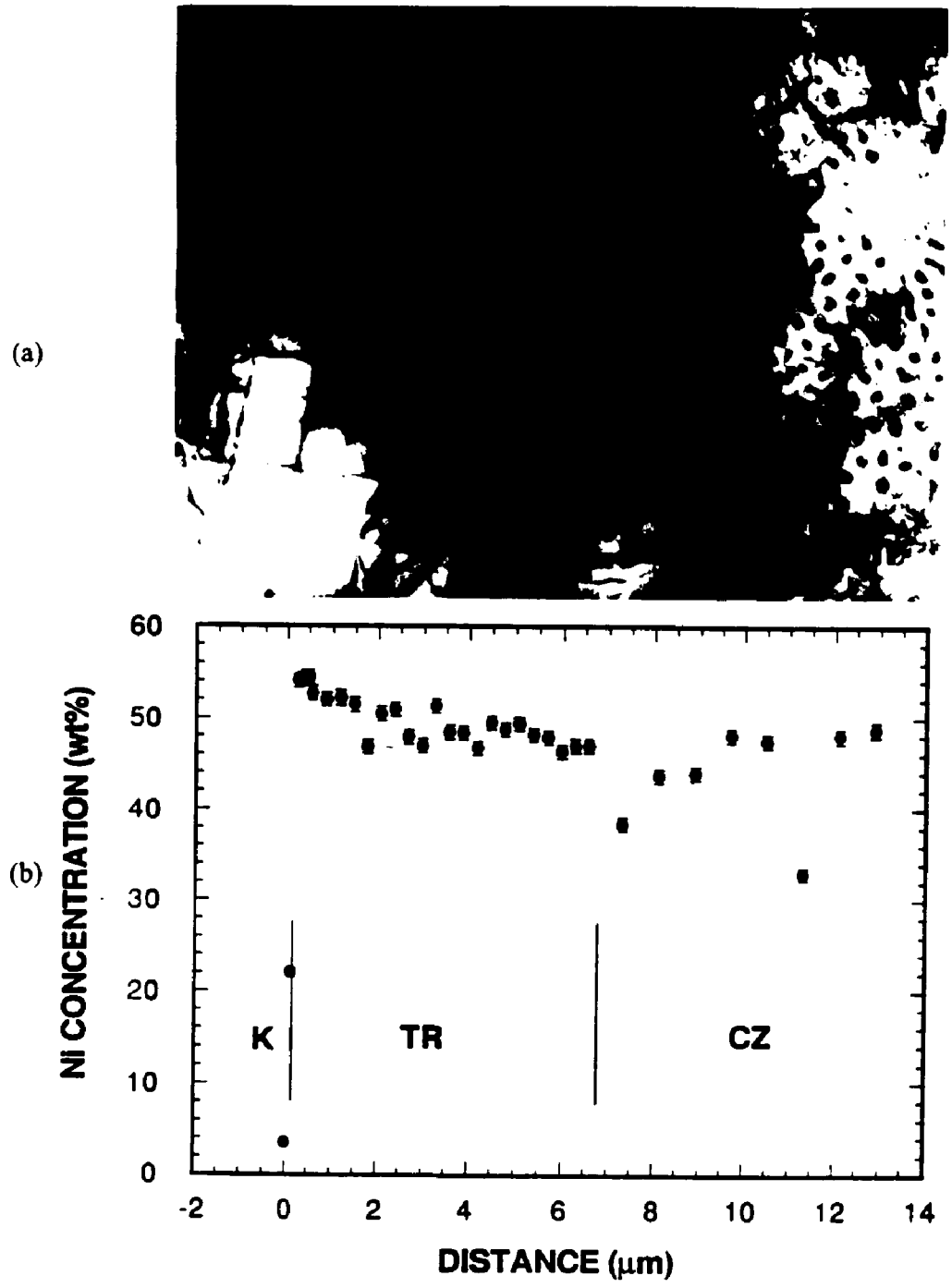

Fig. 4.14 a) a TEM BF image of the RKPA79015 mesosiderite at the boundary between the cloudy zone (CZ) and the tetrataenite rim (TR), b) Ni composition profile across kamacite and taenite.

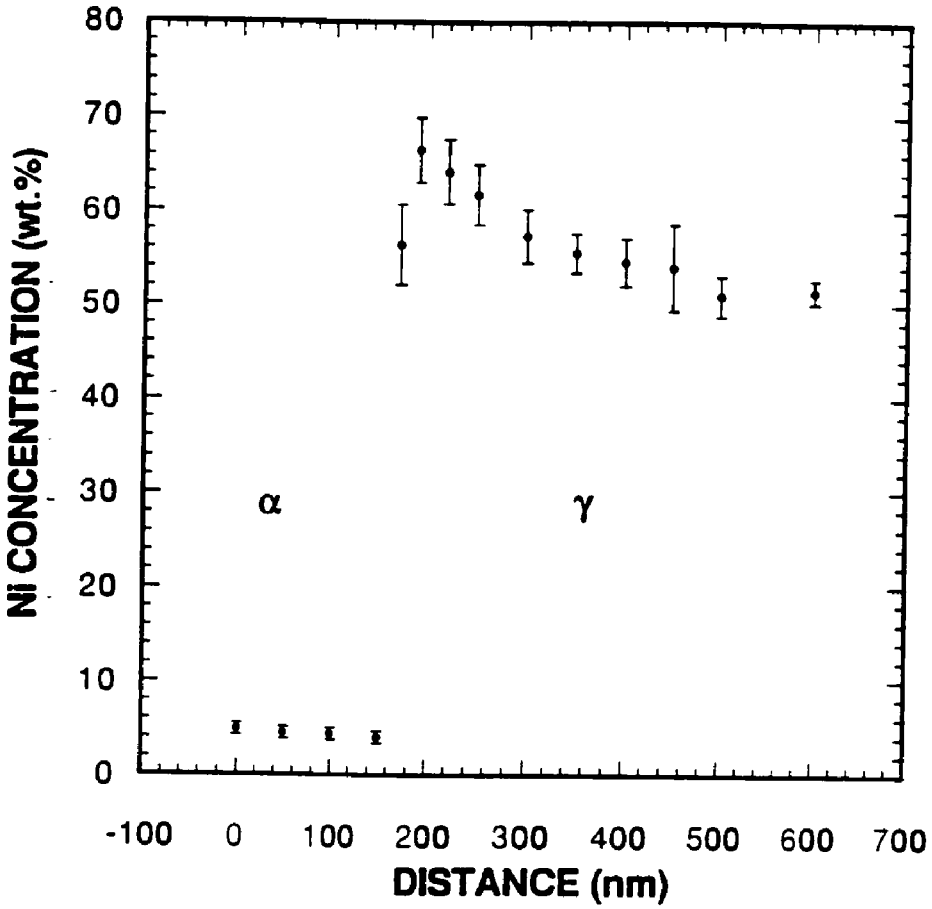

Fig. 4.15 A Ni composition profile across the kamacite/tetrataenite rim interface in the RKPA 79015 mesosiderite obtained with VG HB501 STEM.

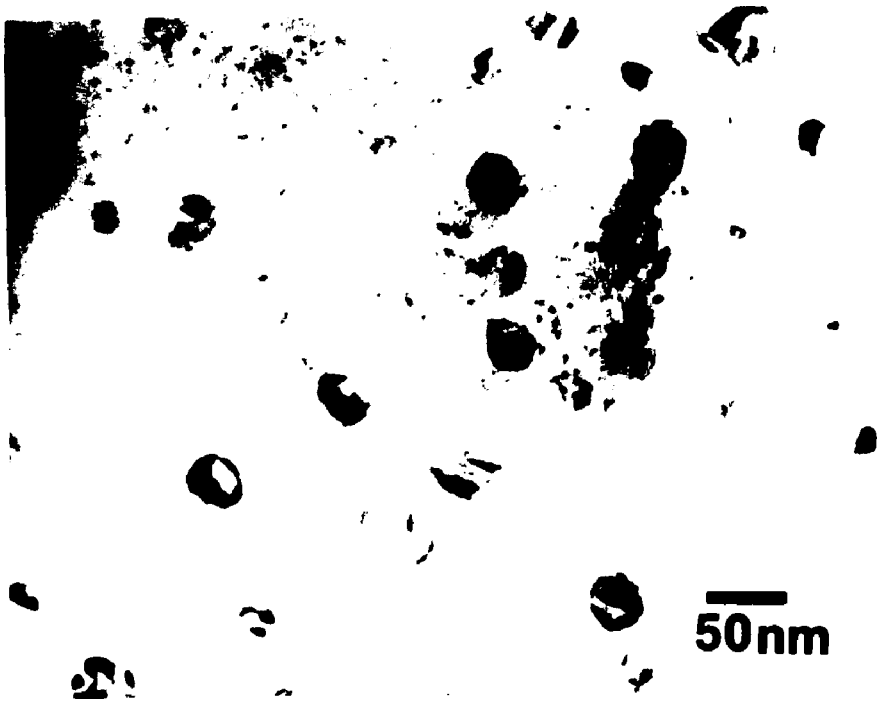

Fig. 4.16 TEM bright field images of the precipitates in the tetrataenite rim region of the mesosiderites: a) Estherville and b) RKPA 79015.

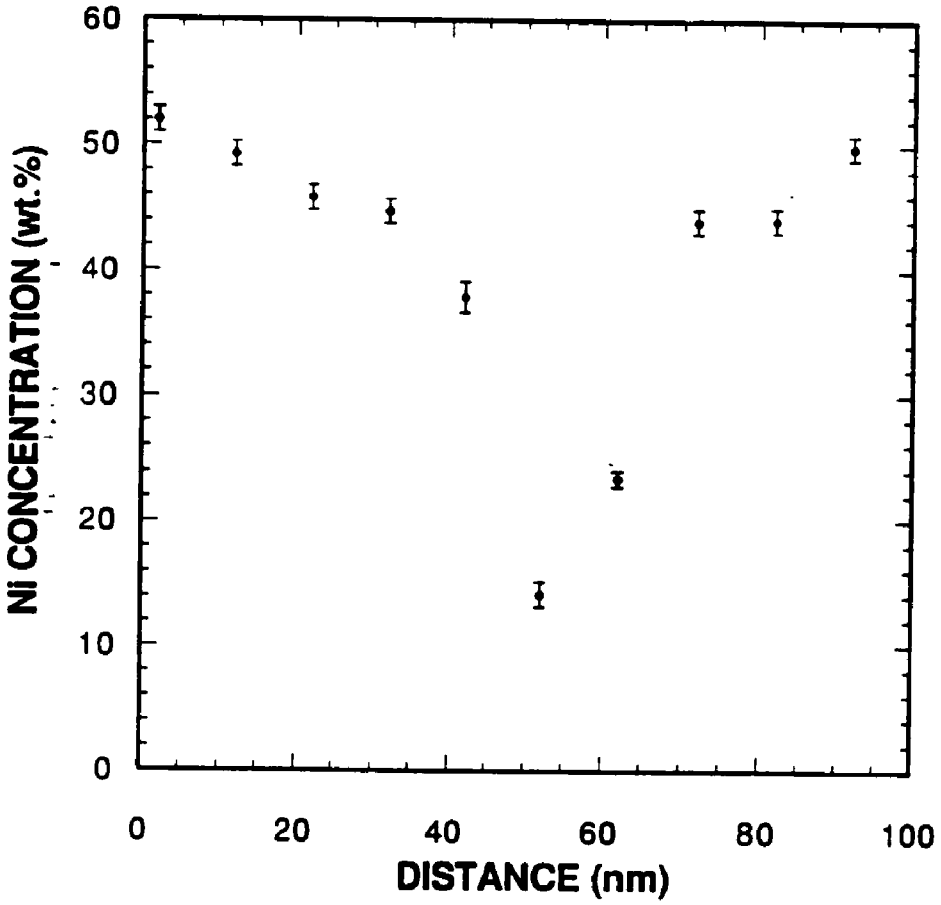

Fig. 4.17 A Ni composition profile across a precipitate in the RKPA 79015 mesosiderite obtained with VG HB501 STEM.

(a)

(b)

Fig. 4.18 SEM images of the cloudy zone of the RKPA79015 mesosiderite. a) substructure is marked with a arrow, b) high magnification image showing details of the substructure. H: honeycomb phase, I: island phase

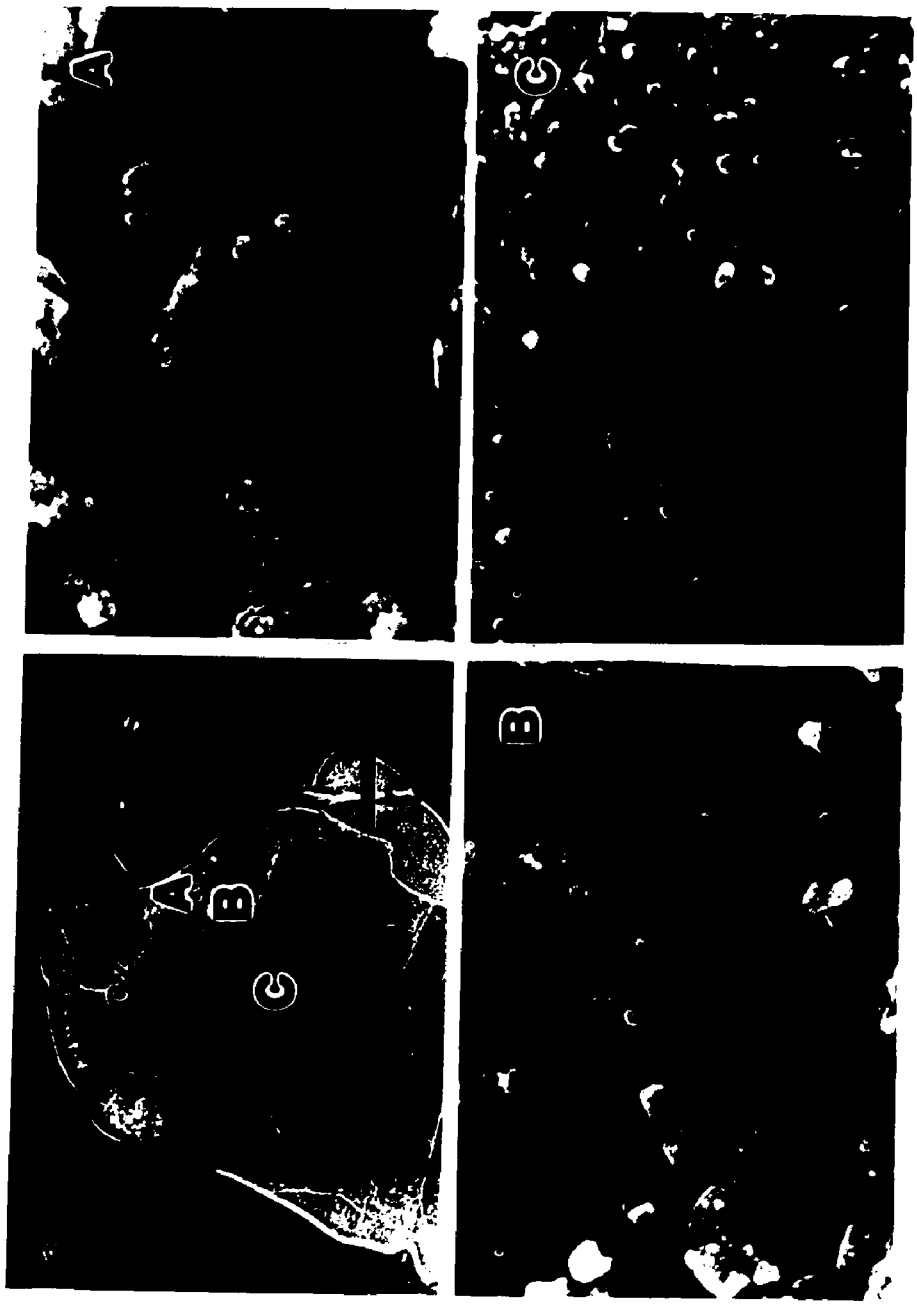

Fig. 4.19 A series of SEM images of a taenite particle in Saint Séverin (LL6) chondrite showing the size variation of the island phase in the cloudy zone. b), c) and d) are high magnification images of regions A, B, and C labeled in a), respectively.

(a)

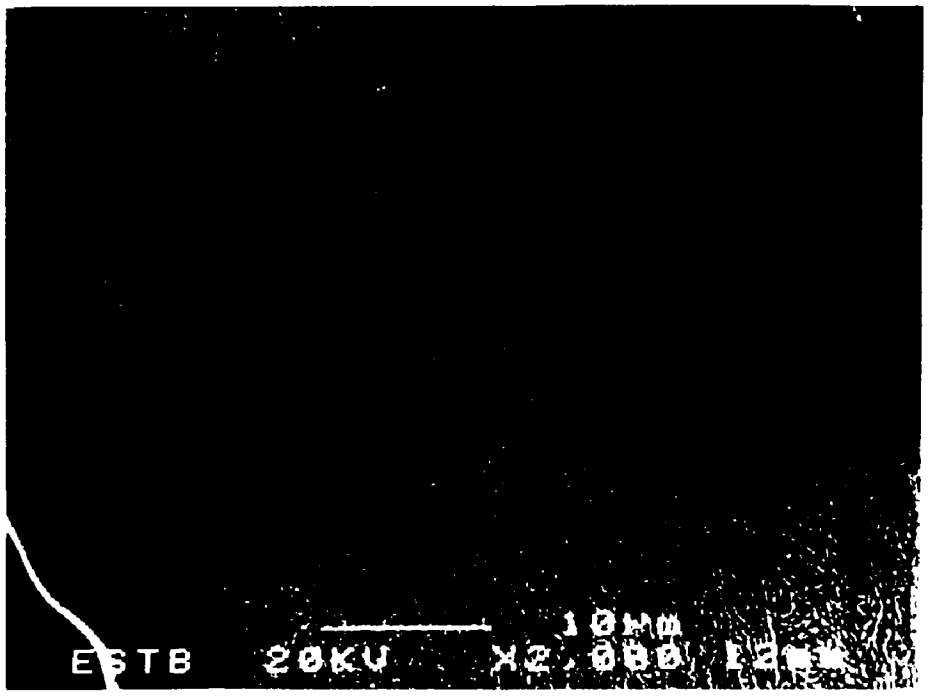

(b)

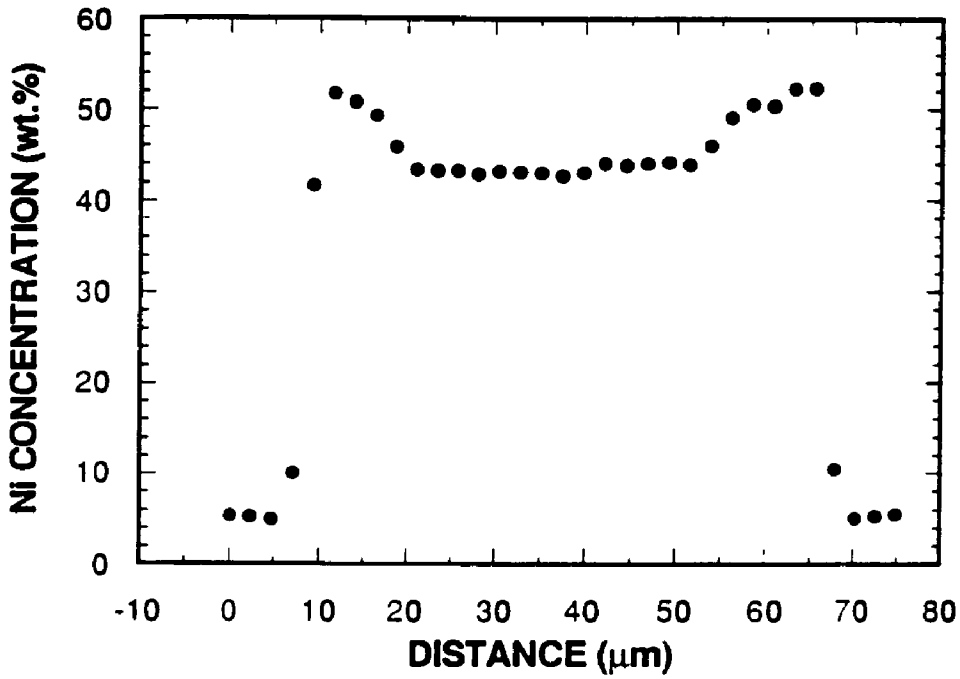

Fig. 4.20 a) a SEM image of the Estherville mesosiderite showing the microstructure of a retained taenite. b) a Ni concentration profile obtained by EPMA traversing kamacite and retained taenite.

(a)

(b)

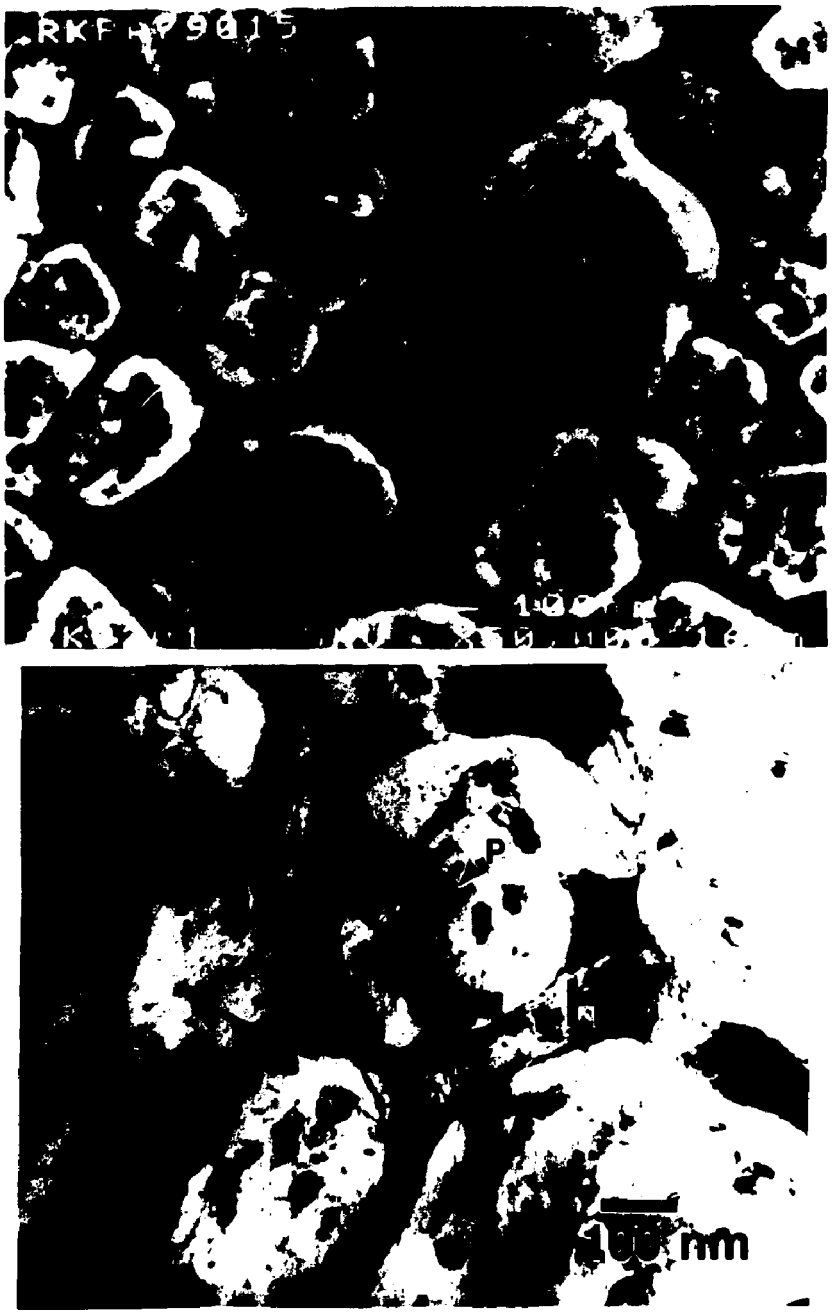

Fig. 4.21 A set of images of the cloudy zone in the RKPA 79015 mesosiderite. a) SEM image showing the etch pits (marked with arrows) as well as honeycomb phase (H) and island phase (I), b) TEM bright field image showing precipitates which correspond to the etch pits in a).

(a)

(b)

Fig. 4.22 A set of TEM bright field and dark field images of the cloudy zone of the Estherville mesosiderite. a) BF image containing the island phase (I) which is bright, the honeycomb phase (H) which is dark, and the precipitates (P) within the island phase, b) CDF image from a (011) bcc reflection, c) SADP, and d) indexing of the SADP.

(c)

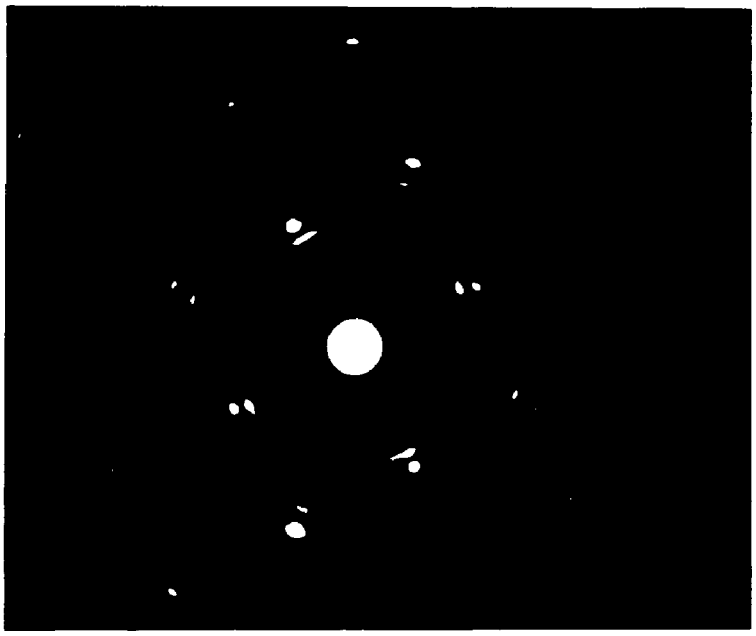

(d)

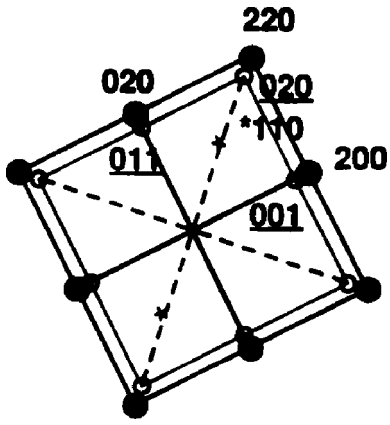

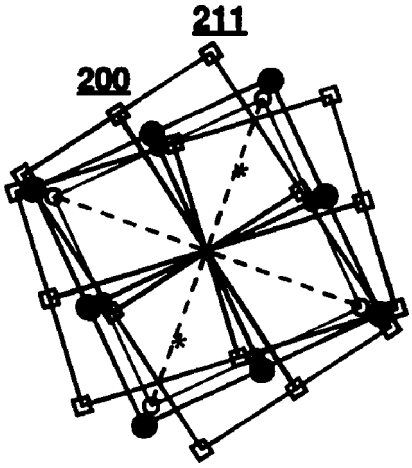

● fcc [100] zone axis
○ bcc [100] zone axis
⋆ superlattice reflections

□ bcc [011] zone axis

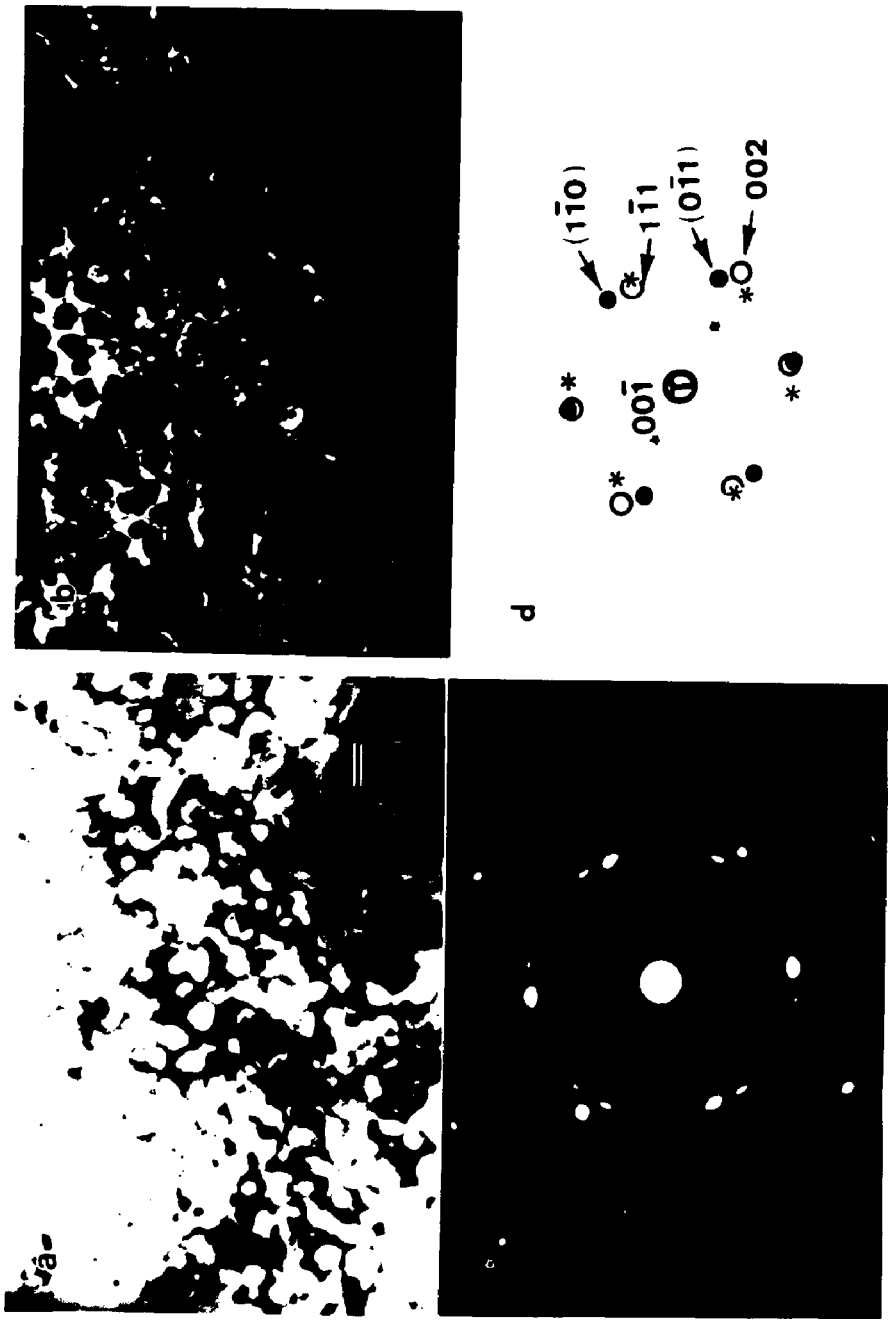

Fig. 4.23 a) TEM bright field image of the CZ region of Saint Séverin chondrite, b) centered dark field image from a (011) bcc spot, c) SAD pattern, d) indexing of SAD pattern; •hkl: bcc[111] zone axis pattern; * hkl: another bcc [111] zone axis pattern; ∘ hkl: fcc[110] zone axis pattern; ⋆ superlattice diffraction spots (observed on the negative).

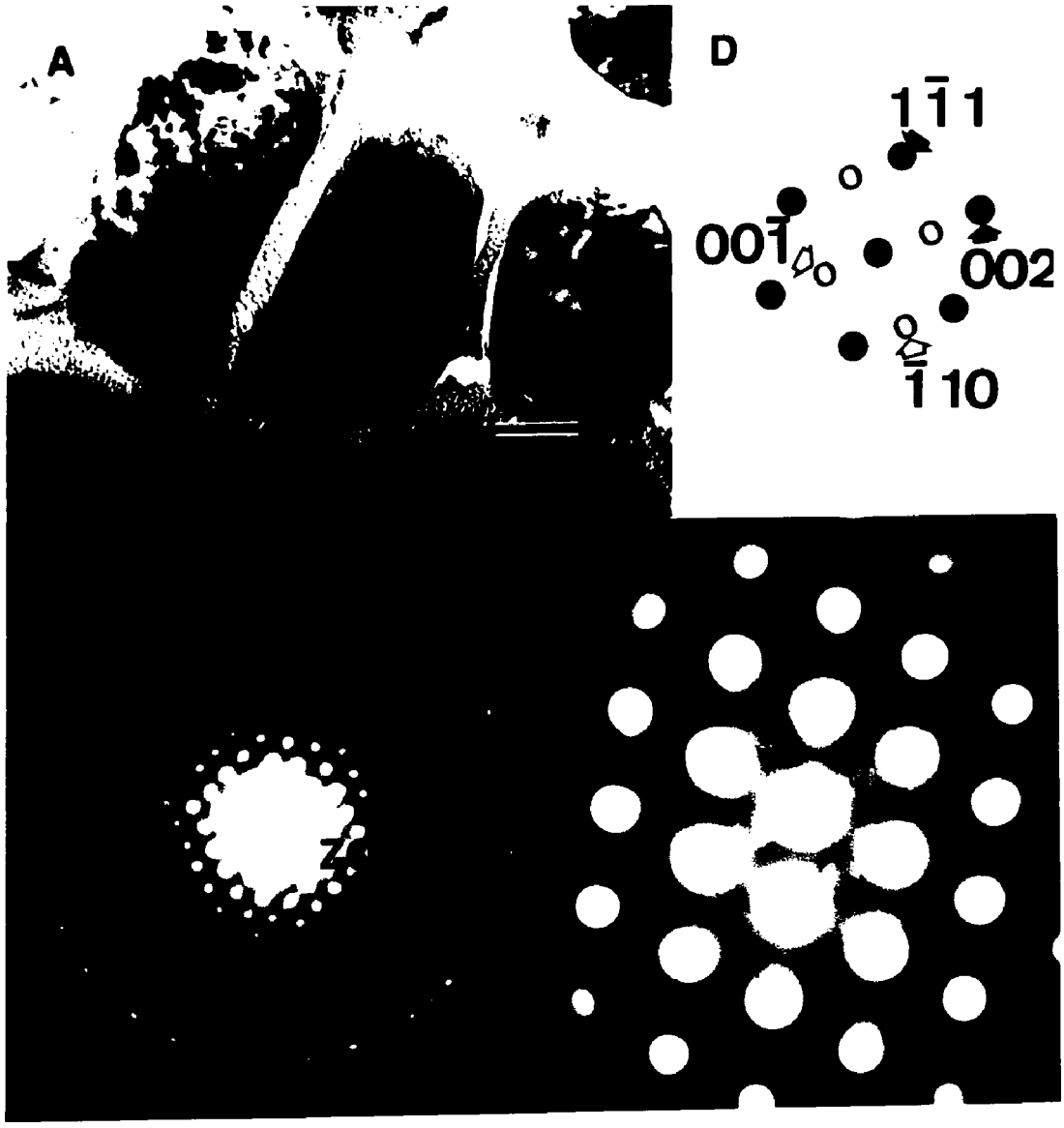

Fig. 4.24 a) a TEM BF image of the cloudy zone in the Saint Séverin chondrite. The island phase is labeled I, b) CBED pattern from the island phase showing a fcc [110] zone axis pattern, c) ZOLZ pattern showing superlattice diffraction spots, and d) indexing of the ZOLZ pattern.

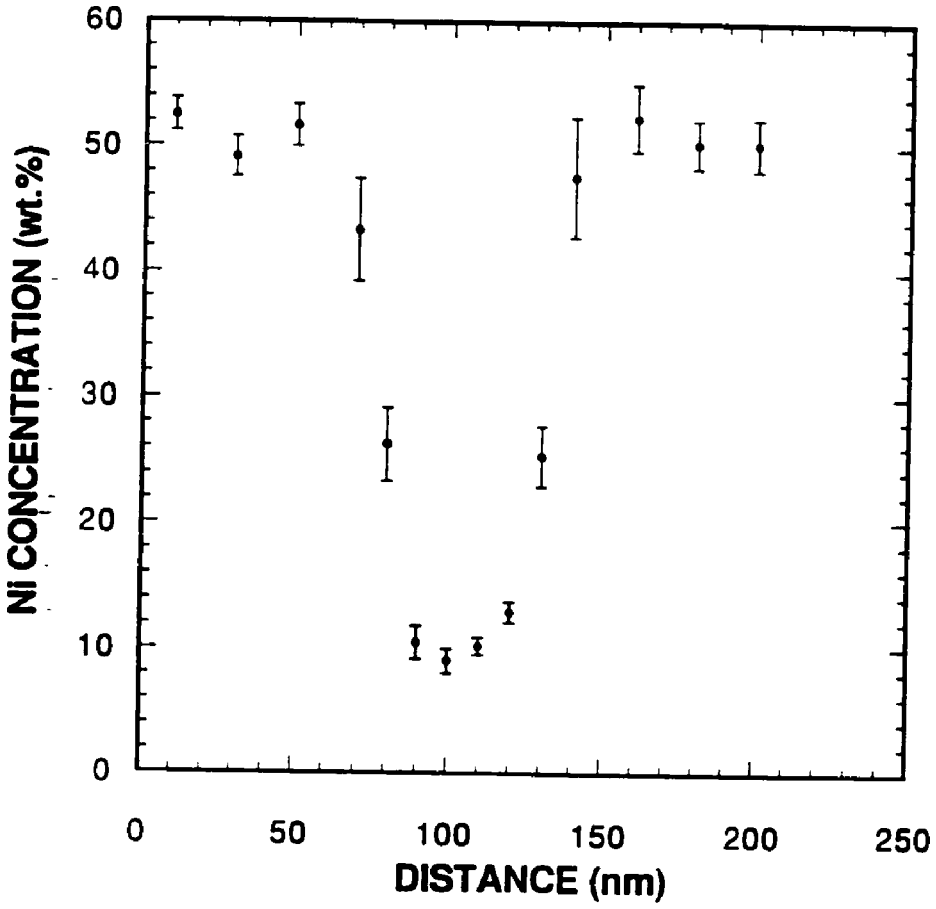

Fig. 4.25 A Ni composition profile across the honeycomb phase and the island phase in the RKPA 79015 mesosiderite obtained with the VG HB501 STEM.

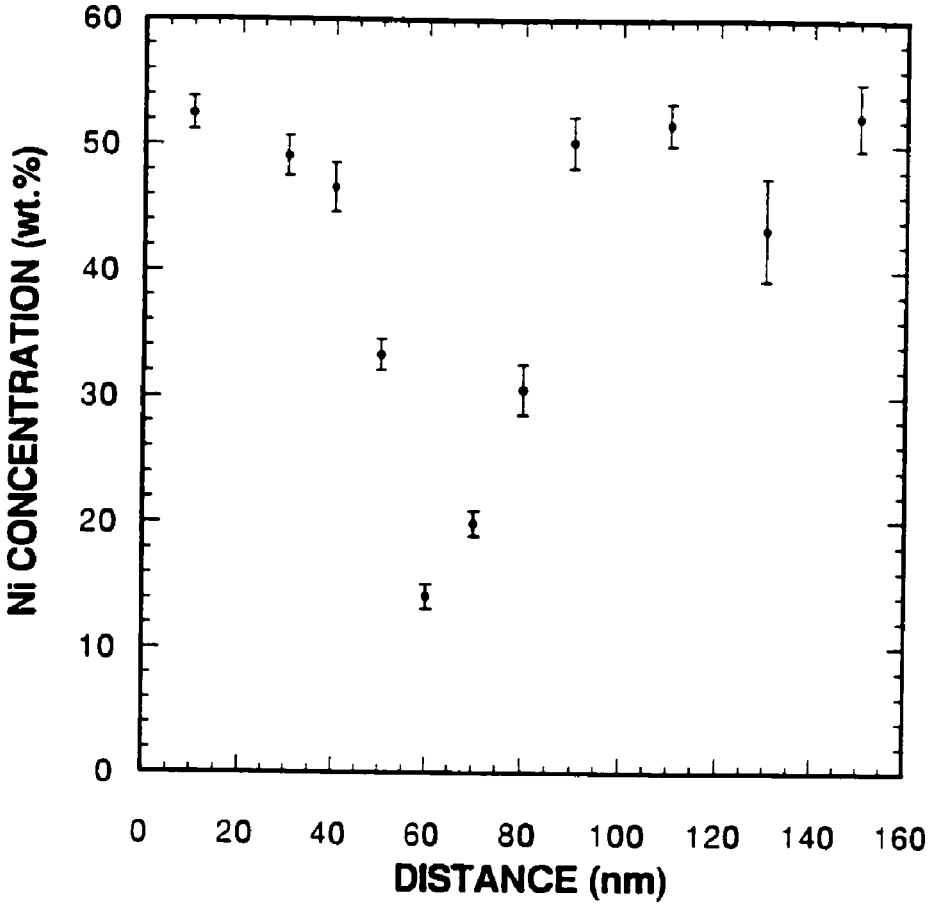

Fig. 4.26 A Ni concentration profile across a precipitate in the RKPA 79015 mesosiderite obtained with the VG HB501 STEM.

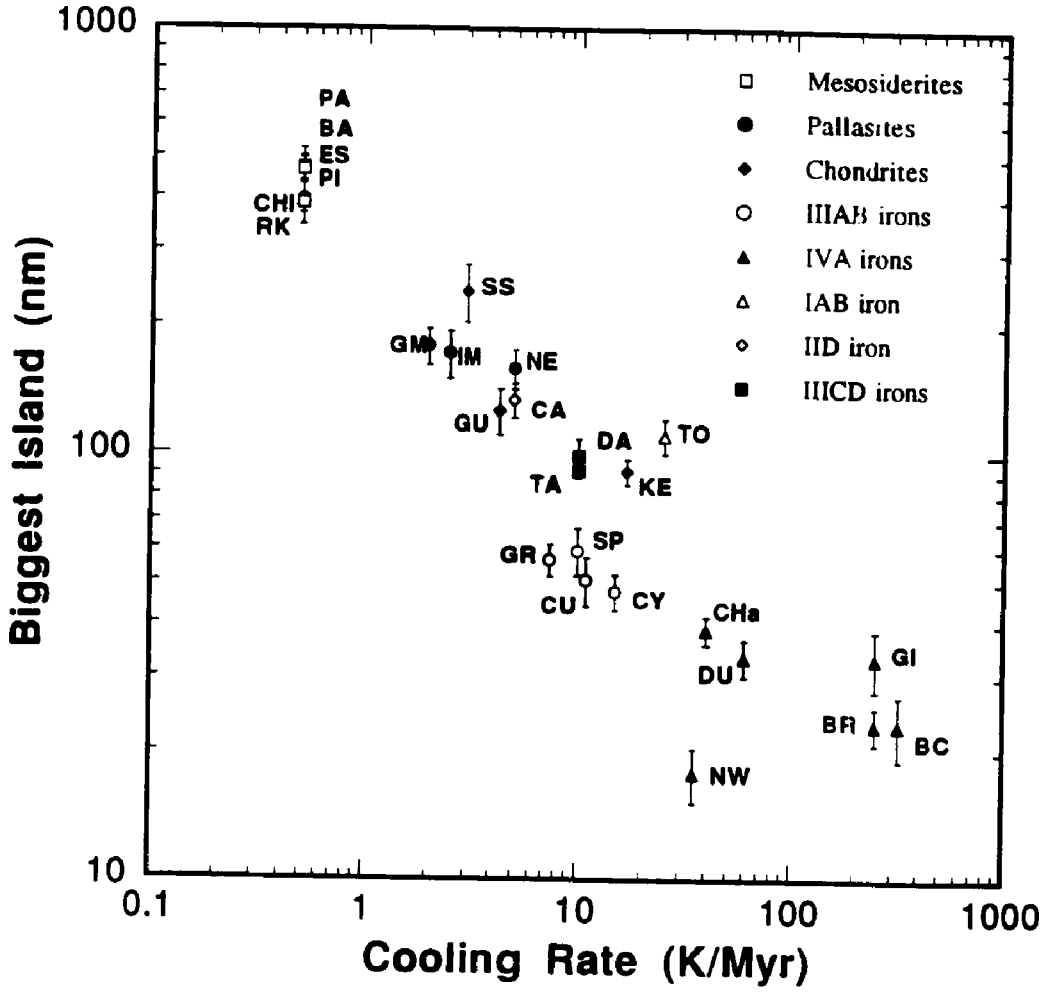

Fig. 4.27 The size variation of the island phase at the outermost region of the cloudy zone versus the cooling rate of meteorites.

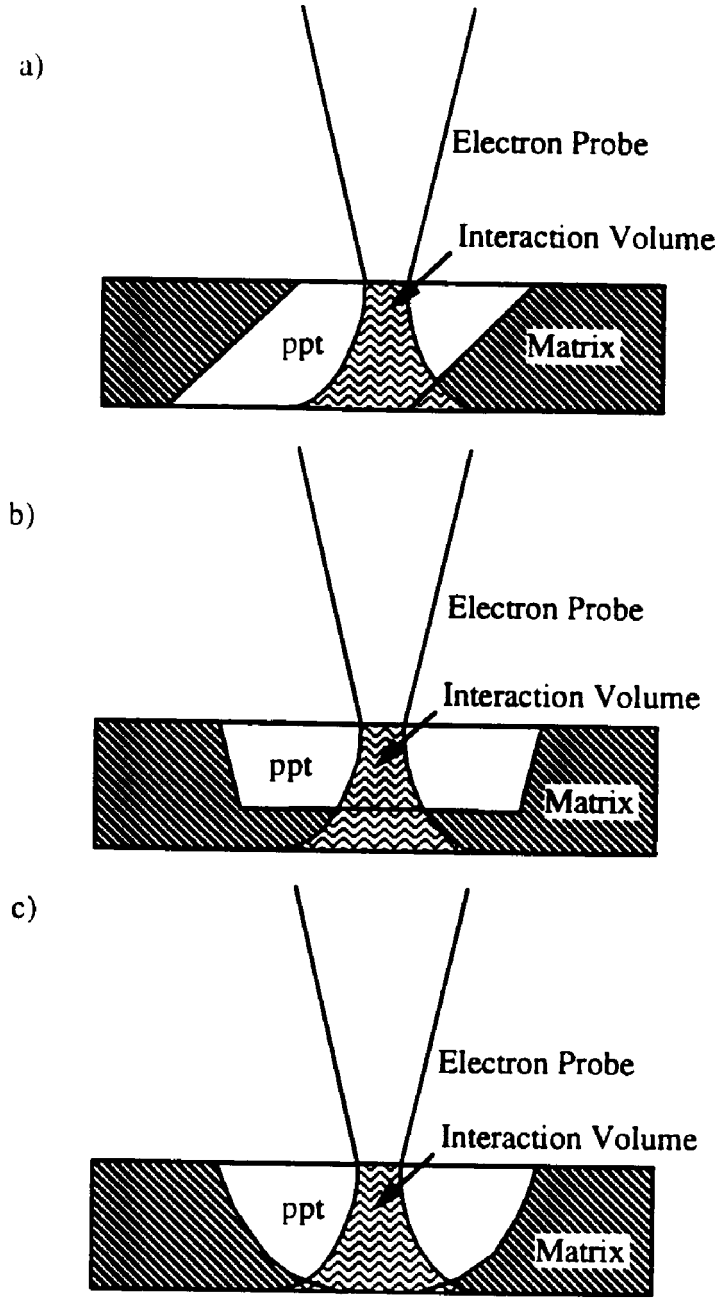

Fig. 5.1 Schematic illustration of the possible situations which can lead to uncertainty in determining the composition. a) the interface and the electron beam are not parallel, b) one phase overlays another completely, and c) one phase overlays another partially.

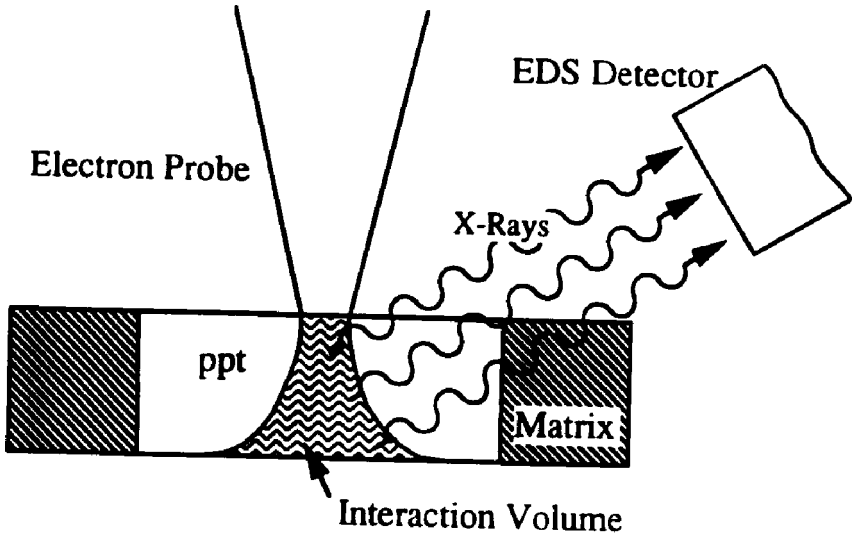

Fig. 5.2 Schematic illustration of the interface not being oriented parallel to the axis of the EDS detector.

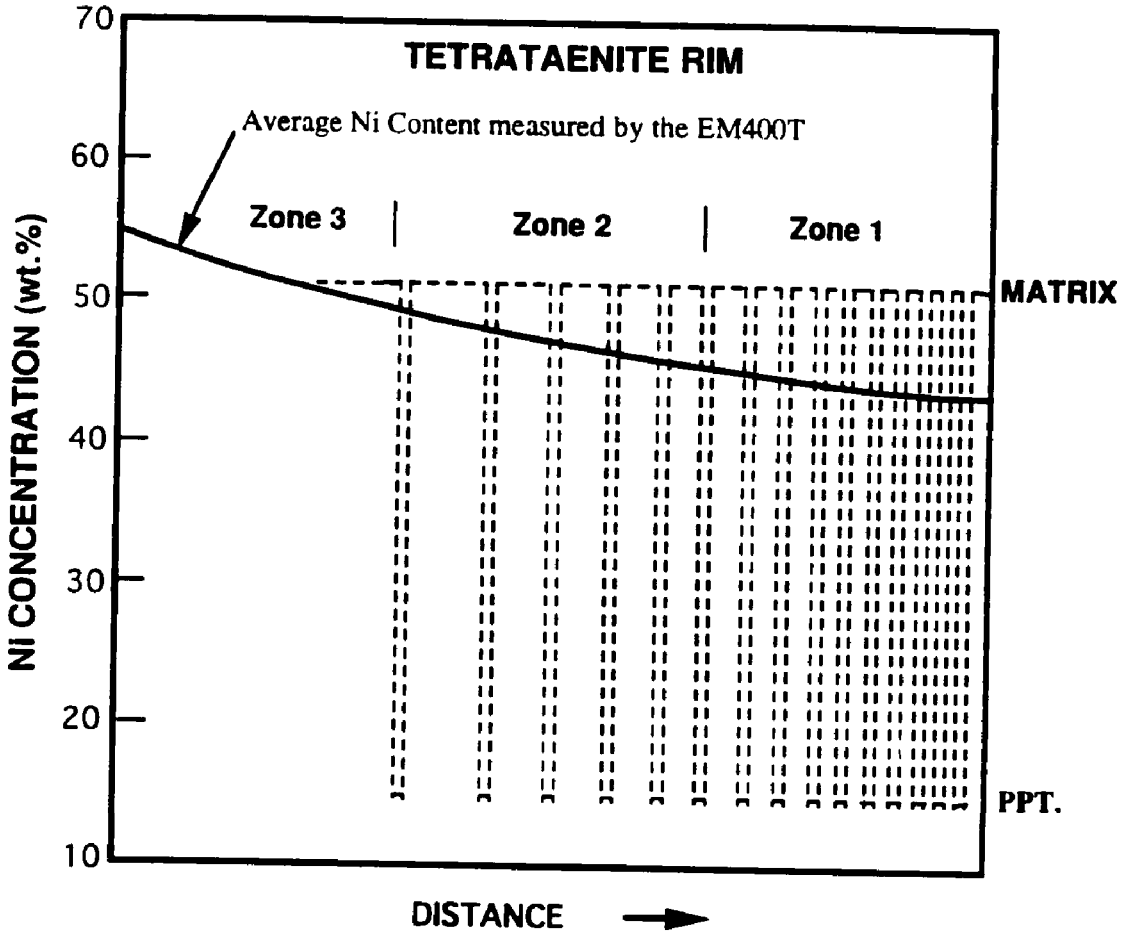

Fig. 5.3 Schematic illustration of the possible Ni composition profile in the TR.

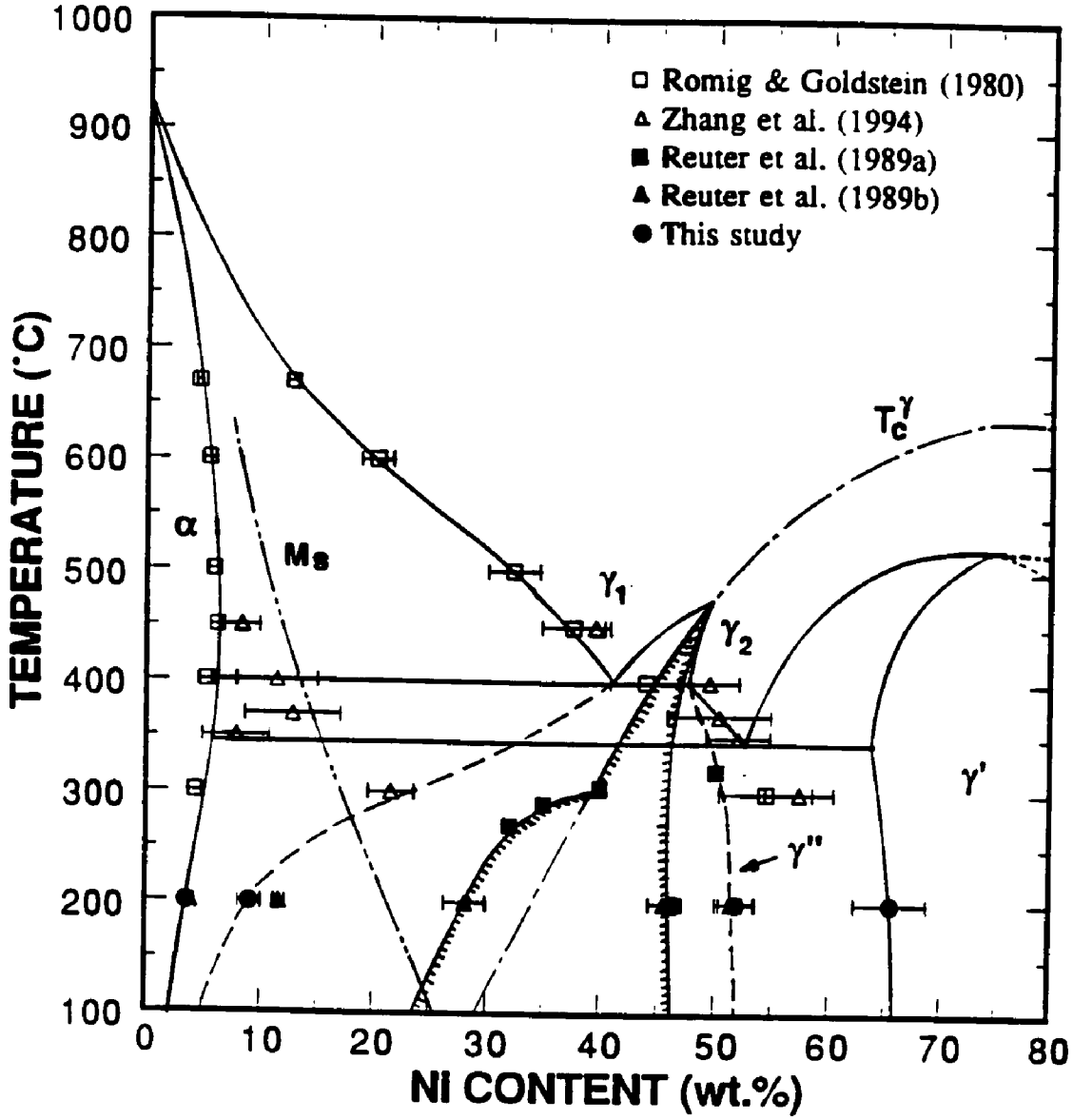

Fig. 5.4 Fe-Ni phase diagram determined in this study. Data obtained from previous studies and this study are shown. On this diagram, γ represents a high Ni fcc phase, γ_1 represents a low Ni paramagnetic fcc phase, γ_2 represents a high Ni ferromagnetic fcc phase, γ' represents ordered Ni_3Fe, γ'' represents ordered FeNi.

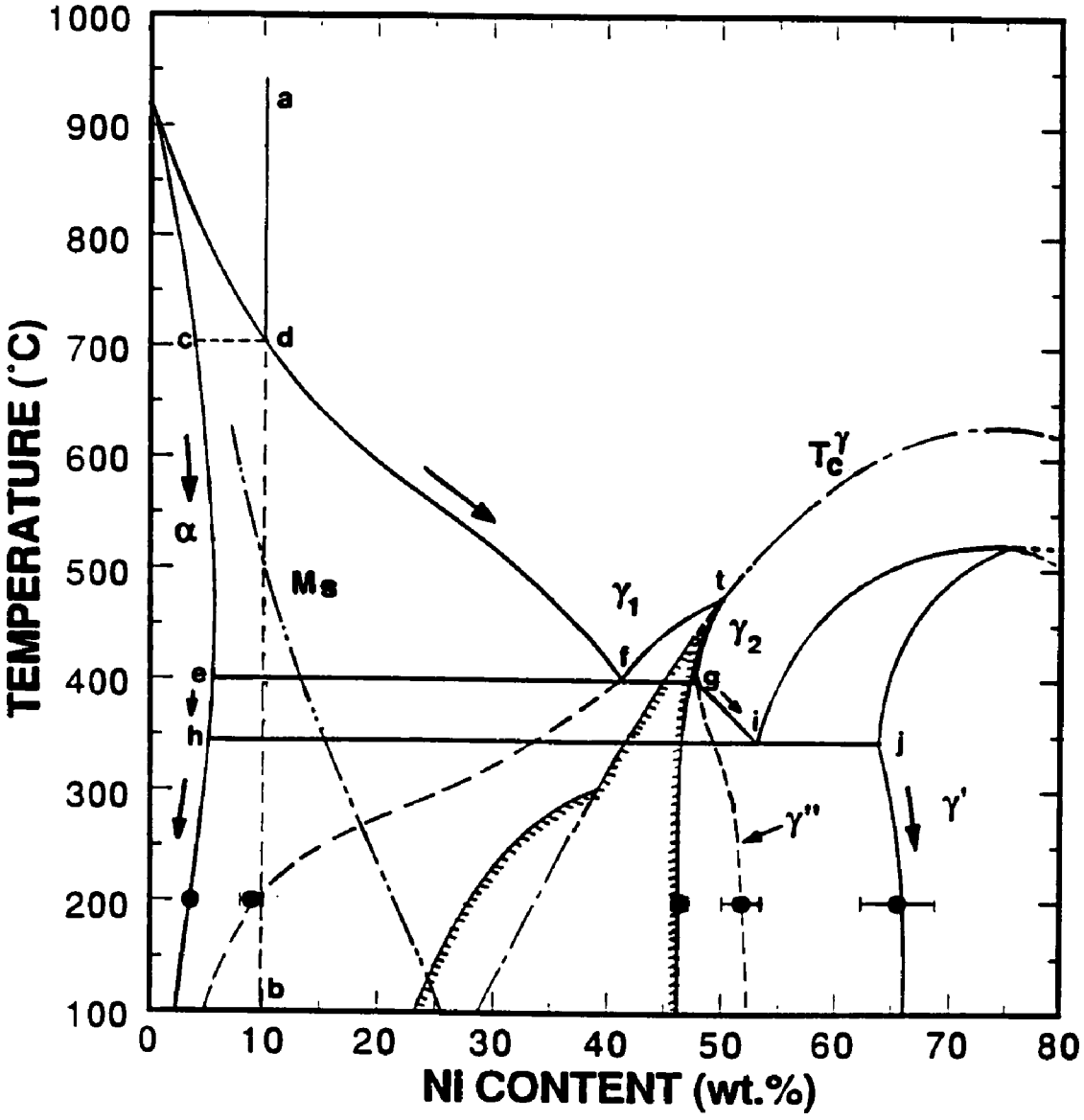

Fig. 5.5 Fe-Ni phase diagram determined in this study. AEM data obtained in this study are shown as filled circles. The arrows indicates the transformation path of equilibrium phases (see text for further details)

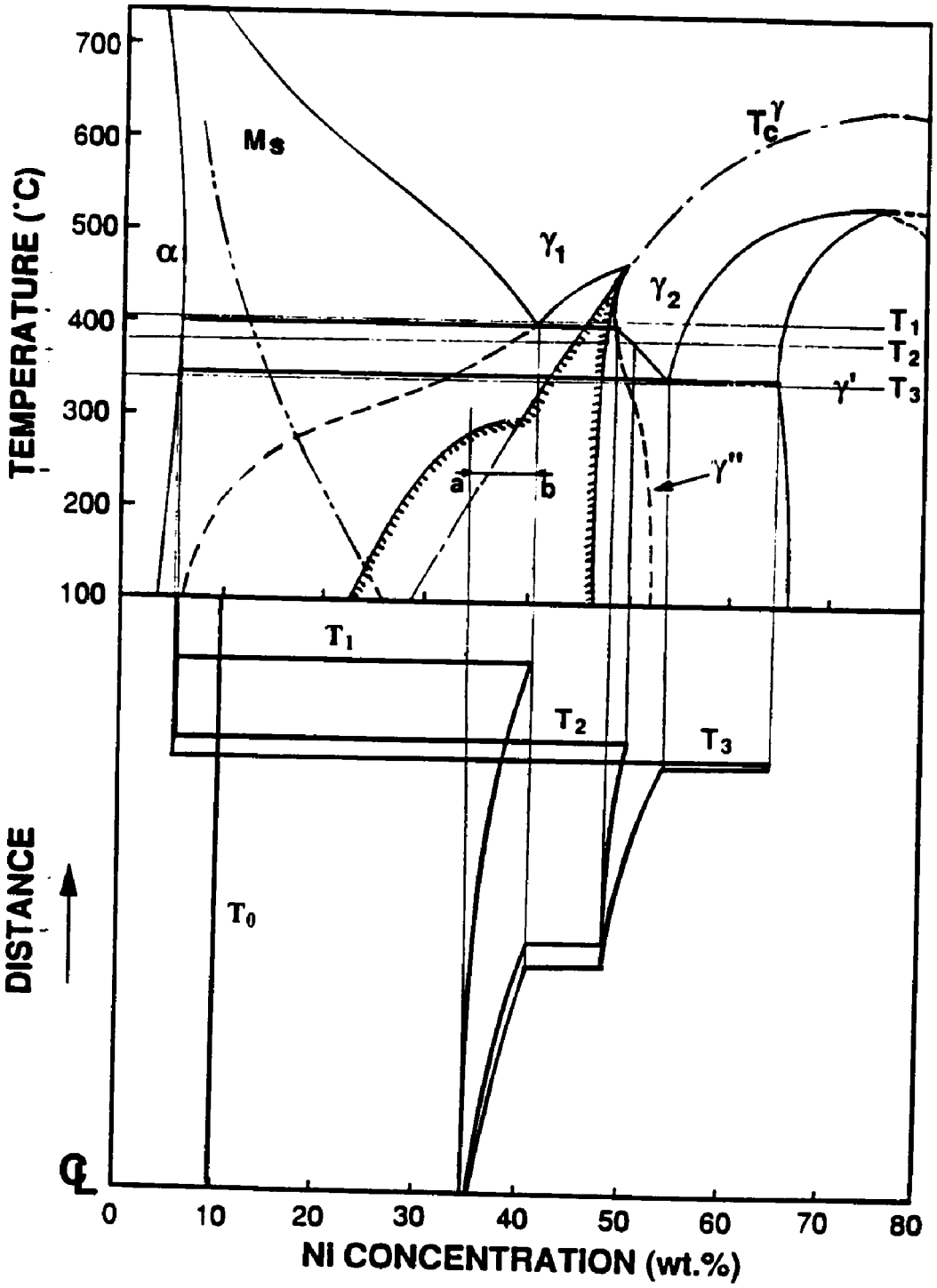

Fig. 5.6 Schematic Ni composition profile across kamacite and retained taenite at different temperatures.

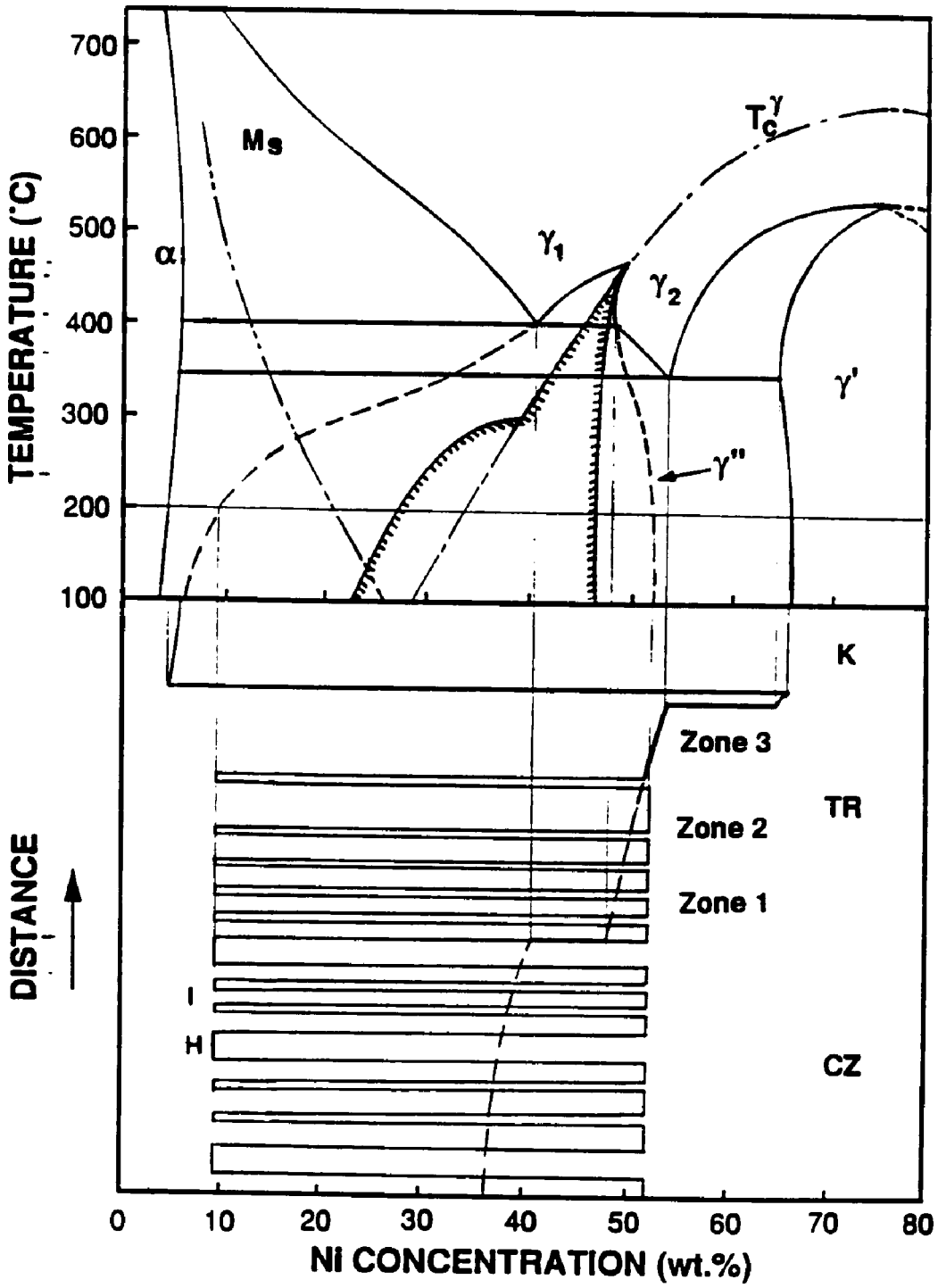

Fig. 5.7 Schematic Ni composition profile across kamacite and retained taenite at 200°C. The dashed line represents the bulk Ni composition.

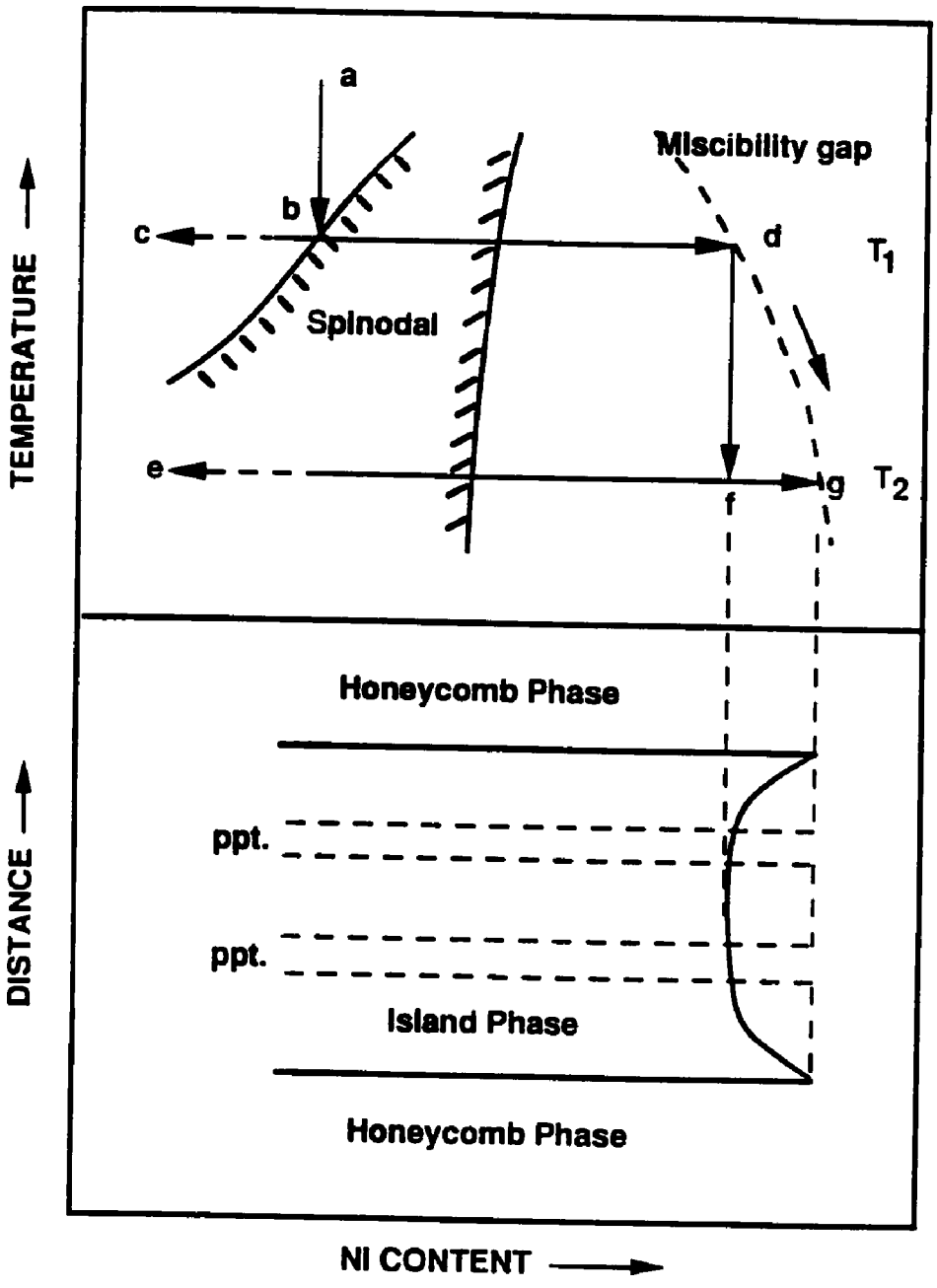

Fig. 5.8 Schematic illustration showing the precipitation process in the island phase.

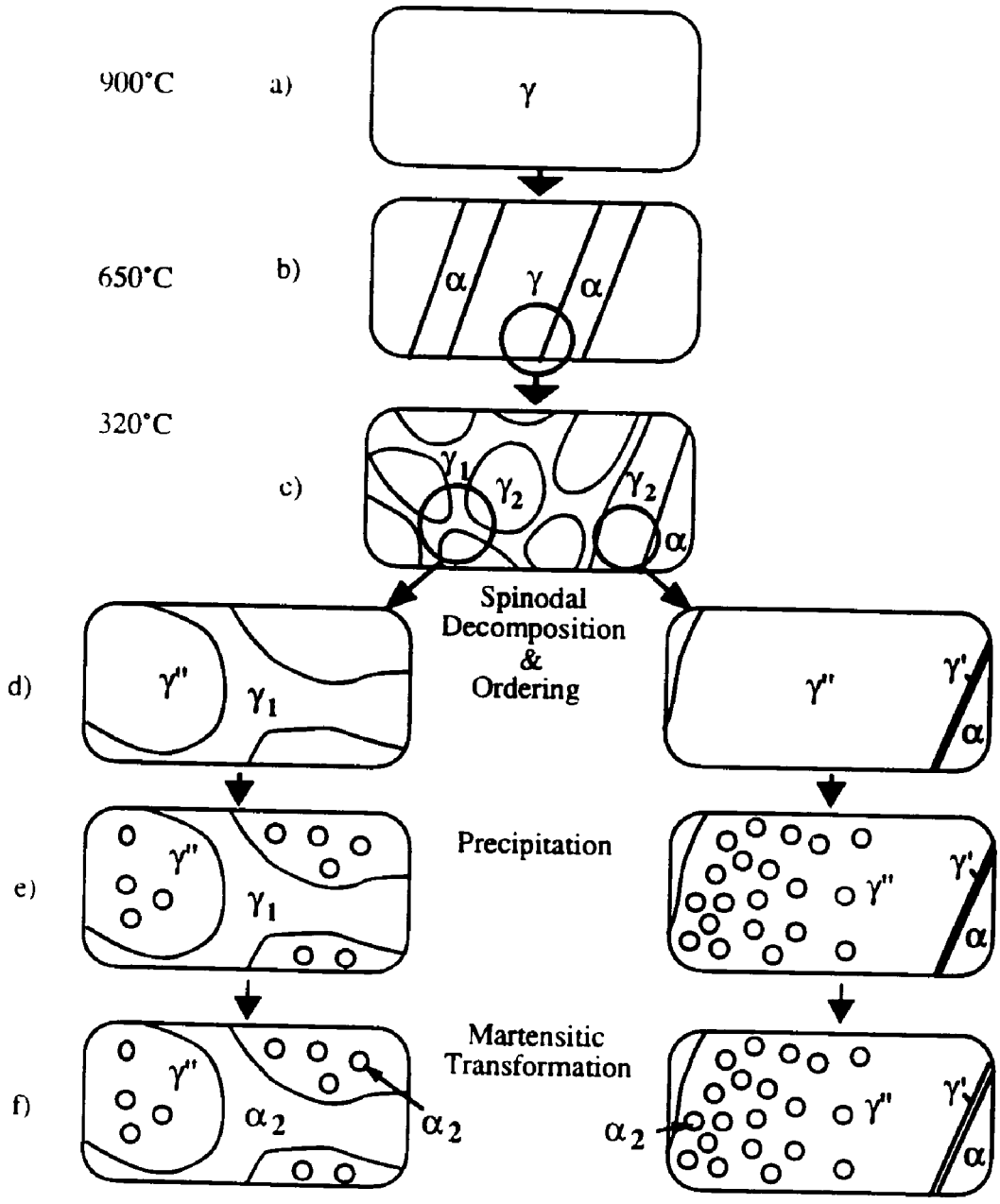

Fig. 5.9 Schematic illustration of a development of the microstructures in the CZ and the TR of meteorites during cooling.

REFERENCES

Afiattalab, F. and J. T. Wasson, (1980), Composition of the Metal Phases in Ordinary Chondrites: Implications Regarding Classification and Metamorphism. *Geochimica et Cosmochimica Acta*, Vol. 44, pp. 431-446.

Alani, R., (1990), Recent Advances in Ion Milling Techniques for TEM Specimen Preparation of Materials. *10th Anniversary of Chinese Electron Microscopy Society*, October 22-26, Beijing, China.

Alani, R., J. Jones, and P. Swann, (1990), Chemically Assisted Ion Beam Etching (CAIBE) - A New Technique for TEM Specimen Preparation of Materials, in Specimen Preparation for Transmission Electron Microscopy of Materials II, Mat. Res. Soc. Symp. Proc., Vol. 199, ed. by R. Anderson, MRS: pp. 85-101.

Albertsen, J. F., G. B. Jensen, J. M. Kundsen, and J. Danon, (1978), On Superstructure in Meteoritical Taenite. *Journal of the Meteoritical Society*, Vol. 13, No. 4, pp. 379-383.

Albertsen, J. F., J. M. Kundsen, N. O. Roy-Poulsen, and L. Vistisen, (1980), Meteorites and Thermodynamic Equilibrium in f.c.c. Iron-Nickel Alloys (25-50% Ni), *Physica Scripta*, Vol. 22, pp. 171-175.

Albertsen, J. F., (1981), Tetragonal Lattice of Tetrataenite (Ordered Fe-Ni, 50-50) from 4 Meteorites. *Physica Scripta*, Vol. 23, pp. 301-306.

Albertsen, J. F., H. P. Nielsen, and V. F. Buchwald, (1983), On the Fine Structure of Meteoritical Taenite/Tetrataenite and its Interpretation. *Physica Scripta.*, Vol. 27, pp. 314-320.

Allen, S. M. and J. W. Cahn, (1976), Mechanisms of Phase Transformations within the Miscibility Gap of Fe-Rich Fe-Al Alloys. *Acta Metallugica*, Vol. 24, pp. 425-437.

Barber, (1970), Thin Foils of Non-Metals Made for Electron Microscopy by Sputter-Etching. *Journal of Materials Science*, Vol. 5, pp. 1-8.

Barna, A. and B. Pécz, (1991), Simple Method for the Preparation of InP Based Samples for TEM Investigation. *Journal of Electron Microscopy Technique*, Vol. 18, pp. 325-328.

Bastin, G. F., F. J. J. V. Loo, and H. J. M. Heijligers, (1984), Evaluation of the Use of Gaussian $\phi(\rho z)$ Curve in Quantitative Electron Probe Microanalysis: A New Optimization. *X-Ray Spectrometery*, Vol. 13, pp. 91-97.

Baxter, C. S. and W. M. Stobbs, (1985), TEM Methods for the Characterisation of Fine Metal Multilayers, *Ultramicroscopy*, Vol. 16, pp. 213-226.

Bravman, J. C. and R. Sinclair, (1984), The Prerparation of Cross-Section Specimens for Electron Microscopy, *Journal of Electron Microscopy Technique*, Vol. 1, pp. 53-61.

Breedis, J. F. and C. M. Wayman, (1962), The Martensitic Transformation in Fe-31 wt.% Ni, *Transactions of the Metallurgical Society of AIME*, Vol. 224, pp. 1128-1133.

Buchwald, V. F., (1975), *Handbook of Iron Meteorites*, University of California Press.

Buseck, P. R. and J. I. Goldstein, (1969), Olivine Compositions and Cooling Rates of Pallasitic Meteorites, *Geological Society of America Bulletin*, Vol. 80, pp. 2141-2158.

Cahn, J. W., (1961), On Spinodal Decomposition, *Acta Metallugica*, Vol. 9, pp. 795-801.

Cahn, J. W., (1962), On Spinodal Decomposition in Cubic Crystals, *Acta Metallugica*, Vol. 10, pp. 179-183.

Cahn, J. W., (1968), Spinodal Decomposition, *Transactions of AIME*, Vol. 242, pp. 166-180.

Cech, R. E. and D. Turnbull, (1956), Heterigeneous Nucleation of the Martensite Transformation, *Journal of Metals*, Vol. pp. 124-132.

Chamberod, A., J. Laugier, and J. M. Penisson, (1979), Electron Irradiation Effects on Iron-Nickel Invar Alloys, *Journal of Magnetism and Magnetic Materials*, Vol. 10, pp. 139-144.

Chamberod, A., M. Roth, and L. Billard, (1978), Small Angle Neutron Scattering Invar Alloys, *Journal of Magnetism and Magnetic Materials*, Vol. 7, pp. 101-103.

Chang, P., M. D. Coviello, and A. F. Scott, (1988), *Cross-Sectional TEM Sample Preparation for Multilayer Electronic Materials.*, in Specimen Preparation for Transmission Electron Microscopy of Materials, Mat. Res. Soc. Symp. Proc., Vol. 115, ed. by J. C. Bravman, R. M. Anderson, and M. L. McDonald, MRS: pp. 93-97.

Chew, N. G. and A. G. Cullis, (1987), The Preparation of Transmission Electron Microscopy Specimens from Compound Semiconductors by Ion Milling, *Ultramicroscopy*, Vol. 23, pp. 175-198.

Christian, J. W., (1975), *The Theory of Transformations in Metals and Alloys*, Oxford, Pergamon Press.

Christiansen, A., L. Larsen, H. Roy-Poulsen, N. O. Roy-Poulsen, L. Vistisen, and J. M. Knudsen, (1984), Iron-Nickel Alloys in a Taenite Lamella from the Iron Meteorite Cape York as Measured by Conversion Electron Mössbauer Spectroscopy, *Physica Scripta*, Vol. 29, pp. 94-96.

Chuang, Y. Y., Y. A. Chang, R. Schmid, and J. C. Lin, (1986b), Magnetic Contributions to the Thermodynamic Functions of Alloys and the Phase Equilibria of Fe-Ni System below 1200K. *Metallurgical Transaction*, Vol. 16A, August, pp. 1361-1372.

Chuang, Y. Y., K. Hsieh, and Y. A. Chang, (1986a), A Thermodynamic Analysis of the Phase Equilibria of the Fe-Ni System above 1200K, *Metallurgical Transaction*, Vol. 17A, August, pp. 1373-1380.

Clarke, R. S., Jr. and E. R. D. Scott, (1980), Tetrataenite-Ordered FeNi, a New Mineral in Meteorites, *American Mineralogist*, Vol. 65, pp. 624-630.

Clarke, R. S., Jr. and B. Mason, (1982), A New Metal-Rich Mesosiderite from Antartica, RKPA79015, *Proc. of Anartica Meteorites*, Tokyo, Nat. Ins. Polar Res., pp. 78-85.

Cliff, G. and G. W. Lorimer, (1975), The Quantitative Analysis of Thin Specimens, *Journal of Microscopy*, Vol. 103, pp. 203-207.

Cullis, A. G. and N. G. Chew, (1988), *Ion Milling of Compound Semiconductors for Transmission Electron Microscopy.*, in Specimen Preparation for Transmission Electron Microscopy of Materials, Mat. Res. Soc. Symp. Proc., Vol. 115, ed. by J. C. Bravman, R. M. Anderson, and M. L. McDonald, MRS: pp. 3-14.

Cullis, A. G., N. G. Chew, and T. L. Hutchinson, (1985), Formation and Elimination of Surface Ion Milling Defects on CdTe, ZnS and ZnSe, *Ultramicroscopy*, Vol. 17, pp. 203-212.

Danon, J., M. Christophe, C. Jehanno, K. Keil, C. B. Gomaes, and R. B. Scorzelli, (1981), Awaruite (Ni_3Fe) in the Genomict LL Chondrite Parambu: Formation under High FeO_2, *Meteoritics*, Vol. 16, pp. 305.

Dodd, R. T., (1981), *Meteorite: A Petrologic-Chemical Synthesis*, New York, Cambridge Univ. Press.

Duffield, C. E., (1989), *The Structure and Composition of Taenite Particles in Two Type VI Ordinary Chondrite Meteorites*, M. S. thesis, Lehigh University, Bethlehem, PA

Duncumb, P., (1966), *Precipitation Studies with EMMA - A Combined Electron Microscope and X-Ray Microanalyzer.*, in The Electron Microprobe, ed. by T. D. McKinley, K. F. J. Heinrich, and D. B. Wittry, New York, Wiley, p. 490.

Easterling, K. E. and P. R. Swann, (1971), Nucleation of Martensite in Small Particles, *Acta Metallugica*, Vol. 19, February, pp. 117-121.

Edington, J. W., (1976), *Pratical Electron Microscopy in Materials Science*, London, MacMillan Press.

Faulkner, R. G., T. C. Hopkins, and K. Norrgard, (1977), Improved Spatial Resolution Microanalysis in a Scanning Transmission Electron microscope, *X-ray Spectroscopy*, Vol. 6, pp. 72-78.

Fleischer, R. L. and P. B. Price, (1964), Tcchniques for Geological Dating of Minerals by Chemical Etching of Fission Fragment Tracks, *Geochimica et Cosmochimica Acta*, pp. 1705-1714.

Gaggero, J. and D. Hull, (1962), On the Nucleation of Martensite, *Acta Metallugica*, Vol. 10, pp. 995-998.

Georgiyeva, I. Y. and O. P. Maksimova, (1971), Relation between Kinetics and Structure during Martensitic Transformations, *Fiz. Metal. Metalloved.*, Vol. 32, No. 2, pp. 364-376.

Goldstein, J. I. and R. E. Ogilvie, (1965), A Re-Evaluation of the Iron-Rich Portion of the Fe-Ni System, *Transactions of the Metallurgical Society of AIME*, Vol. 233, December, pp. 2083-2087.

Goldstein, J. I. and J. M. Short, (1967a), Cooling Rates of 27 Iron and Stony-Iron Meteorites, *Geochimica et Cosmochimica Acta*, Vol. 31, pp. 1001-1023.

Goldstein, J. I. and J. M. Short, (1967b), The Iron Meteorites, Their Thermal History and Parent Bodies, *Geochimica et Cosmochimica Acta*, Vol. 31, pp. 1733-1770.

Goldstein, J. I., (1969), The Classification of Iron Meteorites, *Meteorite Research*, ed. by P. M. Millman, pp. 721-737.

Goldstein, J. I., J. L. Costley, G. W. Lorimer, and S. J. B. Reed, (1977), Quantitative X-Ray Analysis in the Electron Microscope, *Scanning Electron Microscopy/1977*, Vol. 1, Proc. of Workshop on Analytical Electron Microscopy, pp.315-323.

Goldstein, J. I., (1979), *Principles of Thin Film X-Ray Microanalysis.*, in Introduction to Analytical Elctron Microscopy, ed. by J. J. Hren, J. I. Goldstein, and D. C. Joy, New York, Plenum Press, pp. 80-120.

Goldstein, J. I., D. E. Newbury, P. Echlin, D. C. Joy, C. Fiori, and E. Lifshin, (1984), *Scanning Electron Microscopy and X-Ray Microanalysis*, New York, Plenum Press.

Goldstein, J. I., D. B. Williams, and K. B. Reuter, (1985), *Analytical Electron Microscopy and microbeam Analysis of Metallic Phases in Extraterrestrial Materials.*, in Microbeam Analysis-1985, ed. by J. T. Armstrong, San Francisco Press, pp. 259-265.

Goldstein, J. I., C. E. Lyman, and J. Zhang, (1990), Spatial Resolution and Detectability limits in Thin Film X-Ray Microanalysis, *Proc. of the XIIth International Congress for Electron Microscopy*, pp. 450-451.

Goodhew, P. J., (1985), *Thin Foil Preparation for Electron Microscopy*, Amsterdam, Elsevier.

Guimarães, J. R. C., J. Danon, R. B. Scorzelli, and I. S. Azevedo, (1980), Phase Stability on Iron-Nickel Invar Alloys, *J. Phys. F: Met. Phys.*, Vol. 10, pp. L197-202.

Haack, H., G. J. Taylor, E. R. D. Scott, and K. Keil, (1992), Thermal History of Chondrites: Hot Accretion vs. Metamorphic Reheating, *Geophysical Research Letters*, Vol. 19, No. 22, pp. 2235-2238.

Haasen, P., (1974), *Physical Metallurgy*, ed. Cambridge: Cambridge Univ. Press,

Haggerty, S. E. and B. M. McMahon, (1979), Magnetite-Sulfide-Metal Complexes in the Allende Meteorite, *Geochimica et Cosmochimica Acta*, Vol. 11, pp. 851-870.

Hefter, J., K. Ostrecher, and C. Sung, (1992), Improved Method for the Preparation of TiN-Coated WC-Co-Based Samples for Cross-Sectional AEM Investigation, *Microscopy Research and Technique*, Vol. 23, pp. 239-242.

Heumann, T. and G. Karsten, (1963), The Carbonyl Method and Vapor Deposition for Determining Equilibrium Phases at Low Temperatures Taking Iron-Nickel Alloys as an Example, *Arch. furdas Eisenh.*, Vol. 34, pp. 781-786.

Holland-Duffield, C. E., D. B. Williams, and J. I. Goldstein, (1991), The Structure and Composition of Metal Particles in Two Type 6 Ordinary Chondrites, *Meteoritics*, Vol. 26, pp. 97-103.

Hutchings, R., M. H. Loretto, I. P. Jones, and R. E. Smallman, (1979), Spatial Resolution in X-Ray Microanalysis of Thin Foils in STEM, *Ultramicroscopy*, Vol. 3, pp. 401-405.

Hua, X., (1994), Ferroan-Wairauite in the Ningqiang Carbonaceous Chondrite, *Metaoritics*, to be published.

Ivey, D. G. and G. R. Piercy, (1988), Cross-Sectional TEM Specimens of Metal Contacts to Semiconductors, *Journal of Electron Microscopy Technique*, Vol. 8, pp. 233-235.

Jago, R. A., (1974), A Structural Investigation of the Cape York Meteorite by Transmission Electron Microscopy, *Journal of Materials Science*, Vol. 9, pp. 564-568.

Jago, R. A., P. E. Clark, and P. L. Rossiter, (1982), The Santa Catharina Meteorite and the Equilibrium State of Fe-Ni Alloys, *Phys. Stat. Sol.*, Vol. 74 a, pp. 247-254.

Jicheng, Z. and J. Zhanpeng, (1990), Thermodynamics of the Massive, Bainitic and martensitic Transformations in Fe-C, Fe-Ni, Fe-Cr and Fe-Cu Alloys, *Acta Metallurgica et Materialia*, Vol. 38, No. 3, pp. 425-431.

Joy, D. C., D. E. Newbury, and R. L. Myklebus, (1982), The Role of Fast Secondary Electrons in Degrading Spatial-Resolution in the Analytical Electron Microscope, *Journal of Microscopy*, Vol. 128, pp. RP1-R2.

Kachi, S., Y. Bando, and S. Higuchi, (1962), The Phase Transformation of Irn Rich Iron-Nickel Alloy in Fine Particles, *Japanese Journal of Applied Physics*, Vol. 1, No. 6, pp. 307-313.

Kajiwara, S., S. Ohno, K. Homa, and M. Uda, (1987), Martensitic Transformation in Ultrafine Particles of Pure Co and Co-Fe Alloys, Proc. of *Phase Transformations '87*, Vol. London, pp. 216-219.

Kajiwara, S., S. Ohno, and K. Homa, (1991), Martensitic Transformation in Ultrafine Particles of Metals and Alloys, *Philosophical Magazine A*, Vol. 63, No. 4, pp. 625-644.

Kamenetskaya, D. S., O. P. Maksimova, and V. I. Shiryayev, (1983), Features of the Martensitic Transformation in High-Purity Iron-Nickel Alloys, *Phys. Met. Metall.*, Vol. 55, N0. 5, pp. 121-127.

Kamenetzky, E. A., M. Wall, R. Castro, and L. E. Tanner, (1988), *The Preparation of Mechanically Alloyed Powders for TEM Examination.*, in Specimen Preparation for Transmission Electron Microscopy of Materials, Mat. Res. Soc. Symp. Proc., Vol. 115, ed. by J. C. Bravman, R. M. Anderson, and M. L. McDonald, MRS, pp. 167-172.

Kanaya, K., K. Hojou, K. Adachi, and K. Toki, (1974), Ion Bombardment of Suitable Targets for Atomic Shadowing for Hogh Resolution Electron Microscopy, *Micron*, Vol. 5, pp. 89-119.

Kaufman, L. and M. Cohen, (1956), The Martensitic Transformation in the Iron-Nickel System. *Transactions of the Metallurgical Society of AIME*, Vol. 206, October, pp. 1393-1401.

Kellemeyn, G. W., A. E. Rubin, and J. T. Wasson, (1991), The Compositional Classification of Chondrites: V. The Karoonda (CK) Group of Carbinaceous Chondrites. *Geochimica et Cosmochimica Acta*, Vol. 55, pp. 881-891.

Kelly, T. F. and O. Auciello, (1980), On the Origin of Pyramids and Cones on Ion-Bombarded Copper Surfaces. .*Surface Science*, Vol. 100, pp. 135-153.

Kelly, T. F., M. R. Libera, and J. B. V. Sande, (1988), *Preparation of Thin-Foil TEM Specimens from Sub-Milimeter Particulate.*, in Specimen Preparation for Transmission Electron Microscopy of Materials, Mat. Res. Soc. Symp. Proc., Vol. 115, ed. by J. C. Bravman, R. M. Anderson, and M. L. McDonald, MRS, pp. 205-210.

Kim, M. J. and R. W. Carpenter, (1987), TEM Specimen Heating during Ion Beam Thinning: Microstructural Instability. *Ultramicroscopy*, Vol. 21, pp. 327-334.

Klostermann, J. A. and W. G. Burgers, (1964), Surface Martensite in Iron-Nickel. *Acta Metallugica*, Vol. 12, April, pp. 355-360.

Kowalik, J. A., D. B. Williams, and J. I. Goldstein, (1988), Formation of the Lamellar Structure in Group IA and IIID Iron Meteorites, *Proc. of 18th Lunar Planetary Science Conference*, pp. 493-501.

Krauss, G. and A. R. Marder, (1971), The Morphology of Martensite in Iron Alloys. *Metallurgical Transactions*, Vol. 2, pp. 2343-2357.

Krauss, W., S. K. Pabi, and H. Gleiter, (1989), On the Mechanism of Martensite Nucleation. *Acta Metallugica*, Vol. 37, N0. 1, pp. 25-30.

Krumeich, F. and W. Mertin, (1991), Preparation by Ion Milling and TEM Investigation of Embedded Needle-Shaped Crystals of H-Nb_2O_5. *Microscopy Research and Technique*, Vol. 19, pp. 361-365.

Kubaschewski, O., K. Geiger, and K. Hack, (1977), The Thermochemical Properties of Iron-Nickel Alloys. *Z. Metallkde.*, Vol. 68, H. 5, pp. 337-341.

Kubaschewski, O., (1982), *Iron Binary Phase Diagrams*, Springer-Verlag, pp.73-78.

Kubo, H. and C. M. Wayman, (1980), A Theoritical Basis for Spinodal Decomposition in Ordered Alloys. *Acta Metallugica*, Vol. 28, pp. 395-404.

Laughlin, D. E., K. B. Alexander, and L. L. Lee, (1984), Spinodal Decomposition and Continuous Ordering, *Proc. of 2nd Acta-Scripta Metallurgica Conference*, Sonnenberg, Germany, Pergamom Press, pp. 221-226.

Laughlin, D. E. and W. A. Soffa, (1988), *Exsolution, Ordering and Structural Transformations: Systematics and Synergistics.*, in Physical Properties and Thermodynamic Behaviour of Minerals, NATO ASI Series C, Vol. 225, ed. by E. K. H. Salje, D. Reidel Publishing Co.: pp. 213-264.

Leech, P. and C. Sykes, (1939), The Evidence for a Superlattice in Nickel-Iron Alloy Ni_3Fe, *Philosophical Magazine*, Vol. 27, pp. 742-753.

Li, C. H., D. A. Porter, and K. E. Easterling, (1981), On the Nucleation and Growth of Martensite in Small iron Particles in Copper, Proc. of *Solid - Solid Phase Transformations*, Vol. Pittsburgh, Met. Soc. AIME, pp. 1177-1181.

Lin, L. S., J. I. Goldstein, and D. B. Williams, (1977), Analytical Electron Microscopy Study of the Plessite Structure in the Carlton Iron Meteorite, *Geochimica et Cosmochimica Acta*, Vol. 41, pp. 1861-1874.

Lin, L. S., J. I. Goldstein, and D. B. Williams, (1979), Analytical Electron Microscopy Study of the Plessite Structure in Four IIICD Iron Meteorites, *Geochimica et Cosmochimica Acta*, Vol. 43, pp. 725-737.

Lin, J. and Y. A. Chang, (1988), Magnetic-Induced Tricritical Points in Alloys, *Metallurgical Transactions*, Vol. 19A, March, pp. 441-446.

Mandel, J., (1984), *The Statistical Analysis of Experimental Data*, New York, Dover Publications.

Malis, T., S. C. Cheng, and R. F. Egerton, (1988), EELS Log-Ratio Technique for Specimen Thickness Measurement in the TEM, *Journal of Electron Microscopy Technique*, Vol. 8, pp. 193-200.

Marder, J. M. and A. R. Marder, (1969), The Morphology of Iron-Nickel Massive Martensite, *Transactions of the ASM*, Vol. 62, pp. 1-10.

Massalski, T. B., F. R. Park, and L. F. Vassamillet, (1966), Speculations about Plessite, *Geochimica et Cosmochimica Acta*, Vol. 30, pp. 649-662.

McMahon, B. M. and S. E. Haggerty, (1980), Experimental Studies Bearing on the Magnetite-Alloy-Sulfide Association in the Allende Meteorite: Constraints on the Conditions of Chondrule Formation, *Geochimica et Cosmochimica Acta*, Vol. 14, pp. 1003-1025.

McSween, H. Y., Jr., (1987), *Meteorites and Their Parent Planets*, New York, Cambridge Univ. Press.

Mehta, S., P. M. Novotny, D. B. Williams, and J. I. Goldstein, (1980), Electron-Optical Observations of Ordered FeNi in the Estherville Meteorite, *Nature*, Vol. 284, No. 5752, pp. 151-153.

Michael, J. R., D. B. Williams, C. F. Klein, and R. Ayer, (1990), The Measurement and Calculation of the X-Ray Spatial Resolution Obtained in the Analytical Electron Microscope, *Journal of Microscopy*, Vol. 160, Part 1, October, pp. 41-53.

Mirzayev, D. A., M. M. Steynberg, T. N. Ponomareva, and V. M. Schastlivtsev, (1979a), Influence of Cooling Rate on the Position of Martensitic Transformation Point. Carbon Steels, *Phys. Met. Metall.*, Vol. 47, N0.1, pp. 102-111.

Mirzayev, D. A., M. M. Steynberg, T. N. Ponomareva, and V. M. Schastlivtsev, (1979b), Influence of Cooling Rate on the Position of Martensitic Transformation Point. II. Alloyed Steels, *Phys. Met. Metall.*, Vol. 47, N0.5, pp. 73-79.

Moren, A. E. and J. I. Goldstein, (1978), Cooling Rate Variations of Group IVa Iron Meteorites, *Earth and Planetry Science Letters*, Vol. 40, pp. 151-161.

Moren, A. E. and J. I. Goldstein, (1979), Cooling Rates of Group IVa Iron Meteorites Determined from a Ternary Fe-Ni-P Model, *Earth and Planetry Science Letters*, Vol. 43, pp. 182-196.

Morita, H., A. Chamberod, and S. Steinemann, (1984), Electron Irradiation Effects on the Curie Temperature of Fe-Ni Invar Alloys, *J. Phys. F: Met. Phys.*, Vol. 14, pp. 3053-3059.

Morris, P. L., N. C. Davies, and J. A. Treverton, (1977), Development in Electron Microscopy and Analysis, ed. by D. L. Misell, Inst. of Phys., p. 377

Nagatani, T., S. Saito, M. Sato, and M. Yamada, (1987), Development of an Ultra High Resolution Scanning Electron Microscope by means of a Field Emission Source and In-Lens System, *Scanning Microscopy*, Vol. 1, pp. 901-909.

Newbury, D. E. and R. E. Myklebust, (1980), *Calculation of Electron Probe Spreading in Composite Thin Foil Targets.*, in Microbeam Analysis 1980, ed. by D. B. Wittry, San Francisco Press, San Francisco, pp. 173-175.

Novotny, P. M., D. B. Williams, and J. I. Goldstein, (1982), Analytical Electron Miscroscope Study of Eight Ataxites, *Geochimica et Cosmochimica Acta*, Vol. 46, pp. 2461-2469.

Ostreicher, K. and C. Sung, (1993), Cross-Sectional AEM Preparation Technique for Ceramic-Coated WC-Co Cutting Tools, *Microscopy Research and Technique*, Vol. 24, pp. 505-508.

Paulevé, J., D. Dautreppe, J. Laugier, and L. Néel, (1962), A New Order-Disorder Transition in Fe-Ni (50-50), *Journal de Physique.*, Vol. 23, pp. 841-843.

Pear, W. b., (1958), *A Handbook of Lattice Spacing and Structures of Metals and Alloys*, New York, Pergamon Press, pp. 638-641.

Pellas, P. and D. Storzer, (1981), ^{224}Pu Fission Track Thermometry and Its Application to Stony Meteorites, *Proc. of Royal Society London*, Vol. A 374, pp. 253-270.

Peterson, J. F., M. Aydin, and J. M. knudsen, (1977), Mössbauer Spectroscopy of an Ordered Phase (Superstructure) of FeNi in an Iron Meteorite, *Physics Letters*, Vol. 62A, No. 3, pp. 192-194.

Porter, D. A. and K. E. Easterling, (1981), *Phase Transfromations in Metals and Alloys*, Chapman & Hall.

Powell, B. N., (1969), Petrology and Chemistry of mesosiderites-I. Textures and Composition of Nickel-Iron, *Geochimica et Cosmochimica Acta*, Vol. 33, pp. 789-810.

Radomsky, P. M. and R. H. Hewins, (1990), Formation Conditions of Pyroxene-Olivine and and Magnesian Olivine Chondrules, *Geochimica et Cosmochimica Acta*, Vol. 54, pp. 3475-3490.

Rasmussen, K. L., (1982), Determination of the Cooling Rates and Nucleation Histories of Eight Group IVA Iron Meteorites Using Local Bulk Ni and P Variation, *ICARUS*, Vol. 52, pp. 444-453.

Reed, S. J. B., (1982), The Single Scattering Model and Spatial Resolution in X-Ray Analysis of Thin Foils, *Ultramicroscopy*, Vol. 7, pp. 405-409.

Reuter, K. B., D. B. Williams, and J. I. Goldstein, (1984), *Microanalysis and Microdiffraction of two-phase regions in the Metallic Phase of the Estherville Meteorite*, San Francisco Press, pp. 177-182.

Reuter, K. B., (1986), *Determination of the Fe-Ni and Fe-Ni-P (sat) Phase Diagrams below 400°C*, P. D. dissertation, Lehigh University, Bethlehem, PA

Reuter, K. B., D. B. Williams, and J. I. Goldstein, (1988), Low Temperature Phase Transformations in the Metallic Phases of Iron and Stony Iron Meteorites, *Geochimica et Cosmochimica Acta*, Vol. 52, pp. 617-626.

Reuter, K. B., D. B. Williams, and J. I. Goldstein, (1989a), Ordering in the Fe-Ni System under Electron Irradiation, *Metallurgical Transactions*, Vol. 20A, April, pp. 711-718.

Reuter, K. B., D. B. Williams, and J. I. Goldstein, (1989b), Determination of the Fe-Ni Phase Diagram below 400°C, *Metallurgical Transactions*, Vol. 20A, pp. 719-725.

Reynaud, F., (1982), Order-Disorder Transitions in Substitutional Solid Solutions, *Phys. Stat. Sol.*, Vol. (a) 72, pp. 11-59.

Romig, A. D., Jr., (1979), *Determination of the Fe-Ni and Fe-Ni-P Phase Diagrams at Low Temperatures (700 to 300°C)*, P. D. Dissertation, Lehigh University, Bethlehem, PA

Romig, A. D., Jr. and J. I. Goldstein, (1980), Determination of the Fe-Ni and Fe-Ni-P Phase Diagrams at Low Temperatures (700 to 300°C), *Metallurgical Transactions*, Vol. 11A, July, pp. 1151-1159.

Rossiter, P. L. and R. A. Jago, (1984), Toward a True Fe-Ni Phase Diagram, *Proc. of Mat. Res. Soc. Symp.*, Vol. 21, Elsevier Science Publishing Co., pp. 407-411.

Rubin, A. E., (1991), Euhedral Awaruite in the Allende Meteorite: Implications for the Origin of Awaruite- and Magnetite-Bearing Nodules in CV3 Chondrites, *American Mineralogist*, Vol. 76, pp. 1356-1362.

Rudman, P. S., (1967), *Order-Disorder and Radiation Damage*, in Intermetallic Compounds, ed. by J. H. Westbrook, John Wiley & Sons, Inc., NewYork, pp. 405-427.

Russell, K. C. and F. A. Garner, (1992), Thermal and Irradiation-Induced Phase Separation in Fe-Ni Based Invar-Type Alloys, *Metallurgical Transactions*, Vol. 23A, July, pp. 1963-1976.

Sadchikov, V. V. and I. M. Puzey, (1983), On the Formation of an $L1_0$ Type Superstructure in the Fe-Ni System, *Fiz. Metal. Metalloved.*, Vol. 56, No. 4, pp. 829-831.

Saikumar, V. and J. I. Goldstein, (1988), An Evalution of the Methods to Determine the Cooling Rates of Iron Meteorites, *Geochimica et Cosmochimica Acta*, Vol. 52, pp. 715-726.

Schlosser, W. F., (1971), A Model for the Invar Alloys and the Fe-Ni System, *Journal of Physics and Chemistry of Solids*, Vol. 32, pp. 939-949.

Scott, E. R. D., (1973), The Nature of Dark-Etching Rims in Meteoritic Taenite, *Geochimica et Cosmochimica Acta*, Vol. 37, pp. 2283-2294.

Scott, E. R. D. and R. S. Clarke Jr., (1979), Identification of Clear Taenite in Meteorites as Ordered FeNi. *Nature*, Vol. 281, pp. 360-362.

Scott, E. R. D., A. J. Brearley, H. Haack, and T. J. McCoy, (1994), Catastrophic Fragmentation and Reassembly of the Parent Body of the IVA Iron and Stony-Iron Meteorites, *Meteoritics*, Vol. 29, No. 4, pp. 530-531.

Shield, J. E., C. M. Hsu, M. J. Kramer, B. D. Merkle, and R. W. McCallum, (1993), Preparation of Fine Powders for Electron Microscopy Investigations, *Materials Characterization*, Vol. 31, pp. 33-38.

Soffa, W. A. and D. E. Laughlin, (1982), Recent Experimantal Studies of Continuous Transformations in Alloys: An Overview, *Proc. of Solid-Solid Phase Transformaitons*, Pittsburgh, pp. 159-183.

Soffa, W. A. and D. E. Laughlin, (1989), Decomposition and Ordering Process Involving Thermodynamically First-Order Order/Disorder Transformations, *Acta Metallugica*, Vol. 37, No. 11, pp. 3019-3028.

Soylu, B. and R. W. K. Honeycombe, (1987), Precipitation of Copper in a Duplex Stainless Steel, *Proc. of Phase Transformations '87*, Vol. London, pp. 135-138.

Tan, Y. H., D. C. Zeng, X. C. Dong, Y. H. He, and S. Q. Hu, (1992), New Observation of Martensitic Morphology and Substructure Using Transmision Electron Microscopy, *Metallurgical Transactions*, Vol. 23A, May, pp. 1413-1421.

Thadhani, N. N. and M. A. Meyers, (1986), *Kinetics of Isothermal Martensitic Transformation*, in Progress in Materials Science, ed. by J. W. Christian, P. Haasen, and T. B. Masalski., Pergamon: Oxford, pp. 1-37.

Thomas, G. and J. C. Lacaze, (1973), Transmission Electron Microscopy at 2.5 MeV, *Journal of Microscopy*, Vol. 97, pp. 301-308.

Thompson, M. N., P. Doig, J. W. Edington, and P. E. J. Flewitt, (1977), The Influence of Specimen Thickness on X-Ray Count Rates in STEM-Microanalysis, *Philosophical Magazine*, Vol. 35, pp. 1537-1542.

Urey, H. C. and T. Mayeda, (1959), The Metallic Particles of some Chondrites, *Geochimica et Cosmochimica Acta*, Vol. 17, pp. 113-124.

VanDeen, J. K. and F. v. d. Woude, (1980), Phase Diagram of the Order-Disorder Transition in Ni_3Fe, *Journal de Physique.*, Vol. 41, C1, pp. 367-368.

VanDeen, J. K. and F. v. d. Woude, (1981), Phase Diagram of the Order-Disorder Transition in Ni_3Fe, *Acta Metallugica*, Vol. 29, pp. 1255-1262.

Warlimont, H., (1961), Increased Martensite Formation Temperature in Thin Films, *Transactions of the Metallurgical Society of AIME*, Vol. 221, December, pp. 1270-1271.

Wasson, J. T., (1985), *Meteorites: Their Record of Early Solar-System History*, New York, W. H. Freeman and Company.

Williams, D. B., (1984), *Pratical Analytical Electron Microscopy in Materials Science*, New Jersey, Philips Electronic Instruments Inc., Electron Optics Publishing Group.

Williams, D. B., J. R. Michael, J. I. Goldstein, and A. D. Romig, (1991), The Spatial Resolution of X-Ray Microanalysis in Thin Foils, *Proc. of the 49th Annual Meeting of the EMSA*, ed. by G. W. Bailey, San Francisco Press, Inc., pp.472-473.

Willis, J. and J. T. Wasson, (1978), Cooling Rates of Group IVA Iron Meteorites, *Earth and Planetry Science Letters*, Vol. 40, pp. 141-150.

Willis, J. and J. I. Goldstein, (1983), A Three-Dimensional Study of Metal Grains in Equilibrated, Ordinary Chondrites, *Journal of Geophysical Research*, Vol. 88, pp. B287-B292.

Wilson, E. A., (1984), $\gamma \rightarrow \alpha$ Transformation in Fe, Fe-Ni, and Fe-Cr Alloys, *Metal Science*, Vol. 18, October, pp. 471-484.

Wood, J. A., (1964), The Cooling Rates and Parent Planets of Several Iron Meteorites, *ICARUS*, Vol. 3, pp. 429-459.

Wood, J. A., (1967), Chondrites: Their Metallic Minerals, Thermal Histories, and Parent Planets, *ICARUS*, Vol. 6, pp. 1-49.

Yao, J. Y. and G. L. Dunlop, (1991), Preparation of (InGa)As/GaAs Multilayered Materials for TEM by One Side Non-Rotation Ion Beam Thinning, *Journal of Electron Microscopy Technique*, Vol. 19, pp. 90-98.

Yang, C. W., D. B. Williams, and J. I. Goldstein, (1993), Metallographic Observation of the Cloudy Zone in Meteorites, *Meteoritics*, Vol. 28, No. 3, pp. 464.

Yang, C. W., D. B. Williams, and J. I. Goldstein, (1994), New Cooling Rate Indicator for Metal Particles in Meteorites, *Meteoritics*, Vol. 29, No. 4, pp. 553-554.

Yu, J. E., K. S. Jones, and R. M. Park, (1991), A Technique for the Preparation of Cross-Sectional TEM Samples of ZnSe/GaAs Heterostructures Which Eliminates

Process-Induced Defects, *Journal of Electron Microscopy Technique*, Vol. 18, pp. 315-324.

Zhang, J., (1991), *Phase Decomposition in Fe-rich Fe-Ni Alloys at Low Temperatures (<450°C)*, P. D. dissertation, Lehigh University, Bethlehem, PA

Zhang, J., D. B. Williams, and J. I. Goldstein, (1988), AEM Investigation of the Plessite Structure of a IIIB Iron Meteorite-Grant, *Meteoritics*, Vol. 23, pp. 314.

Zhang, J., D. B. Williams, J. I. Goldstein, and R. S. C. Jr., (1990), Electron Microscopy Study of the Iron Meteorite Santa Catharina, *Meteoritics*, Vol. 25, pp. 167-175.

Zhang, J., D. B. Williams, and J. I. Goldstein, (1994), Decomposition of Fe-Ni Martensite: Implications for the Low-Temperature (<500°C) Fe-Ni Phase Diagram, *Metallurgical and Materials Transctions*, Vol. 25A, August, pp. 1627-1637.

Zhou, Y. H., M. Harmelin, and J. Bigot, (1990), Martensitic Transformation in Ultrafine Fe-Ni Powders, *Materials Science and Engineering A*, Vol. A124, pp. 241-249.

Zhou, Y. H., M. Harmelin, and J. Bigot, (1991), Preparation of Ultra-Fine Metallic Powders. A Study of the Structural Transformations and of the Sintering Behaviour, *Materials Science and Engineering A*, Vol. A133, pp. 775-779.

GLOSSARY

Accretion - the process by which particles come together to form a larger mass of material.

Achondrite - a class of stony meteorites that crystallized from magmas; the term literally means "without chondrules," emphasizing the distinction between these and chondrites.

Ataxite - an iron meteorite with high Ni content, composed almost entirely of taenite and having no obvious structure.

Chondrite - an abundant type of stony meteorite characterized by the presence of chondrules.

Chondrule - millimeter-sized spherule of rapidly cooled silicate melt, found in abundance in chondritic meteorites.

Fission track - a submicroscopic trail in a crystal along which a particle produced decay of a heavier isotope traveled; these can be used as a means of age determination.

Hexahedrite - an iron meteorite with low Ni content, consisting almost exclusively of kamacite.

Kamacite - bcc α-ferrite in meteorites.

Mesosiderite - a class of stony-iron meteorites consisting of equal proportions of metal and silicates.

Metamorphism - recrystallization, in the solid state, of a rock in response to high temperature or pressure.

Meteorite - extraterrestrial material that survives passage through the atmosphere and reaches the earth's surface as a recoverable object.

Octahedrite - an iron meteorite of intermediate Ni content, containing both kamacite and taenite in a Widmanstätten pattern.

Pallasite - a class of stony-iron meteorites consisting of metal and isolated crystals of olivine.

Taenite - fcc γ-austenite in meteorites.

Tetrataenite - an ordered FeNi phase (γ') in meteorites. The name is derived from its tetragonal structure and taenite.

VITA

Cheol-Woong Yang was born to Seong-Pil Yang and Hee-Bok Ryu on January 22, 1965 in Chunchon, Korea. He received his secondary education at Chunchon High School, Korea. After graduating from high school, he entered Seoul National University, Korea, in 1983. He was awarded a B.S. degree in Metallurgical Engineering with an honor in February, 1987 and awarded a M. S. degree in Metallurgical Engineering in February, 1989. While at the university, he worked with Korean Institute of Machinery and Metals for 6 months. In the fall of 1990 he entered Lehigh University. Since then, he has pursued his graduate education in the Department of Materials Science and Engineering at Lehigh University. He has seven technical publications. He is married to his wife, Eunha Kim, and has a daughter, Haeyeon.